

ADA 045315

Princeton University

D 2



D D C  
REF ID: A65114  
OCT 11 1977  
RECORDED  
RECORDED

Department of  
Aerospace and  
Mechanical Sciences

AD No. \_\_\_\_\_  
DDC FILE COPY

⑥ AERODYNAMICS AND HOVERING CONTROL OF LTA VEHICLES.

by

⑩ W. F. Putman  
M. Maughmer  
H. C. Curtiss, Jr.  
J. J. Traybar

Department of Aerospace and Mechanical Sciences, Princeton University Princeton, N. J.

⑪ FINAL REPORT

NADC Contract No. N62269-76-C-0493

⑫ ⑬ ⑭ AMS-TR-1339

Prepared in support of the Advanced Naval Vehicles Concepts Evaluation Project (OP96 C), 1300 Wilson Boulevard, Arlington, Virginia 22209, Area 202-697-0901.

D D C

OCT 11 1977

RECORDED  
RECEIVED  
REBOLVED

A

Monitored by: Naval Air Development Center  
Code 30P3  
Warminster, Pa. 18974  
Area 215-441-2501

⑮ 2550.1

⑯ A

A  
18

⑰ May 1977

288 475

18

## TABLE OF CONTENTS

	<u>Page</u>
<b>LIST OF FIGURES</b>	iii
<b>NOMENCLATURE</b>	vi
<b>INTRODUCTION</b>	1
<b>BODIES OF REVOLUTION</b>	2
Potential Flow Theories	
Empirical Approaches	
Angular Damping	
<b>AERODYNAMICS OF DELTA PLANFORMS</b>	47
Introduction	
Longitudinal Characteristics	
a.) Linear Region	
b.) Non-Linear Region	
Lateral-Directional Characteristics	
<b>AIRSHIP DRAG REDUCTION</b>	86
Drag Minimization Through Shaping	
Active Boundary-Layer-Control Through Suction	
Stern Propulsion for Airships	
Integrated Hull Design: Boundary-Layer-Control and Propulsion	
Conclusions and Recommendations	
<b>STABILITY AND CONTROL</b>	121
Keeping Station in a Steady Wind	
Keeping Station in Gusts	
Operator Control	
<b>BIBLIOGRAPHY</b>	139

11

LIST OF FIGURES

<u>Figures</u>		<u>Page</u>
1	Dimensionless Coefficients for Forces and Moments Acting on Ellipsoid of Revolution From Potential Flow Theory	11
2	Variation in Angle of Attack Stability and Directional Stability for Tri-Axial Ellipsoid. Potential Flow Theory	12
3	Second Order Theory Results: Parabolic Body of Revolution Compared with Exact Theory for Ellipsoid. Potential Flow	13
4	Comparison of Theory and Experiment for Loading on Slender Body at Angle of Attack	14
5	Local Loading on Flat Body and Body of Revolution	16
6	Circumferential Distribution of Pressure on Airship "Akron"; Comparison of Theory and Experiment	27
7	Body of Revolution in Inclined Flow Field	28
8	Variation of Cross-Flow Drag Coefficient with Cross-Flow Reynolds Number for Circular Cylinders	28
9	Ratio of the Drag Coefficient of a Circular Cylinder of Finite Length to That of a Cylinder of Infinite Length as a Function of the Fineness Ratio. $Re_c = 88,000$ .	29
10.	Schematic Diagram of Hopkins Flow Model for the Determination of Forces and Moments on Bodies of Revolution.	30
11.	Calculated Loci of Minimum Pressure Positions on Airship "Akron".	31
12	Correlation Between Assumed Extent of Applicability of Potential Theory and the Position of the Maximum Negative Rate of Change of Body Cross-Sectional Area With Body Length.	32
13	Model Geometries Used in the Development of Hopkins Theory.	33
14	Comparison Between the Experimental and the Estimated Lift, Drag and Pitching-Moment Characteristics of Various Bodies of Revolution.	34
15	Skin Friction Drag Coefficient as a Function of Reynolds Number.	41

<u>Figures</u>		<u>Page</u>
16	Drag Coefficient on a Body of Revolution as a Function of Fineness Ratio as Calculated by Hoerner's Formula	41
17	Flow Model for Zero-Lift Drag Prediction on Body of Revolution	42
18	Potential Flow on Triangular Wings of Low Aspect Ratio	64
19	Pressure and Lift Distribution on Delta Wing, Jones' Theory	65
20	Lift Curve Slope vs. Aspect Ratio for Triangular Wings	66
21	Center of Pressure vs. Aspect Ratio for Uncambered Delta Wings	67
22	Lift Characteristics of Sharp and Round Leading Edge Delta Planforms	68
23	Comparison of Prediction Method and Experimental Lift and Moment Data	69
24	Definition of Lift Curve Regions	73
25	Comparison of Prediction Method and Experimental Data for Profile Drag	74
26	Determination of Efficiency Factor for Induced Drag	75
27	Comparison of Predicted and Measured Induced Drag at Low Angles-of-Attack.	77
28	Comparison of Predicted and Measured Drag at High Angles-of-Attack	78
29	Method of Application of Non-Linear Drag	82
30	Directional Stability Derivative	83
31	Center of Lateral Pressure Location	84
32	Dihedral Effect Derivative	85

<u>Figures</u>		<u>Page</u>
33	Model of Flow Over Body of Revolution	113
34	Transition Location as a Function of Fineness Ratio and Its Effect on Separation	113
35	Effect on Laminar Flow Design of Increasing Reynolds Number	114
36	Effect of Increasing Flight Velocity on Drag Gains Achieved by Laminar Flow Design	114
37	Coefficient of Skin Friction of a Flat Plate at Zero Incidence with Suction	115
38	Effect of BLC on the Overall Drag of Airships	115
39	Thirty-four Percent Thick Lighthill Airfoil Body and Velocity Distribution	116
40	Experimentally Determined Bare Hull Drag	117
41	Stern Propelled Airship	117
42	Schematic of BLC Airship Propulsion System	118
43	Comparison of BLC Airship with Conventional For Equal Volume	119
44	Possible Reductions in the Power Requirements of Airships	120
45	Lateral Drag and Propeller Horsepower Required to Balance Lateral Drag at Zero Forward Speed for Various Wind Velocities	133
46	RMS Lateral Displacement as a Function of Closed Loop Vehicle Damping Ratio and Natural Frequency	134
47	Level of Roll Disturbance Caused by Gusts and Translational Control System	136
48	Closed Loop Dynamics, Translational Control by Human Operator; Position Feedback with Lag $\tau_o$	137
49	RMS Displacement in Gusts with Human Operator Control; Displacement Feedback with Lag	138

### NOMENCLATURE

$A_b$	body base area at $x = l$ , ft <sup>2</sup>
$A_p$	planform area of body, ft <sup>2</sup> , or propeller area, ft <sup>2</sup>
AR or A	aspect ratio, $AR = \frac{b^2}{S_w}$
a	semilength, ellipsoid
b	semispan, ellipsoid or full span, wing
$C_d$	drag coefficient, $C_d = \frac{D}{q S_w}$ or $\frac{D}{q \psi^{2/3}}$
$C_f$	turbulent flat plate friction coefficient
$C_f$	skin friction drag based on wetted area
$C_L$	lift coefficient, $C_L = \frac{L}{q S_w}$ or $\frac{L}{q \psi^{2/3}}$
$C_\ell$	rolling moment coefficient, $C_\ell = \frac{L}{q S_w b}$
$C_m$	pitching moment coefficient, $C_m = \frac{M}{q S_w c}$ or $\frac{M}{q \psi}$
$C_N$	yawing moment coefficient, $C_N = \frac{N}{q S_w b}$ or normal force coefficient $C_N = \frac{\text{Normal Force}}{q \psi^{2/3}}$
$C_{N\beta}$ , $C_{\ell_p}$ , $C_{\ell_r}$ , $C_{m_q}$ , $C_{h_p}$ , $C_{h_r}$ ,	partial derivative of quantity with respect to variable indicated
$C_{L\alpha}$ , $C_{\ell_\beta}$ , $C_{m_q}$	

$C_M \tilde{q}$	measured damping derivative, $C_M \tilde{q} = [M_q + M_{\dot{q}}] \frac{4}{\rho \pi^{2/3} U_o^2 l^2}$
$C_D \alpha = 0$	drag coefficient at $\alpha = 0$ (based on $\psi^{2/3}$ )
$\Delta C_d$	increase in body drag coefficient above that at zero angle of attack
c	semithickness of ellipsoid, chord, ft.
$c_{d_c}$	sectional drag coefficient/unit length
D	diameter of hull, ft., drag force, lb.
d	diameter of body, ft.
$d_o$	maximum diameter of body, ft.
e	leading edge pressure efficiency factor
F	local aerodynamic force, lb.
FR	fineness ratio, length divided by maximum thickness
$f_p$	potential crossflow force per unit length, lb/ft.
G	drag factor for camber and position of maximum thickness
h	distance between centers of gravity and buoyancy
$h_c$	distance of control below center of gravity
I	moment of inertia, slug-ft <sup>3</sup>
$I'$	moment of inertia including virtual mass terms
$k_1, k_2$	shape factor in Munk's slender body theory
$k_o$	displacement feedback gain factor
$k_v$	velocity feedback gain factor
L	lift force, lb. or rolling moment, ft-lb., positive roll right

M	pitching moment, ft-lb.
M'	apparent mass, slugs
N	yawing moment, ft-lb., positive nose right
n	fineness ratio
F	propeller induced power, $\frac{\text{ft-lb}}{\text{sec}}$
p	pressure, lb/ft <sup>2</sup>
q	pitch rate, rad/sec., or dynamic pressure, lb/ft <sup>2</sup>
R	radius, ft.
R <sub>N</sub>	Reynolds number, $R_N = \frac{Vd}{\nu}$
Re <sub>x</sub>	Reynolds number for length, x
Re <sub>c</sub>	cross flow Reynolds number, $Re_c = \frac{Vd \sin \alpha}{\nu}$
r	yaw rate, rad/sec. or radius of body, feet
S	cross sectional area, ft <sup>2</sup>
S <sub>w</sub>	wing planform area, ft <sup>2</sup>
T	propeller thrust, lb.
t/c	thickness to chord ratio
U	free stream velocity, ft/sec.
U <sub>o</sub>	initial velocity, ft/sec.
u	body axis forward perturbation velocity, ft/sec.
v	velocity, ft/sec.
V <sub>o</sub>	initial velocity, ft/sec.
V	volume of body, ft <sup>3</sup>
v	body axis lateral perturbation velocity, ft/sec., positive right or induced velocity, ft/sec.

$v_g$	gust velocity, ft/sec.
Vcl.	body volume, ft <sup>3</sup>
w	body axis vertical perturbation velocity, ft/sec., positive downward, or vehicle weight, lb.
X	axial force, lbs., positive forward
x	longitudinal (chordwise) position, ft.
$x_o$	endpoint of integration, ft.
$x_1$	point at which $\frac{ds}{dx}$ is most negative
$x_m$ , $x_t$	longitudinal position of maximum thickness, ft. or per unit chord
$x_c$	longitudinal position of maximum camber, per unit chord
Y	lateral force, lb., positive right
y	lateral coordinate
$y_1$	lateral position
Z	vertical force, lb., positive downward
$\alpha$	angle of attack, degrees or radians
$\beta$	local slope of body surface or sideslip angle, positive slip right
$\delta$	control deflection
$\epsilon$	downwash at lifting surface
$\eta$	drag proportional factor
$\eta_p$	propeller profile efficiency
$\theta$	pitch angle, degrees or radians
$\Gamma$	dihedral angle, rad

$\Lambda_{l.e.}$	sweep angle of leading edge, degrees
$\lambda_{11}, \lambda_{22}, \lambda_{33}, \lambda_{88}$	generalized aerodynamic derivatives with acceleration
$\mu_x, \mu_y, \mu_z, \mu_{yy}$	potential flow shape factors
$\nu$	kinematic viscosity
$\rho$	density of air, slugs/ft <sup>3</sup>
$\phi$	roll angle or potential, ft <sup>2</sup> /sec.
$\omega_N$	natural frequency, rad/sec.
$\psi$	yaw angle, positive nose right

#### Subscripts

(force or moment)<sub>variable</sub> dimensional partial derivative with respect to variable indicated

#### Other Notations

(')	single differentiation with respect to time
('')	double differentiation with respect to time

## INTRODUCTION

Recent U.S. Navy interest in air vehicles for application to advanced naval missions has pointed out a need for technology development in certain areas to support parametric and point design studies in the Advanced Naval Vehicle Concepts Evaluation (ANVCE) program. Among those technologies requiring study were the aerodynamics and precision hover control characteristics of Lighter-Than-Air (LTA) vehicles.

LTA, or buoyant assisted lift, vehicles offer potentially significant increases in on-station endurance over conventional aircraft. To evaluate fully this potential, however, it is important to have a sound aerodynamic description of these aircraft that can be relied upon to give accurate representations of their performance, stability and control requirements.

The present study is intended to provide a basis for the aerodynamic characterization of LTA vehicles suited to parametric studies, point design and even preliminary design efforts. The study employs combinations of applicable theory, experiment and empiricisms to represent the aerodynamic characteristics of conventional airship (body-of-revolution) and delta shapes, the latter shape having applicability to hybrid aircraft utilizing both aerodynamic and aerostatic lift. Additionally, the potential of boundary layer control for drag reduction in conventional airships is reviewed and the basic aspects of hovering control of LTA vehicles are developed.

## BODIES OF REVOLUTION

This section discusses various methods for predicting the aerodynamic forces and moments acting on bodies of revolution. Only the bare hull is considered. Basically the prediction techniques fall into two broad categories, potential flow theories based on ideal fluid aerodynamics and empirical theories which attempt to account for the real fluid effects in an approximate way. It should be noted that there is no condition corresponding to the Kutta condition for airfoil shaped bodies which can be invoked in connection with the potential flow theories to account for real fluid effects in a consistant and rational manner, thus the empirical theories involve necessarily some apparently arbitrary assumptions. First we consider the results of potential flow theories as they serve as a valuable basis from which to proceed to the empirical approaches which are necessary if good agreement with experiment is desired.

### 1.) Potential Flow Theories

Historically one of the first attempts to predict the forces and moments on bodies of revolution was made my Munk in 1924<sup>1</sup>. Earlier work, which can be found in modern form in References 2 or 3, employed potential theory to predict the forces acting on an ellipsoid of revolution moving with an arbitrary motion through an unbounded fluid. These results are essentially due to Lamb<sup>4</sup>. The results of potential flow theory indicate that if an ellipsoid of revolution is moving in a rectilinear fashion through the fluid the only net effect of the fluid on the body is to produce an unstable couple if the body is moving in a direction near to

its longest axis. Moving in the direction of its shortest axis the couple will be stable. The pitching moment acting on the body for a small angle-of-attack is given by

$$M = \rho \frac{V^2}{2} (\mu_y - \mu_x) C_x$$

where  $\mu_y$  and  $\mu_x$  are functions of the fineness ratio of the body. As the fineness ratio (length/diameter) becomes very large  $\mu_y \rightarrow 1$  and  $\mu_x \rightarrow 0$  and consequently  $M = \rho \frac{V^2}{2} C_x$ .

This limiting result is referred to in many cases in the literature as slender body theory, i.e., the case of very high fineness ratio. Of course as the fineness ratio  $\rightarrow 0$   $\mu_y \rightarrow 0$  and  $\mu_x \rightarrow 1$  and  $M = -\rho \frac{V^2}{2} C_x$  and a stable moment is obtained.

Various other forces and moments are predicted for an ellipsoid of revolution moving in an arbitrary fashion. In general the forces and moments for arbitrary motion can be expressed in a body axis system as

$$X = -\lambda_{11}\dot{u} - \lambda_{22}q w + \lambda_{33}r v$$

$$Y = -\lambda_{33}\dot{v} - \lambda_{11}r u + \lambda_{22}p w$$

$$Z = -\lambda_{22}\dot{w} - \lambda_{33}p v + \lambda_{11}q u$$

$$L = 0$$

$$M = -\lambda_{55}\dot{q} + \lambda_{55}p r + (\lambda_{22} - \lambda_{11}) u w$$

$$N = -\lambda_{55}\dot{r} - \lambda_{55}p q + (\lambda_{11} - \lambda_{22}) u v$$

where

$$\lambda_{11} = \frac{\rho}{2} \mu_x$$

$$\lambda_{22} = \frac{\rho}{2} \mu_y$$

$$\lambda_{33} = \frac{\tilde{I}}{2} \mu_{yy}$$

where  $\mu_x$ ,  $\mu_y$  and  $\mu_{yy}$  are functions of the fineness ratio of the body as shown in Figure 1.

A variety of confusing terminology is found in the literature referring to these forces and moments. They may be referred to as apparent or virtual mass terms. This terminology tends to cause confusion since the implication is that one merely finds the effect of these forces by adding to the mass of the body. Note that this is only the case for a sphere where with a fineness ratio of 1 ( $\lambda_{11} = \lambda_{22}$ ) and the force equations in fact reduce to a coefficient which is the same in all directions times the respective acceleration in that direction. For a body with fineness ratio other than one since  $\lambda_{11} \neq \lambda_{22}$  the apparent masses are different for different motions.

In addition, in the literature<sup>5</sup> associated with missile aerodynamic terms in the force equations involving a product of a rate and a linear velocity such as  $\lambda_{22} q w$  are called Magnus Forces, although this is not at all the usual terminology for Magnus Force which is usually thought of as arising from viscous effects when cylinder or sphere is rotating and moving through a fluid<sup>6</sup>. It is perhaps best just to think of these results as predicting aerodynamic forces and moments depending on acceleration as well as velocity. Normally in the analysis of conventional aircraft dynamics the acceleration dependent terms are neglected owing to the high relative density of the vehicle. In flutter analysis, they are usually included<sup>7</sup>.

Again slender body theory usually refers to the limits of these equations when the fineness ratio becomes very large. In that case

$\mu_x \rightarrow 0$ ,  $\mu_y \rightarrow 1$ ,  $\mu_{yy} \rightarrow 1$  as shown in Figure 1 and the resulting forces and moments become

$$X = \rho V [-q w + r v]$$

$$Y = \rho V [-\dot{v} + p w]$$

$$Z = \rho V [-\dot{w} - p v]$$

$$L = 0$$

$$M = \rho \bar{I} (-\dot{q} + p r) + \rho V u w$$

$$N = \rho \bar{I} (-\dot{r} - p q) - \rho V u v$$

Slender body theory then usually refers to the results given by the equation above. Note that in this case of high-fineness ratio, i.e., slender body theory, all dependence upon body shape has essentially vanished and the overall forces and moments depend only on two gross characteristics of the vehicle, its volume  $V$ , and its displaced fluid moment of inertia  $\bar{I}$ . The above results comprise what might be termed exact potential flow theory which is restricted to bodies of revolution.

The exact theory can also be extended to bodies of elliptical cross section. Reference 3 presents the various coefficients in the force and moment equation for tri-axial ellipsoids as well as bodies of revolution. As an example of the importance of cross section shape, the angle-of-attack stability and directional stability of a tri-axial ellipsoid can be expressed as

$$-N_\beta = \rho V_0^2 V (\mu_x - \mu_y)$$

$$M_\alpha = \rho V_0^2 V (\mu_z - \mu_x)$$

where

$$\mu_x \approx \frac{1}{2} \frac{c}{a}$$

$$\mu_y \approx \left( \frac{c}{b} - \frac{1}{2} \frac{c}{a} \right)$$

$$\mu_z \approx \left( \frac{b}{c} - \frac{1}{2} \frac{b^2}{ac} \right)$$

where  $a$  is the semi-length,  $b$  is the semi-span and  $c$  is the semi-thickness.

The reader is referred to Reference 3 for further details and exact results.

Figure 2 shows the trends in directional stability and angle-of-attack stability given by the above expressions.

For bodies with other than elliptical sections solving the exact problem becomes very difficult. There is an extensive literature which attempts to develop second order corrections to the slender body equations to bring into this theory effects of fineness ratio and the influence of longitudinal distribution of area. Two examples of these highly complex theories are given in References 8 and 9. By and large these theories are very involved and only result in rather small corrections which for the parabolic body examined give trends very similar to the exact ellipsoid results in some cases. In other cases there are marked disagreements between these two theories and the exact ellipsoid. Comparison of the results of References 8 and 9 for a parabolic arc body and the exact ellipsoid results are shown in Figure 3. While there is a large difference shown in the prediction of the total damping parameter ( $M_g + M_q$ ), the absolute level predicted in any case is quite small. Since in general, the exact potential flow results for ellipsoids do not agree well with experimental results, there appears to be little value in considering further these highly complex second order theories.

While in the symmetric flight case, with no angle-of-attack and no side slip it is possible to include the effects of viscosity and predict the drag of a body of revolution, it is a much more complex problem when the angle-of-attack and side slip angles are non-zero. The flow is now fully three-dimensional and there are difficulties even with prediction of the separation line on the body, much less the forces and moments. Consequently methods which will be discussed in the next section are essentially of an empirical nature.

One additional piece of information which can be obtained from potential flow theory is the nature of the pressure distribution and the local force distribution over the body. For the very slender body, the local force distribution in rectilinear flight can be expressed as

$$\frac{dL}{dx} = \frac{\rho U^2}{2} \frac{ds}{dx} \sin 2\alpha$$

This result is based on the assumption that the flow in each cross section plane is that of a circular cylinder, i.e., it is essentially a two-dimensional theory in the cross flow plane<sup>10</sup>. This formula is sometimes modified by the factors discussed previously for an ellipsoid of revolution to read

$$\frac{dL}{dx} \approx \frac{\rho U^2}{2} (k_2 - k_1) \frac{ds}{dx} \sin 2\alpha$$

These approximations essentially work well when the body cross section area is not changing rapidly, i.e., at the very nose of the vehicle they tend to give less than satisfactory results as

shown in Figure 4. An even better approximation to the local force loading can be obtained by using the exact result for the ellipsoid of revolution. The exact result is<sup>11</sup>

$$\frac{dF}{dx} = \frac{1}{2} \rho U^2 \sin 2\alpha \frac{dS}{dx} \left[ \frac{1}{2} (1 + k_1) (1 + k_2) \right] \cos^2 \beta$$

The angle  $\beta$  is the local slope of the body surface. Upson in Reference 12 simplifies this expression by noting that  $\frac{1}{2} (1 + k_1)(1 + k_2) \approx 1$  over the entire range of fineness ratios and consequently suggests using

$$\frac{dF}{dx} \approx \frac{1}{2} \rho U^2 \sin 2\alpha \frac{dS}{dx} \cos^2 \beta$$

and argues that this result may be used for bodies with other than elliptical plan form. Upson shows excellent agreement between this result and experiment on the forward portions of the body. Some comparisons are shown in Figure 4. The approximate result of Munk is also shown. It can be seen that this equally simple result given above gives a much better result near the nose where the cross section is changing rapidly than Munk's result. Apparently Upson's result, which was originally given by Jones<sup>13</sup> is not much used although it gives considerably better results than Munk.

For bodies with a cross sectional shape, other than a circle, i.e., other than bodies of revolution, the expression for the transverse force can be generalized as indicated by Jones<sup>14</sup> by viewing the problem in an unsteady reference frame. This approach yields for the force,

$$\frac{dF}{dx} = U^2 \alpha \frac{dM'}{dx}$$

where  $M'$  is the apparent mass of the cross section. Recall this result is only for very slender bodies. The apparent mass for various cross section shapes is given by Nielsen<sup>5</sup>. Note that for cylindrical cross section, a flat plate cross section, and an elliptical cross section with the same lateral dimension or span, the apparent mass will be the same, thus

indicating theoretically that all of these cross section shapes will produce the same transverse force according to slender body theory. The local pressure distribution on each of these bodies will be quite different however, as shown in Figure 5 for a cylindrical cross section and a flat plate or wing. These distributions have complications with regard to force distribution on a wing as discussed in a later section. Again recall these results are for a very high fineness ratio body and in effect do not depend on fineness ratio, and consequently cannot be expected to give good agreement with experiment in regions where the body cross section shape is changing rapidly. Upson's simple modification appears to handle this problem quite well for circular cross sections.

Now we turn to the question of comparison of theory with experiment. It can be seen from the pressure distributions shown in Figure 4 that on the parts of the body where the area is increasing, the agreement between experiment and potential flow theory is quite good as given by Von Karman's double source method or Upson's ellipsoid result. Downstream of the maximum cross section however, there is a marked discrepancy between any of the theories and experiment. This large discrepancy is no doubt a result of the adverse pressure gradients causing separated flow. In addition to the lack of agreement on the transverse forces it can be seen that this discrepancy which is characteristic of all comparisons of experimental data and potential theories on bodies of revolution will give rise to a transverse force or lift due to angle-of-attack and a somewhat smaller moment (about the center of buoyancy) than is predicted by theory.

Consequently, recourse must be made to modification to the theory. At this time, it appears fair to say that a brute force approach of attempting to solve the complete, exact problem by including viscosity and predicting the separation line, etc., is probably not possible. Even the problem of determining separation in a true three-dimensional flow, as distinguished from the axi-symmetric case at zero angle-of-attack, is a difficult if not impossible problem at the present time. Therefore, recourse must be had to semi-empirical techniques.

<sup>11</sup> Thwaites discusses in detail more general methods for solving for the potential flow fields about bodies of revolution employing various distributions of singularities (sources and sinks) to represent various body shapes. Since, with the exception of obtaining a good prediction of the force distribution from the nose of the body to the region of maximum diameter, the potential flow theories are not too successful at predicting overall forces and moments these more complex methods are not discussed.

The next section therefore treats the empirical approaches.

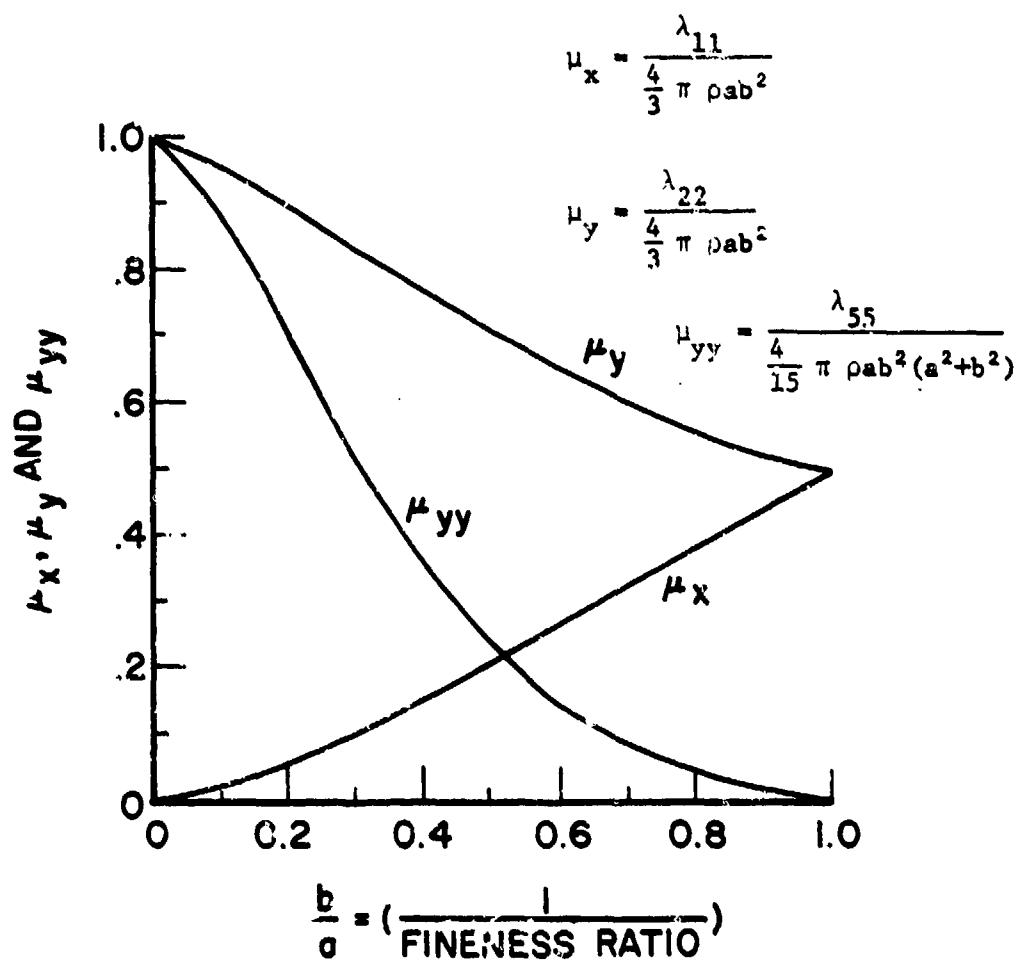
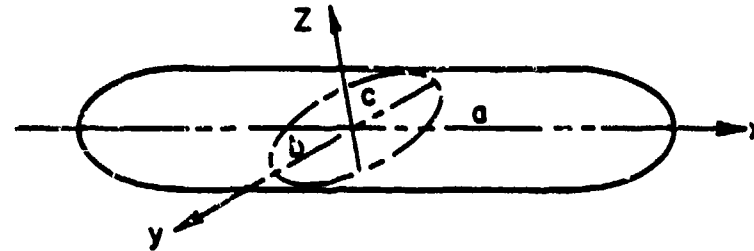


FIGURE 1. Dimensionless Coefficients for Forces and Moments Acting on Ellipsoid of Revolution From Potential Flow Theory

"EXACT" THEORY FOR ELLIPSOIDS



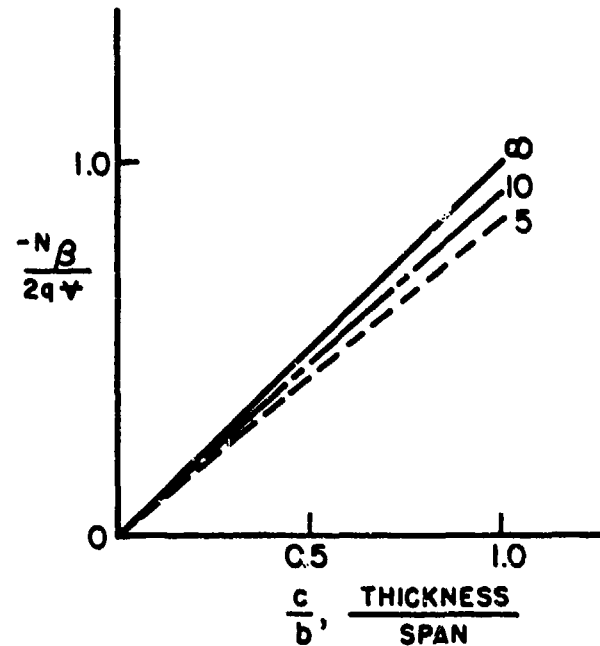
APPROXIMATE APPARENT MASS

$$\mu_x \approx \rho \nabla \left\{ \frac{1}{2} \frac{c}{a} \right\}$$

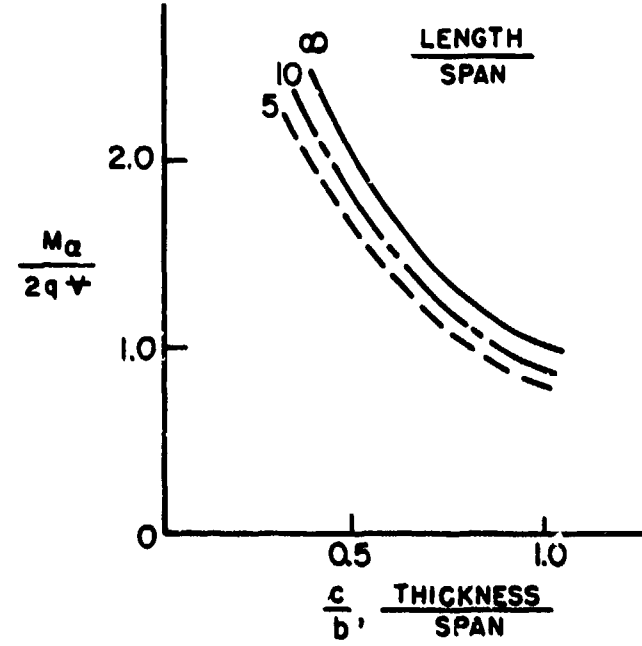
$$\mu_y \approx \rho \nabla \left\{ \frac{c}{b} - \frac{1}{2} \frac{c}{a} \right\}$$

(APPROXIMATIONS)

$$\mu_z \approx \rho \nabla \left\{ \frac{b}{c} - \frac{1}{2} \frac{b^2}{ac} \right\}$$



$$-N_\beta = \rho U_0^2 (\mu_x - \mu_y)$$



$$Ma = \rho U_0^2 (\mu_z - \mu_x)$$

FIGURE 2. Variation in Angle of Attack Stability and Directional Stability for Tri-Axial Ellipsoid Potential Flow Theory

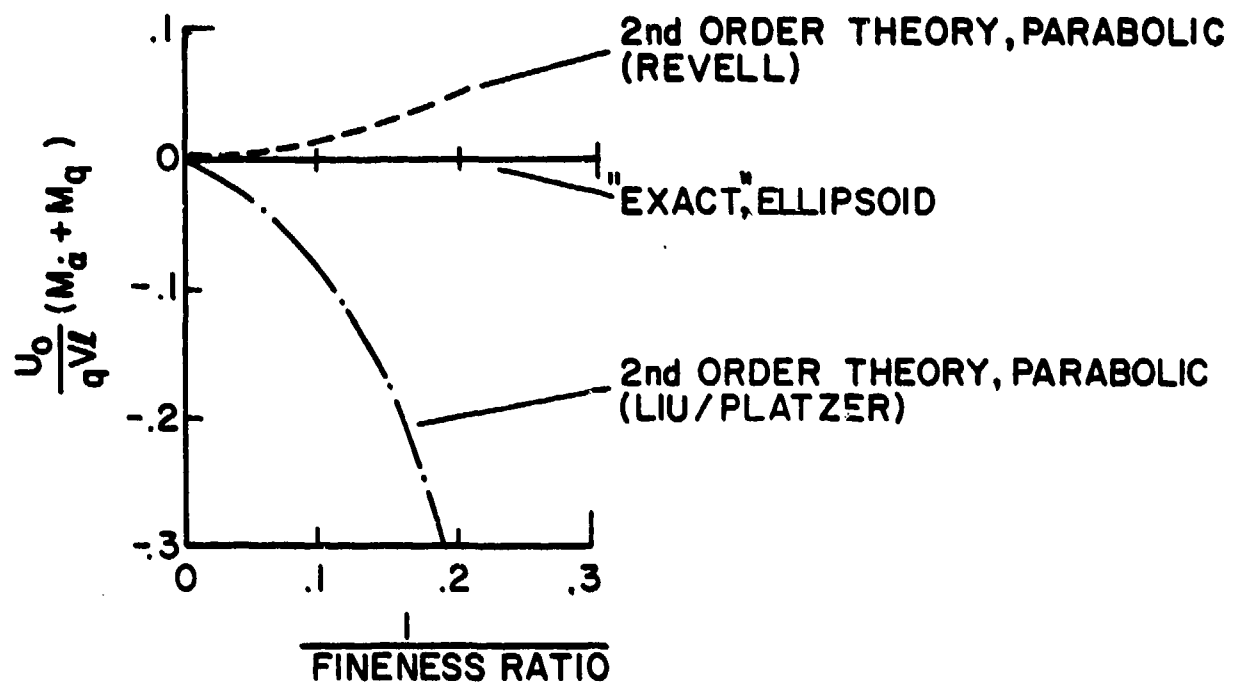
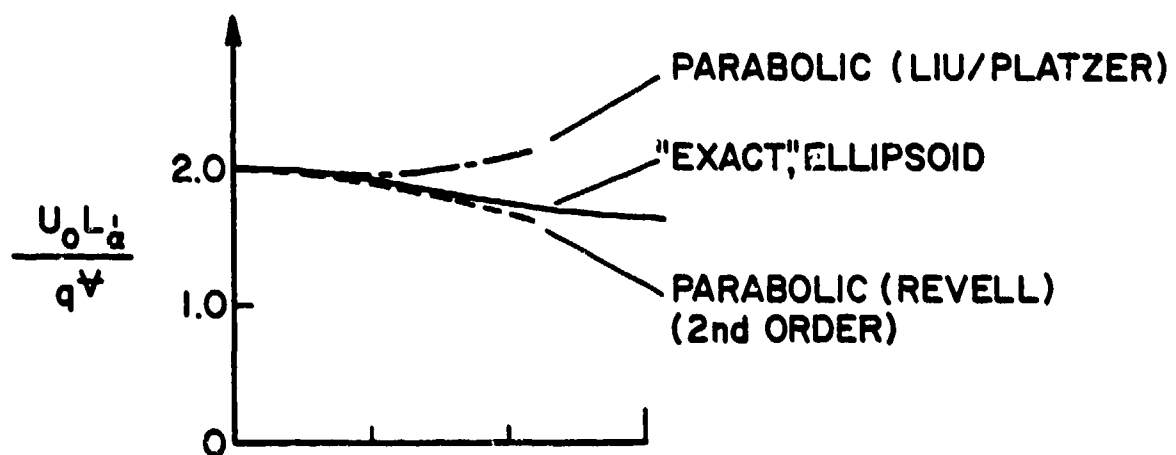
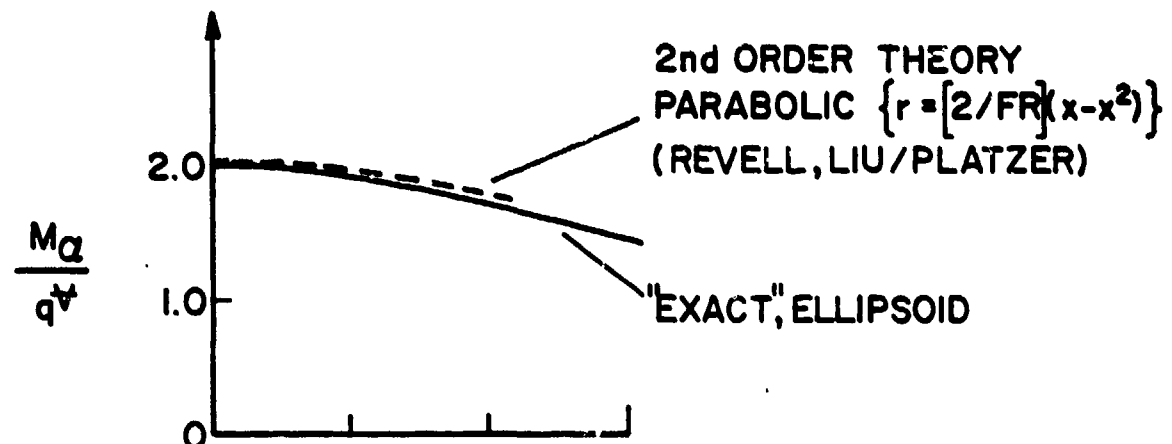


FIGURE 3. Second Order Theory Results: Parabolic Body of Revolution Compared with Exact Theory for Ellipsoid Potential Flow

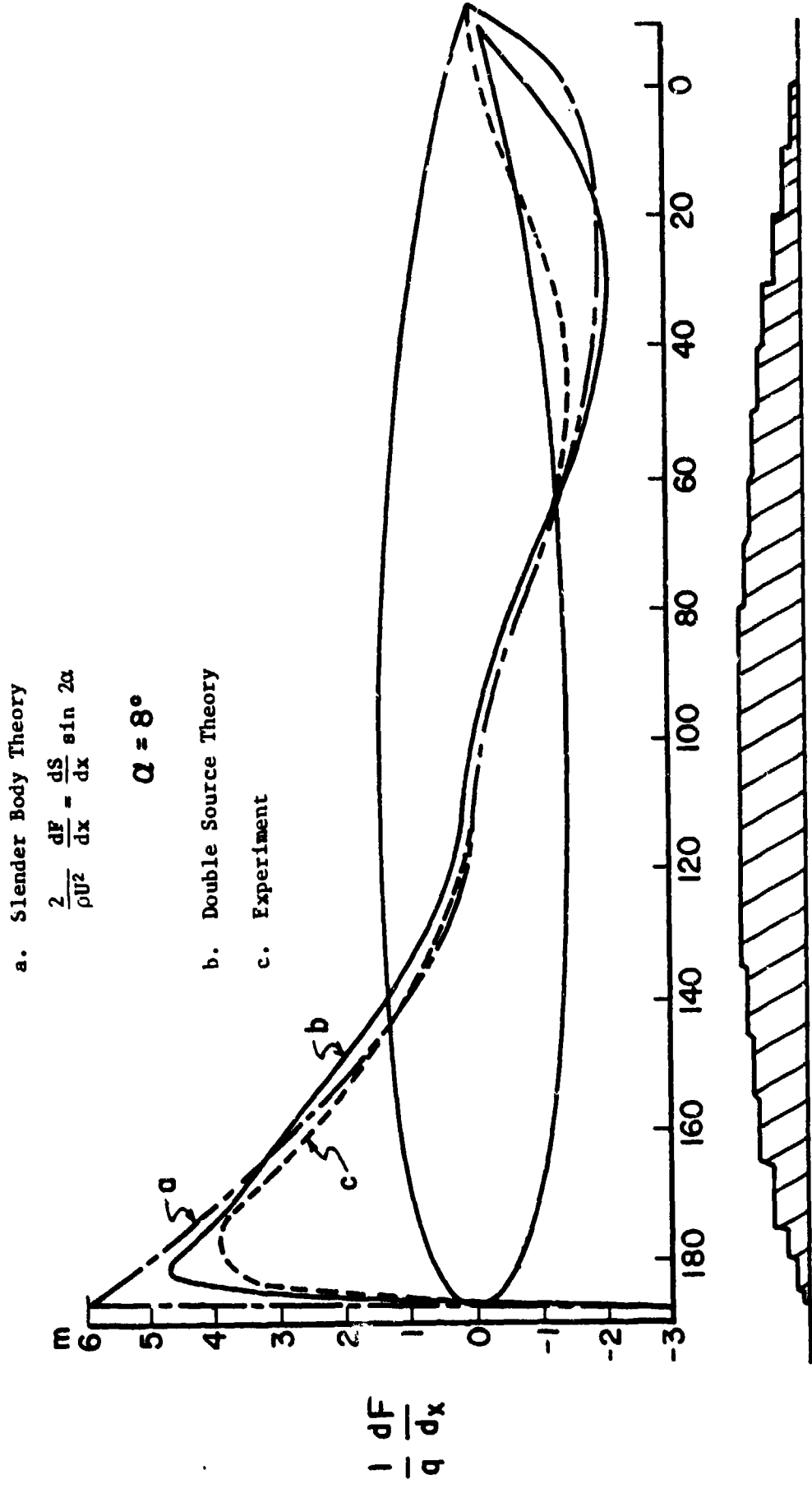


FIGURE 4. Comparison of Theory and Experiment for Loading on Slender Body  
at Angle of Attack

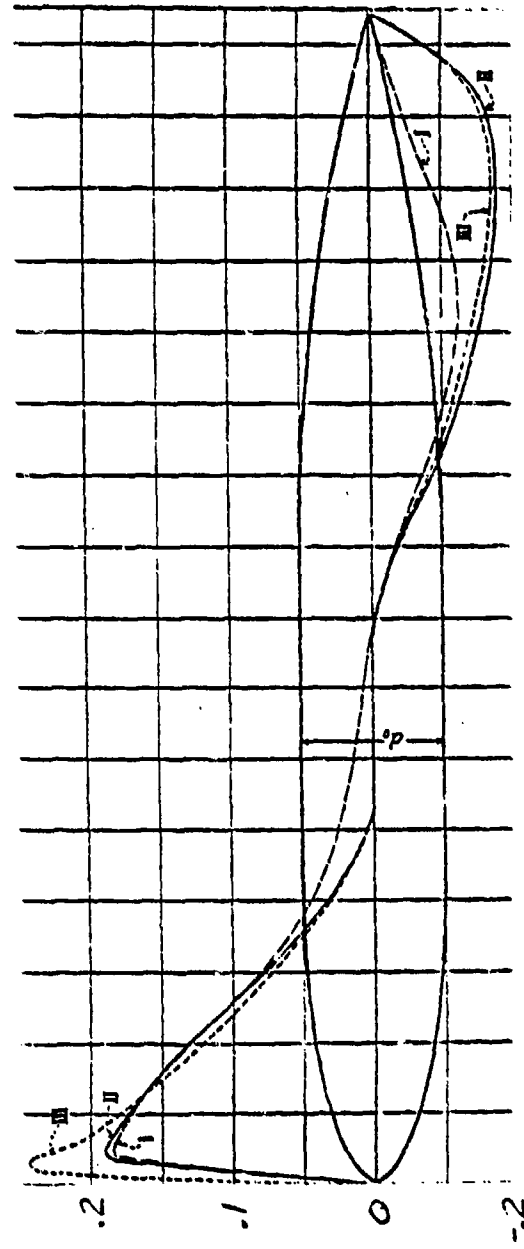
I Experimental Results (RSM 801)

II Exact Ellipsoid Theory

$$\frac{1}{\rho U^2} \frac{1}{d_o} \frac{dp}{dx} = \frac{1}{d_o} \frac{ds}{dx} \sin 2\alpha \cos^2 \beta$$

III Munk's Formula

$$\frac{1}{\rho U^2} \frac{1}{d_o} \frac{dp}{dx} = \frac{1}{d_o} \frac{ds}{dx} (k_2 - k_1) \sin 2\alpha$$



$$\frac{1}{\rho U^2} \frac{1}{d_o} \frac{dp}{dx}$$

Airship R 33

$\alpha = 10^\circ$

FIGURE 4. Comparison of Theory and Experiment for Loading on Slender Body at Angle of Attack (continued)

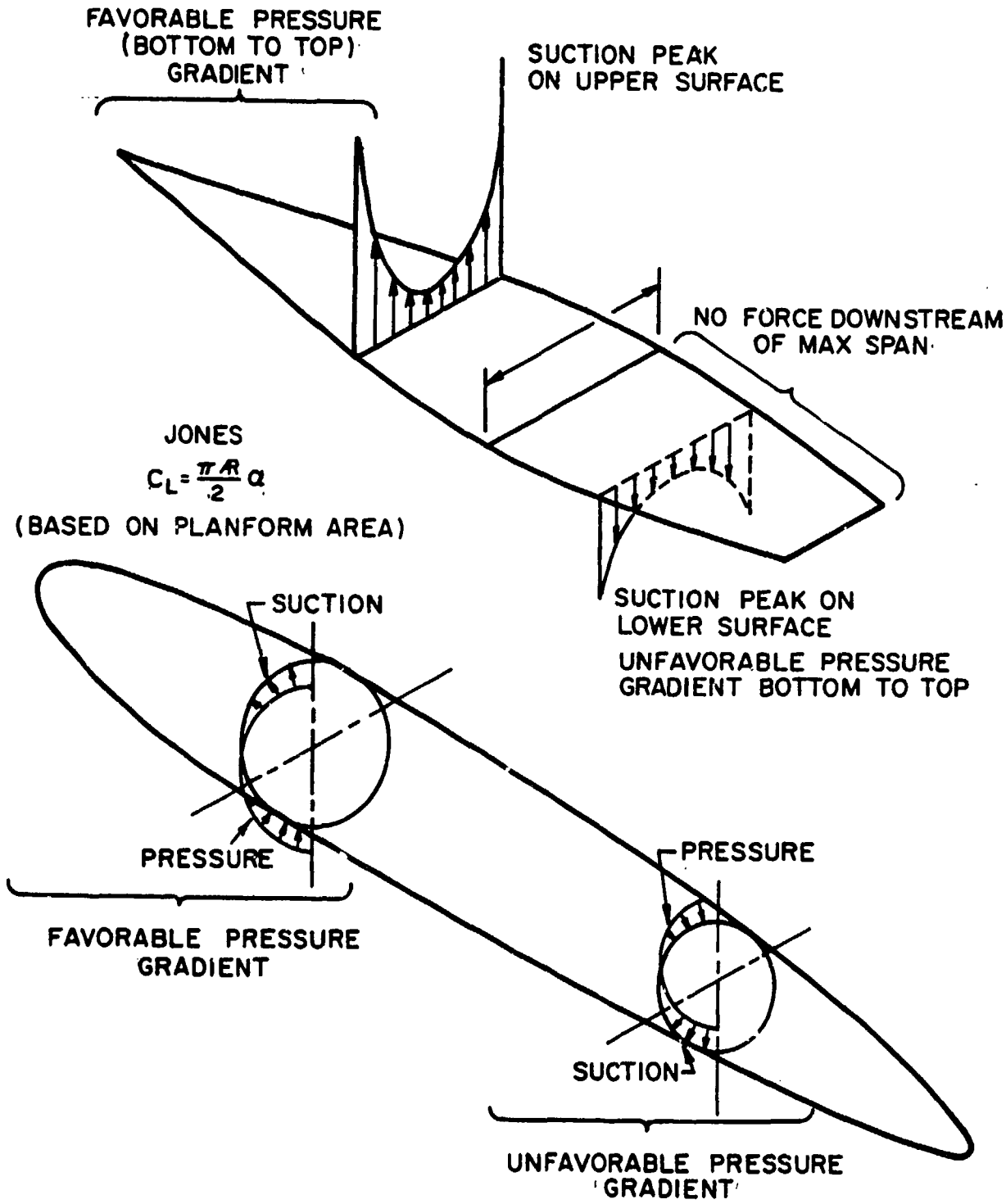


FIGURE 5. Local Loading on Flat Body and Body of Revolution

## 2.) Empirical Approaches

As discussed in the previous section potential flow theories applied to slender bodies of revolution characteristically break down when attempting to predict the pressures on the body downstream of the maximum diameter. This deviation between theory and experiment is of course a result of the viscosity of the real fluid and consequent boundary layer which thickens and eventually separates at some location on the body. This discrepancy in pressure distribution also implies of course that the overall lift and moment will not be predicted.

In addition to the separation of the boundary layer as a result of adverse pressure gradients a pair of vortices will be formed on the lee side of the body which tend to induce an additional flow field and further influence the actual pressure distribution. Excellent physical descriptions of this three-dimensional flow field are given in Thwaites' (Ref. 11), Peake, Rainbird, and Atraghji (Ref. 15) and Wang (Ref. 16). The development of separated flow and the departure of the measured pressure distribution from the theoretical distribution is shown in Figure 6. The development of the adverse pressure gradient around the circumference can be seen from this figure as well as the marked departure of the experimental results at these locations.

The two empirical theories to be discussed are based on the fundamental idea that for slender bodies, the flow may be assumed to be two-dimensional in planes normal to the longitudinal axis of the body, and that in any specific cross flow plane a suitable model for the force on a two-dimensional

cylinder of infinite length may be used to predict the force on that particular slice of the body (Figure 7).

Two empirical theories are discussed, that due to Allen (Ref. 17 and 18) and that due to Hopkins (Ref. 19). To determine the resultant forces and moments Allen takes the potential flow result for the body of revolution and simply adds to the potential flow term a viscous correction which consists simply of the drag force experienced by a circular cylinder in a flow velocity of ( $U \sin \alpha$ ), the flow component perpendicular to the section. The analytical expressions for the lift, drag and pitching moment given by Allen are:

$$C_N = \frac{(k_2 - k_1) \sin 2\alpha \cos \frac{\alpha}{2}}{(\text{Vol.})^{2/3}} \int_0^l \frac{ds}{dx} dx + \frac{2\eta \sin^3 \alpha \cos \alpha}{(\text{Vol.})^{2/3}} \int_0^l r C_{d_c} dx$$

$$C_D = \frac{(k_2 - k_1) \sin 2\alpha \sin \frac{\alpha}{2}}{(\text{Vol.})^{2/3}} \int_0^l \frac{ds}{dx} dx + \frac{2\eta \sin^3 \alpha}{(\text{Vol.})^{2/3}} \int_0^l r C_{d_c} dx + C_{D_\alpha} = 0$$

$$C_M = \frac{(k_2 - k_1) \sin 2\alpha \cos \frac{\alpha}{2}}{\text{Vol.}} \int_0^l \frac{ds}{dx} (x_m - x) dx + \frac{2\eta \sin^3 \alpha}{\text{Vol.}} \int_0^l r C_{d_c} (x_m - x) dx$$

where  $C_{d_c}$  is the sectional drag coefficient per unit length of a circular cylinder normal to the air stream and given as a function of the cross flow Reynolds number in Figure 8. The  $\eta$  term is required because the drag coefficient of a finite length cylinder is less than the infinite cylinder value. The value of  $\eta$  as a function of the body slenderness ratio is given in Figure 9.

In considering Allen's equations, it should be noted that the first integral term in each equation is the contribution that results from potential flow. As with Munk's analysis, for closed bodies this term is equal

to zero in the normal force and drag force equations. The second integral term represents the contribution due to viscous forces acting on the body.

Considerable simplification of Allen's equations is possible if the following substitutions are made:

$$A_b = \int_0^l \frac{ds}{dx} dx \quad \text{and} \quad \frac{1}{2} A_p = \int_0^l r dx$$

Furthermore, if it is assumed that the variation over the body  $c_{d_c}$  due to Reynolds number changes is small, and a small angle assumption is

imposed, then Allen's equations reduce to

$$C_N = 2 \left( \frac{A_b}{(\text{Vol.})^{2/3}} \right) \alpha + \eta c_{d_c} \left( \frac{A_p}{(\text{Vol.})^{2/3}} \right) \alpha^2$$

$$\Delta C_D = C_D - C_{D\alpha=0} = \left( \frac{A_b}{(\text{Vol.})^{2/3}} \right) \alpha^2 + \eta c_{d_c} \left( \frac{A_p}{(\text{Vol.})^{2/3}} \right) \alpha^3$$

$$C_M = 2 \left[ \frac{V - A_b (l - x_m)}{\text{Vol.}} \right] \alpha + \eta c_{d_c} \left( \frac{A_p}{\text{Vol.}} \right) (x_m - x_p) \alpha^2$$

where

$A_b$  = body base area at  $x = l$

$A_p$  = planform area of body

Vol. = body volume

$\Delta C_D$  = increase in body coefficient above that at an angle-of-attack of zero degrees.

Allen's method of predicting forces and moments yields good correlations with experiment for normal force and incremental drag force on bodies of revolution with truncated tails ( $A_b \neq 0$ ). The prediction of the pitching moment, although an improvement over potential theory is

still not entirely satisfactory. It should be noted however, that Allen only considers a very special class of shapes more characteristic of artillery shells rather than airship hulls. His technique does not seem to work so well for airship hulls as will be discussed below. In addition all of Allen's bodies have a finite downstream area  $A_b$  which in fact leads to a reasonable prediction of the lift and moment at very small angles-of-attack from potential flow theory alone. However, it is significant that after over twenty five years, Allen's method is not only still very much in use (Ref. 20), but also that the theoretical model is the basis for some very recent work, such as, that of Marshall and Deffenbaugh (Ref. 21), in which the empirically determined viscous term  $C_{d_c}$ , is replaced by a theoretical calculation of the cross-flow drag. Agreement with experiment, however, was inadequate and it was necessary to impose an empirical correction factor which is dependent on the geometry of the body to obtain satisfactory results. Presently, although this technique is an improvement over Allen in having less dependence on empirical inputs, it does not seem worthwhile to attempt to further refine a rather crude theory. It is not clear why Allen chooses to add the two results and refinements such as calculating the cross flow drag coefficient based on cross flow Reynolds number do not appear to be justified for bodies such as airship hulls where the cross section is continuously changing in contrast to an artillery shell or missile where there is a long section of constant radius.

Due to the inadequacies of Allen's method for determining pitching moments, Hopkins (Ref. 19) was motivated to propose an approach to the problem which is quite similar but seems physically more plausible.

In this approach, which is similar to that suggested by Multhopp (Ref. 22), the body is divided into a forward portion over which the potential flow solution is applied and an aft portion over which the empirical viscous cross-flow solution is applied (Figure 10). There appears to be still one physical aspect of the problem that is not modelled. In general, it would be expected that the separation line on the body for any appreciable angle-of-attack would not lie in a plane normal to the longitudinal axis, as can be seen by the location of the points of minimum pressure on a body of revolution as shown in Figure 11. Hopkins' resulting equations are:

$$C_N = \frac{(k_2 - k_1) 2\alpha}{(\text{Vol.})^{2/3}} \int_0^{x_0} \frac{dS}{dx} dx + \frac{2\alpha^2}{(\text{Vol.})^{2/3}} \int_{x_0}^l \eta r c_{dc} dx$$

$$\Delta C_D = \frac{(k_2 - k_1) 2\alpha}{(\text{Vol.})^{2/3}} \int_0^{x_0} \frac{dS}{dx} dx + \frac{2\alpha^2}{(\text{Vol.})^{2/3}} \int_{x_0}^l \eta c_{dc} dx$$

$$C_M = \frac{(k_2 - k_1) 2\alpha}{\text{Vol.}} \int_0^{x_0} \frac{dS}{dx} (x_m - x) dx + \frac{2\alpha^2}{\text{Vol.}} \int_{x_0}^l \eta r c_{dc} (x_m - x) dx$$

These equations are essentially the same as those of Allen except for the limits of integration. The endpoint of integration,  $x_0$ , was found experimentally to correlate to the point on the body,  $x_1$ , where  $\frac{dS}{dx}$  reaches its most negative value. Thus, the empirically determined relationship

between  $x_0$  and  $x_1$  which produces the best agreement with experimental findings for some fifteen bodies of revolution considered in Hopkins' paper is presented in Figure 12 and the different body geometries are detailed in Figure 13.

The forces and moments as calculated by each of the techniques thus far discussed, potential flow, Allen's technique, and Hopkins' technique, are compared in Figure 14. The potential flow term used in Hopkins' equations is also plotted simultaneously in this figure so that the relative importance of the terms in the solution can be ascertained. In examining this figure, it is apparent that the prediction which best correlates with experiment, particularly for bodies most resembling those of conventional airship hulls, is obtained by using Hopkins' technique. It is further interesting to note that while Allen's equations generate a solution which, for close bodies, predicts lift and drag solely dependent on the viscous term, the Hopkins' solution depends largely on its potential flow contribution. Consequently, Hopkins' model is much more consistant with the physics of the problem than that of Allen because of the fact that potential flow theory does result in reasonable prediction of the flow over most of the body and only breaks down in the far aft portions because of the effects of fluid viscosity. Therefore, Hopkins' equations are recommended for the prediction of the forces and moments on bodies of revolution because of good agreement with experiment as well as based on a better physical picture.

For the determination of the overall drag coefficient for a body of revolution, it is necessary to evaluate the zero-lift drag coefficient,  $C_{D_{\alpha=0}}$ , which must then be summed with the incremental drag increase due to angle-of-attack,  $\Delta C_D$ , as calculated using the appropriate equation from Hopkins. The simplest approach to drag prediction at zero angle-of-attack is based on the empirical formula given in Hoerner (Ref. 23)

$$C_{D_{\alpha=0}} = C_f [4 (\frac{L}{d})^{0.33} + 6 (\frac{d}{L})^{1.2} + 24 (\frac{d}{L})^{2.7}]$$

where  $(\frac{L}{d})$  is the fineness ratio of the body and  $C_f$  is the flat-plate friction coefficient which is given as a function of Reynolds number in Figure 15. In considering the above equation, the first two terms in the brackets account for skin friction drag, while the third term accounts for drag due to separation. This equation is plotted for a typical case as a function of fineness ratio in Figure 16.

Although it is doubtful that preliminary airship performance or stability and control design studies require a more accurate calculation of  $C_{D_{\alpha=0}}$  than provided by Hoerner's formula, particularly if used in conjunction with other approximate methods outlined herein, the reader should be aware that several more sophisticated techniques are available which, unlike Hoerner's formula, attempt to account for the effect on drag of actual body shape rather than just fineness ratio (References 24 - 29). As noted in Myring (Reference 17), changes in shape for a body of fixed fineness ratio may lead to changes in drag per unit surface area of up to 10 percent. Depending on what phase of design a particular airship is in when a drag calculation is needed, this may or may not be of critical importance.

Conceptually, all of the more rigorous drag prediction techniques (References 24 - 29) model the flow over a streamline body at zero angle-of-attack as starting from a stagnation point on the nose of the body as shown at point A in Figure 17. From this point, a laminar boundary-layer is present for some distance, followed by a transition region, T, after which the boundary-layer becomes fully turbulent. From the tail of the body, the boundary layer continues downstream as a wake. Typically in each of these techniques, the boundary-layer development is calculated by means of momentum integral type boundary-layer equations as it occurs under the particular pressure distribution on the body (References 30 - 32). The location of the transition region, normally assumed to occur at a point, is determined by empirical or semi-empirical criteria. Finally, using boundary-layer parameters, such as, momentum thickness, shape factor, and velocity ratio, all at the trailing edge of the body, the total drag can be calculated by means of Granville's formula (Reference 26) or Young's formula (Reference 24). The differences between the several methods referenced are primarily associated with varying degrees of sophistication in the equations modelling the flow in one particular flow region or another. All in all, the technique outlined in the paper by Cebeci, Mosinskis, and Smith (Reference 27) most represents the current theoretical state-of-the-art in which the zero-lift drag coefficients on streamline airship-like bodies at high Reynolds number can be predicted to within a few percent.

Essential to the prediction of zero-lift drag on bodies of lower

fineness ratios, on which substantial portions of separated flow exist, is the accurate determination of the line of separation. This problem is considered qualitatively in References 11, 15 and 16. Cebeci, Mosinskis, and Smith (Ref. 33) outline a semi-empirical, theoretical approach which produces results very close to experiment in the somewhat limited comparisons shown. Once developed fully and integrated into use with the problem at hand, such techniques could improve even further the prediction of the zero-lift drag on a body of revolution.

This more complex approach however, can not really be extended at this time to the nonsymmetric case. Consequently, extension of the cross-flow ideas of slender body theory, including viscous effects through the use of cross-flow drag coefficient appear satisfactory for forces and moments. Recent efforts to refine Allen's work are given in the paper of Marshall and Deffenbaugh (Ref. 21). However, the technique of Hopkins appears more consistant with the actual physics of the problem, but also seems to offer the best compromise between effort and results presently available for prediction of the aerodynamic characteristics of airship-like bodies. As for the zero-lift drag calculation, reasonable first-order results can be obtained from Hoerner's purely empirical formula (Ref. 23). The ability to predict the zero-lift drag with extreme accuracy currently exists; however, the rigor that is required to obtain it hardly seems justified if the results are to be used in conjunction with the other predictive techniques recommended herein. And finally, the future development of purely theoretical

techniques of determining the forces and moments on bodies of revolution in nonsymmetric flight is doubtful because of the difficulty in treating the turbulent boundary-layer equations in three-dimensional flow as well as predicting separation. While exact solutions to the problem involving only laminar boundary-layers are becoming available (Ref. 34), it is a safe assumption that the turbulent flow solution will always contain some degree of empiricism.

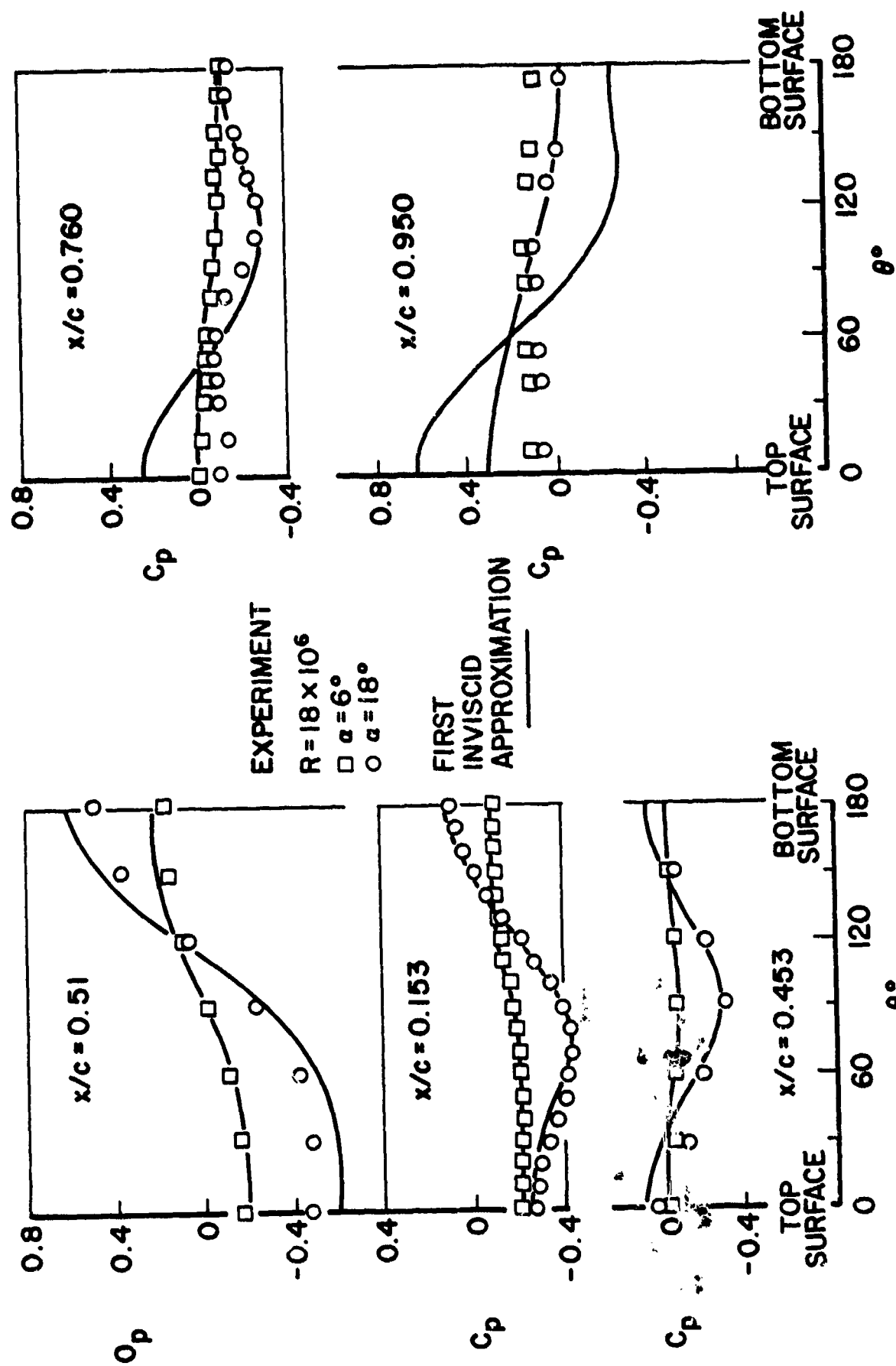


FIGURE 6. Circumferential Distribution of Pressure on Airship "Akron"; Comparison of Theory and Experiment

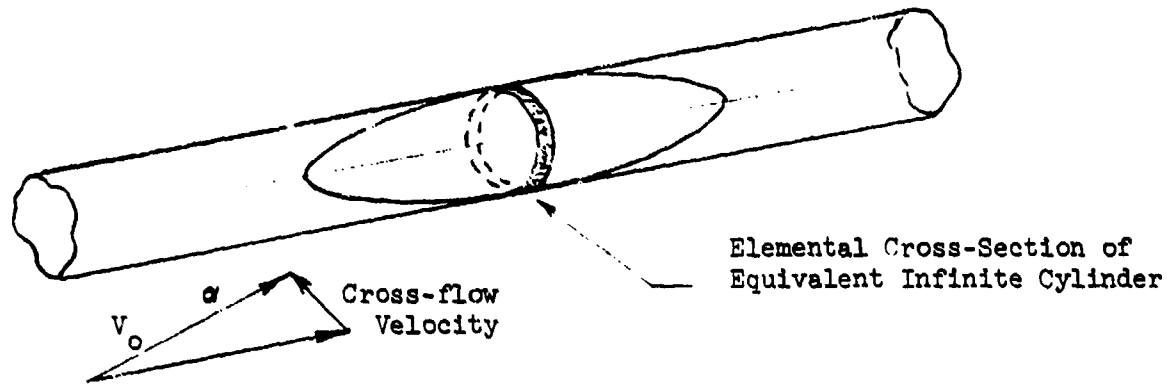


Figure 7. Body of Revolution in Inclined Flow Field.

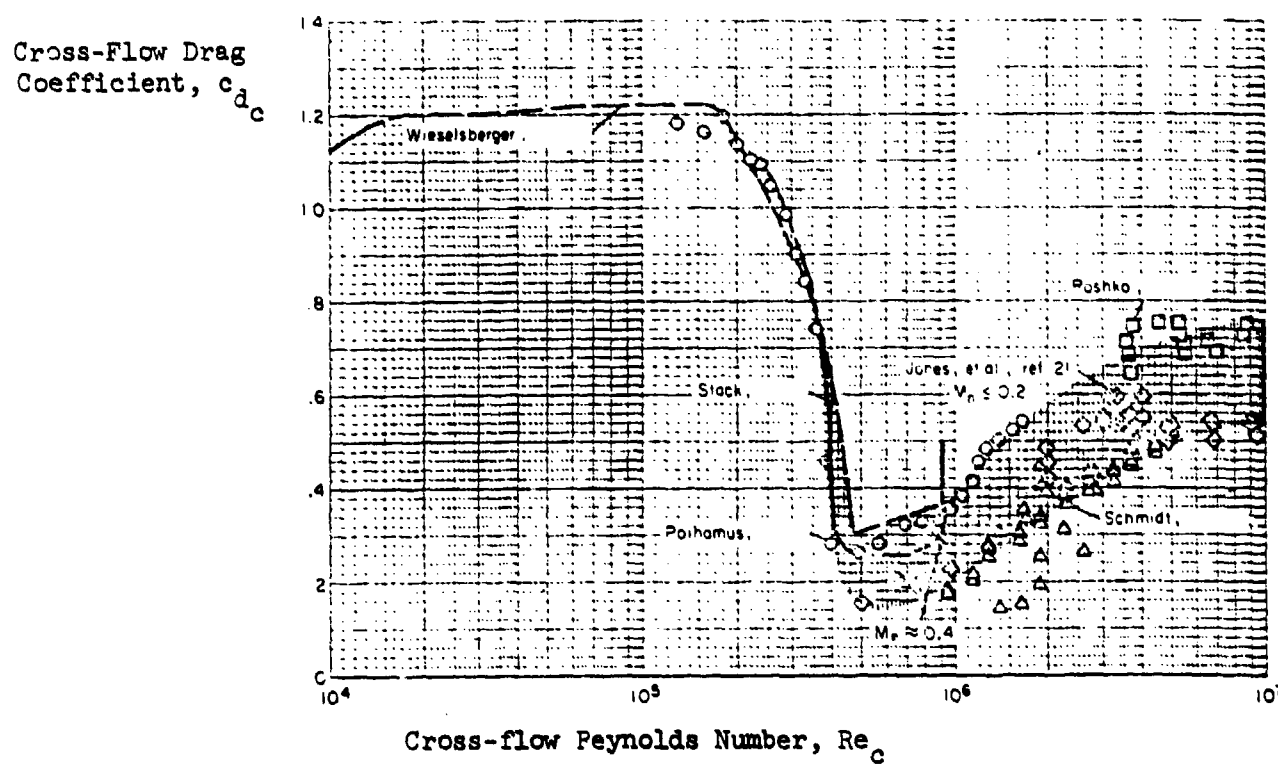


Figure 8. Variation of Cross-flow drag Coefficient with Cross-flow Reynolds Number for Circular Cylinders (From Reference 7).

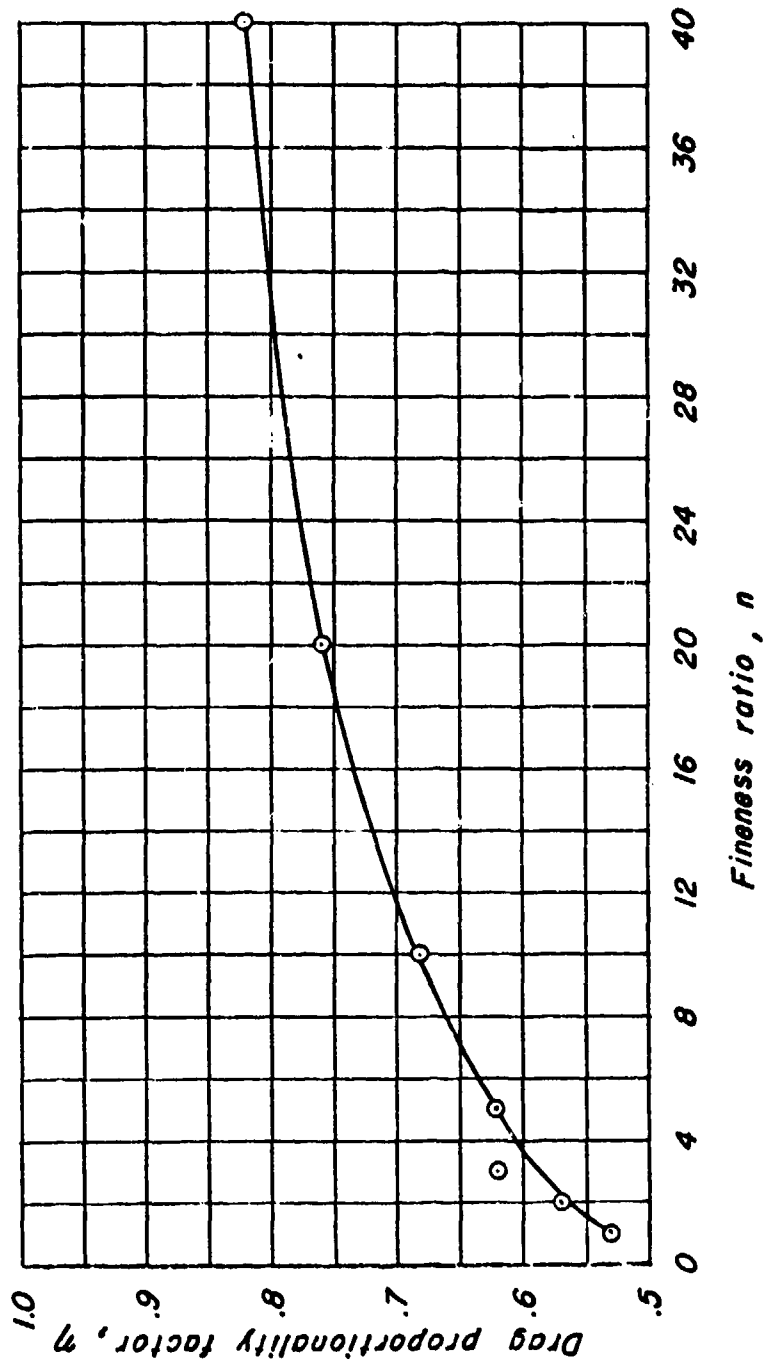
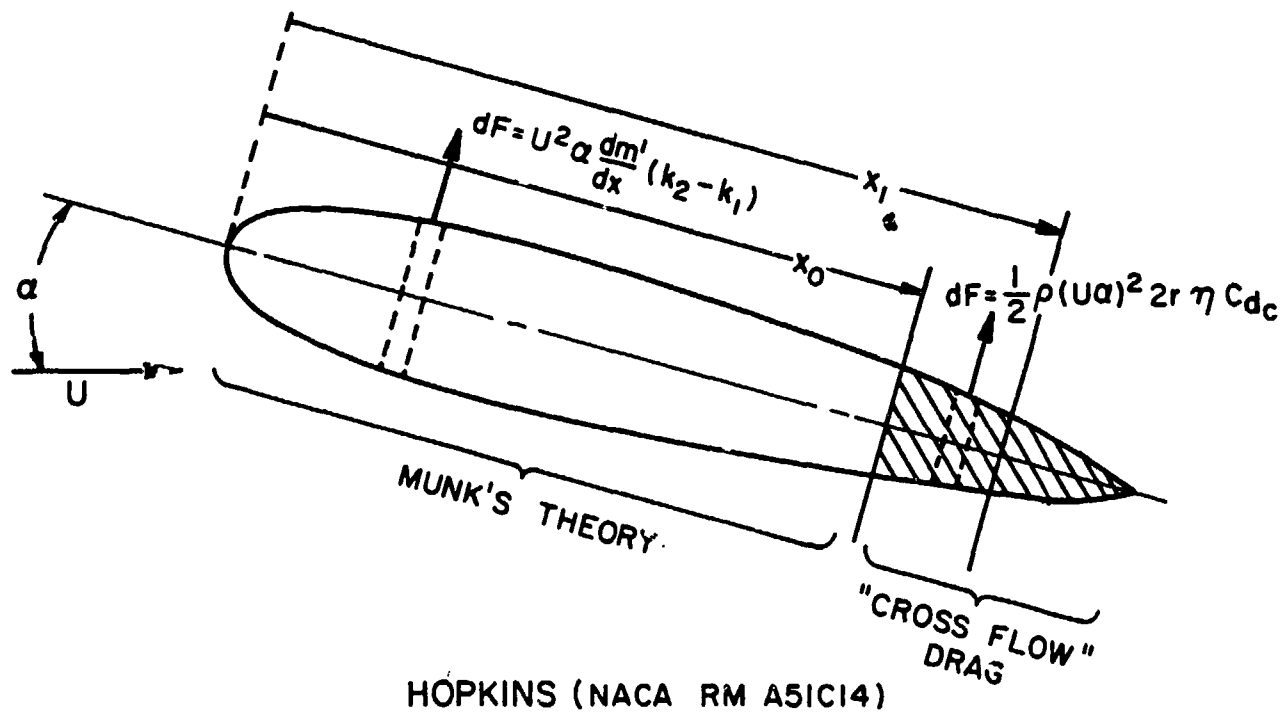
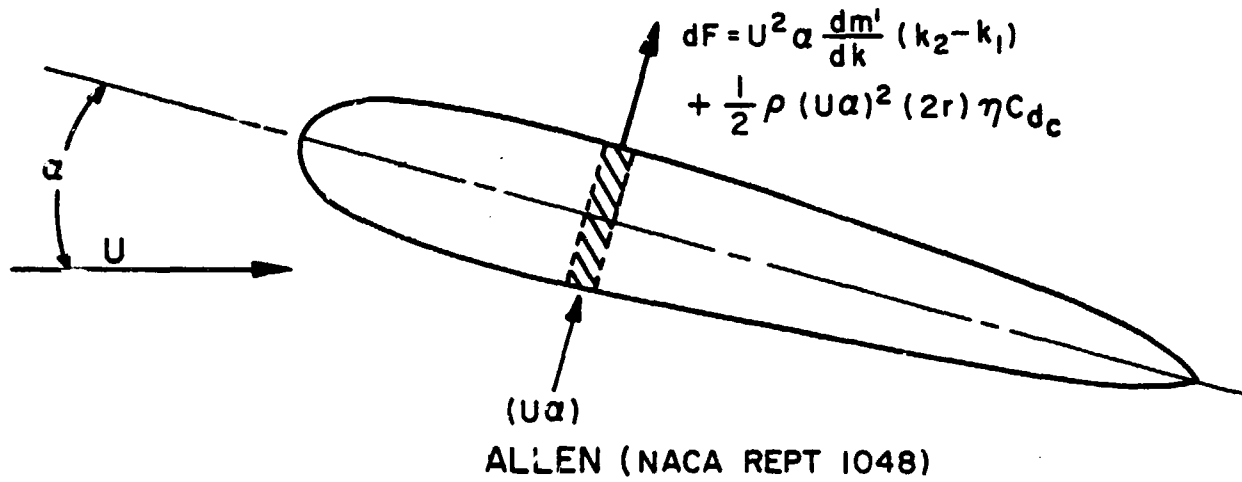


Figure 9. Ratio of the Drag Coefficient of a Circular Cylinder of Finite Length to That of a Cylinder of Infinite Length as a Function of the Fineness Ratio.  $Re_c = 88,000$ .

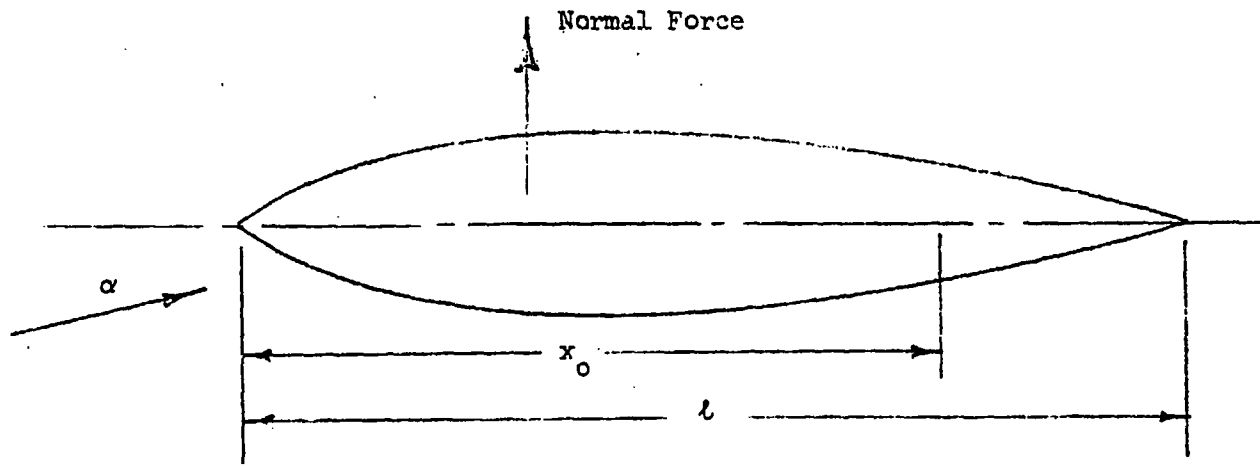


HOPKINS (NACA RM A5IC14)

$$x_0 = f(x_1)$$

$$x_0 = x_1 \text{ WHERE } \frac{ds}{dx} \text{ IS MAX. NEGATIVE}$$

FIGURE 10. Schematic Diagram of Hopkins Flow Model for the Determination of Forces and Moments on Bodies of Revolution



$$\text{Forces and Moments} = \int_0^{x_0} \text{Potential Flow Contribution} + \int_{x_0}^l \text{Viscous Cross-flow Contribution}$$

Figure 10. Schematic Diagram of Hopkins Flow Model for the Determination of Forces and Moments on Bodies of Revolution. (continued)

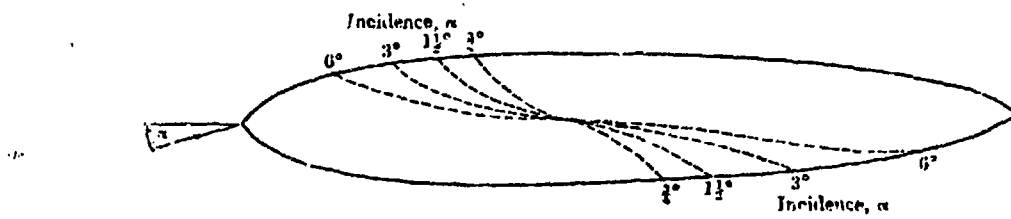


Figure 11. Calculated Loci of Minimum Pressure Positions on Airship "Akron".

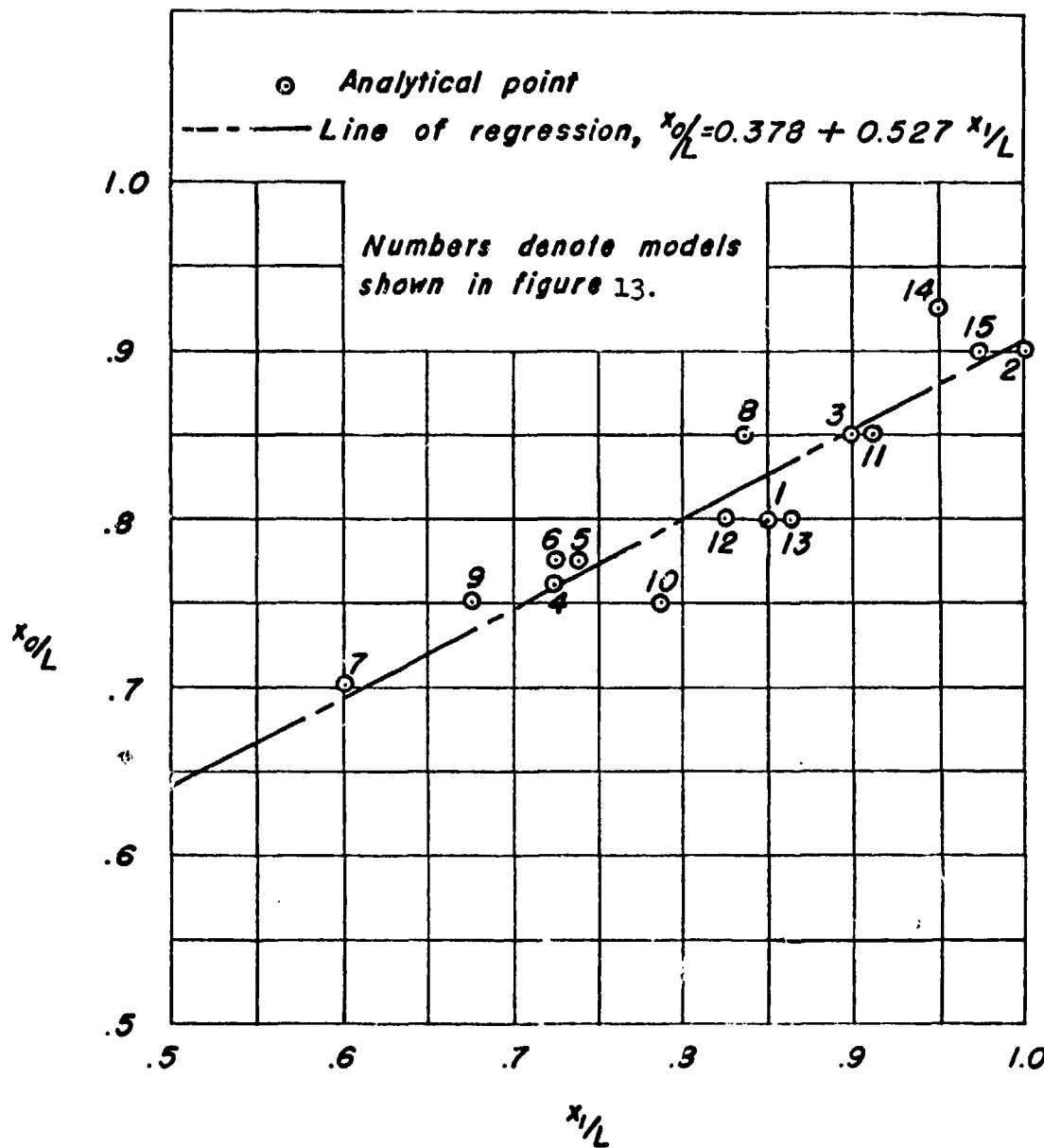


Figure 12. Correlation Between Assumed Extent of Applicability of Potential Theory and the Position of the Maximum Negative Rate of Change of Body Cross-sectional Area With Body Length.

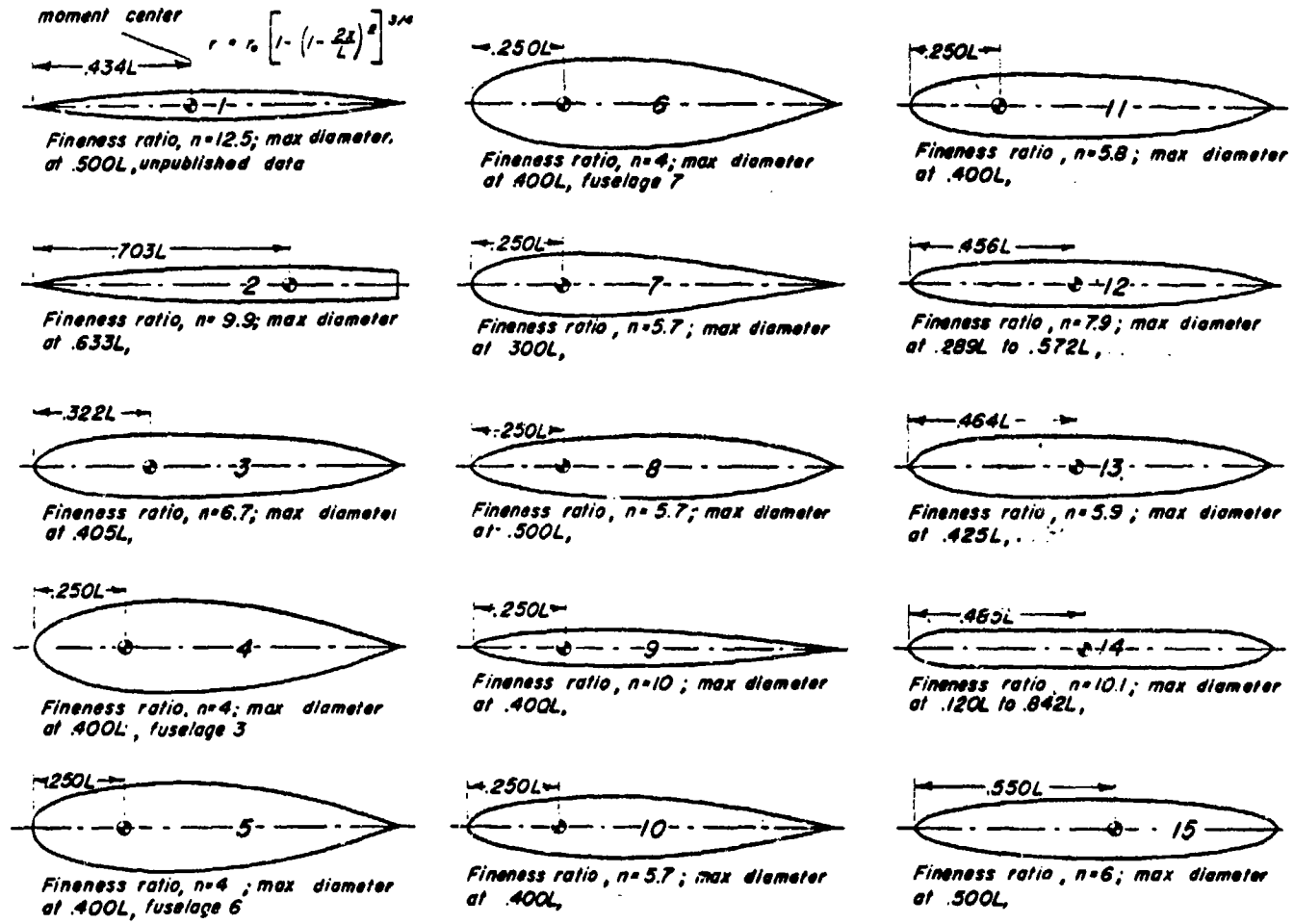


Figure 13. Model Geometries Used in the Development of Hopkins Theory.

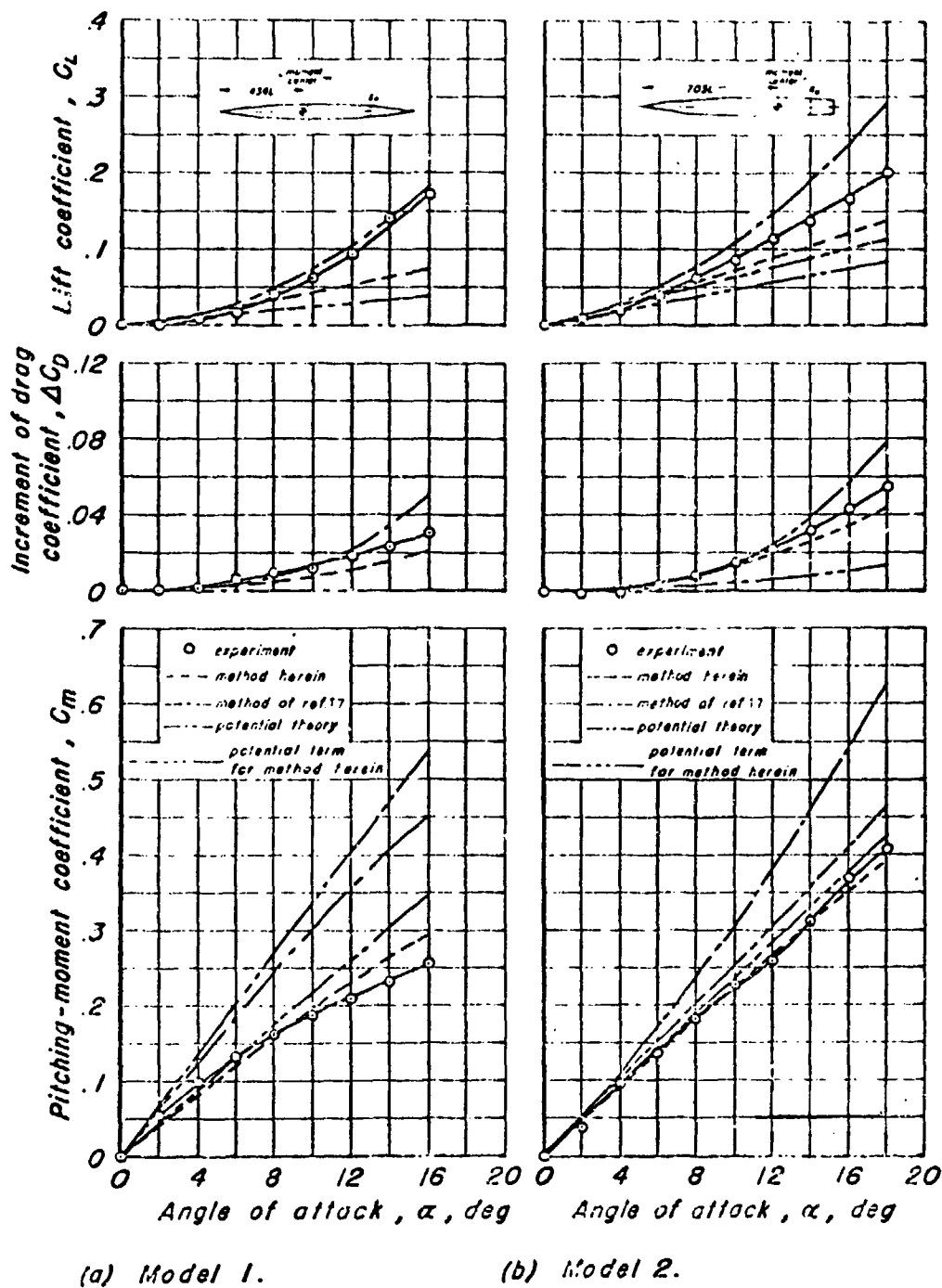


Figure 14. Comparison Between the Experimental and the Estimated Lift, Drag, and Pitching-Moment Characteristics of Various Bodies of Revolution.

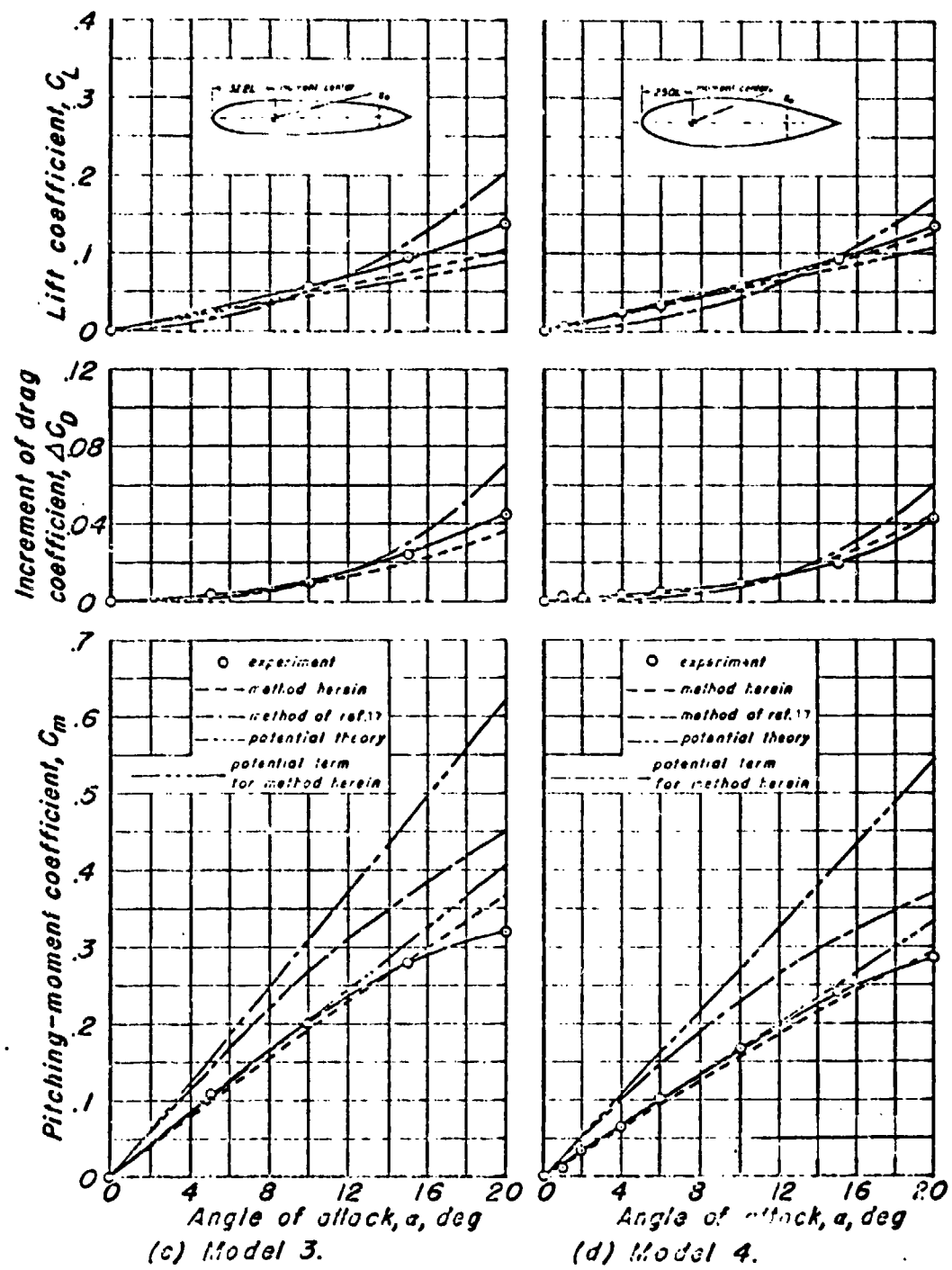


Figure 14. Continued.

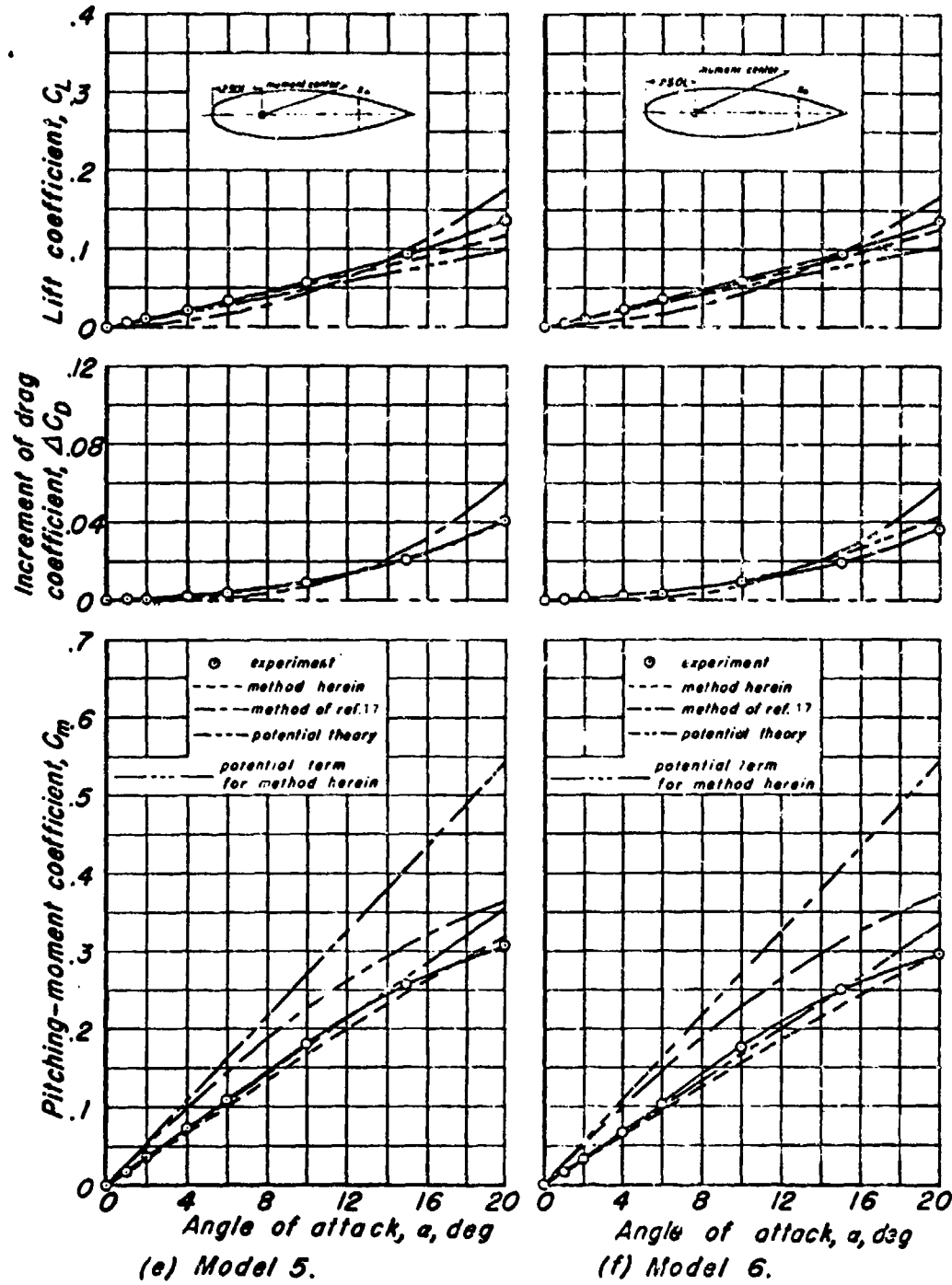


Figure 14. Continued.

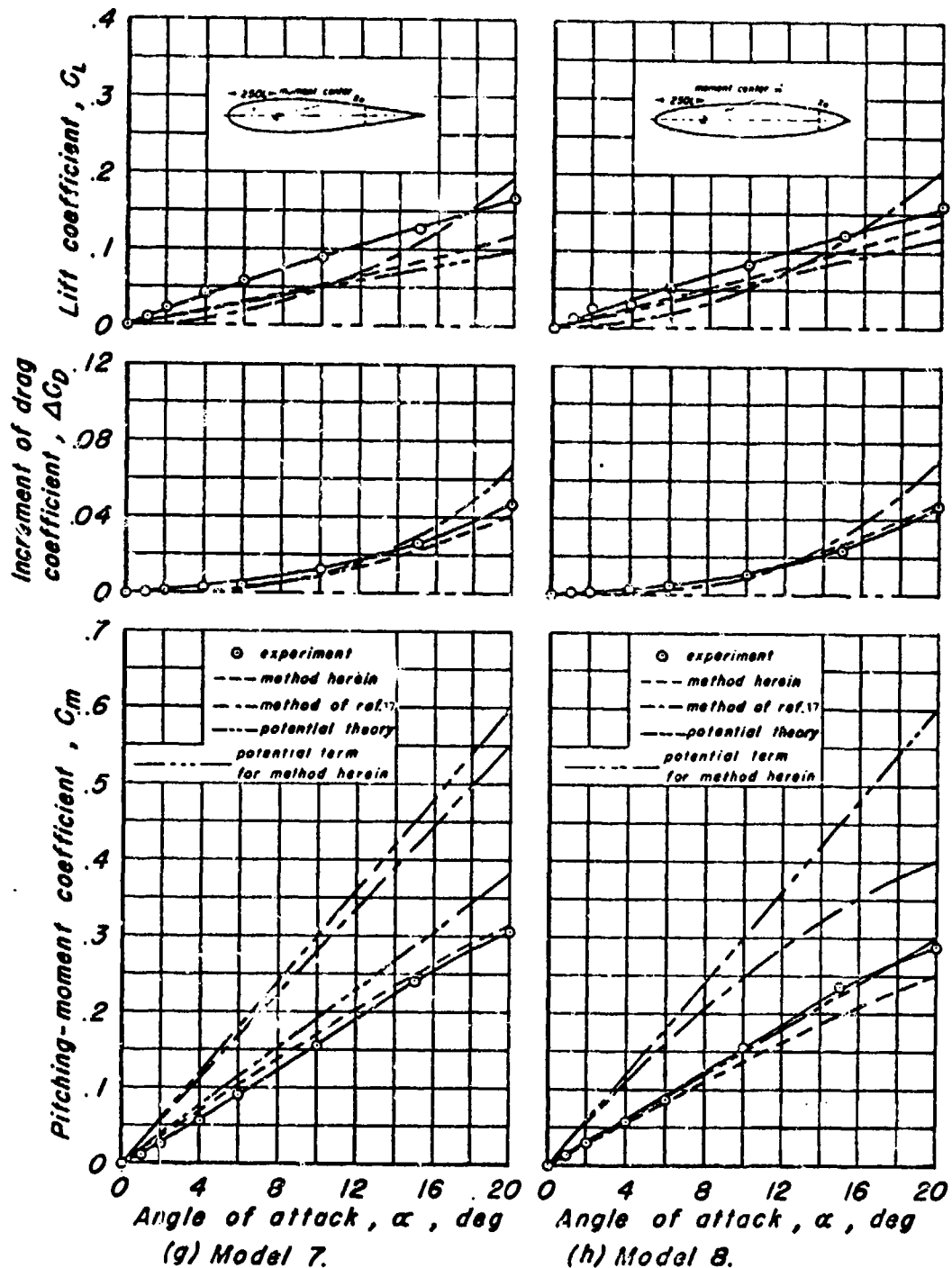


Figure 14. Continued.

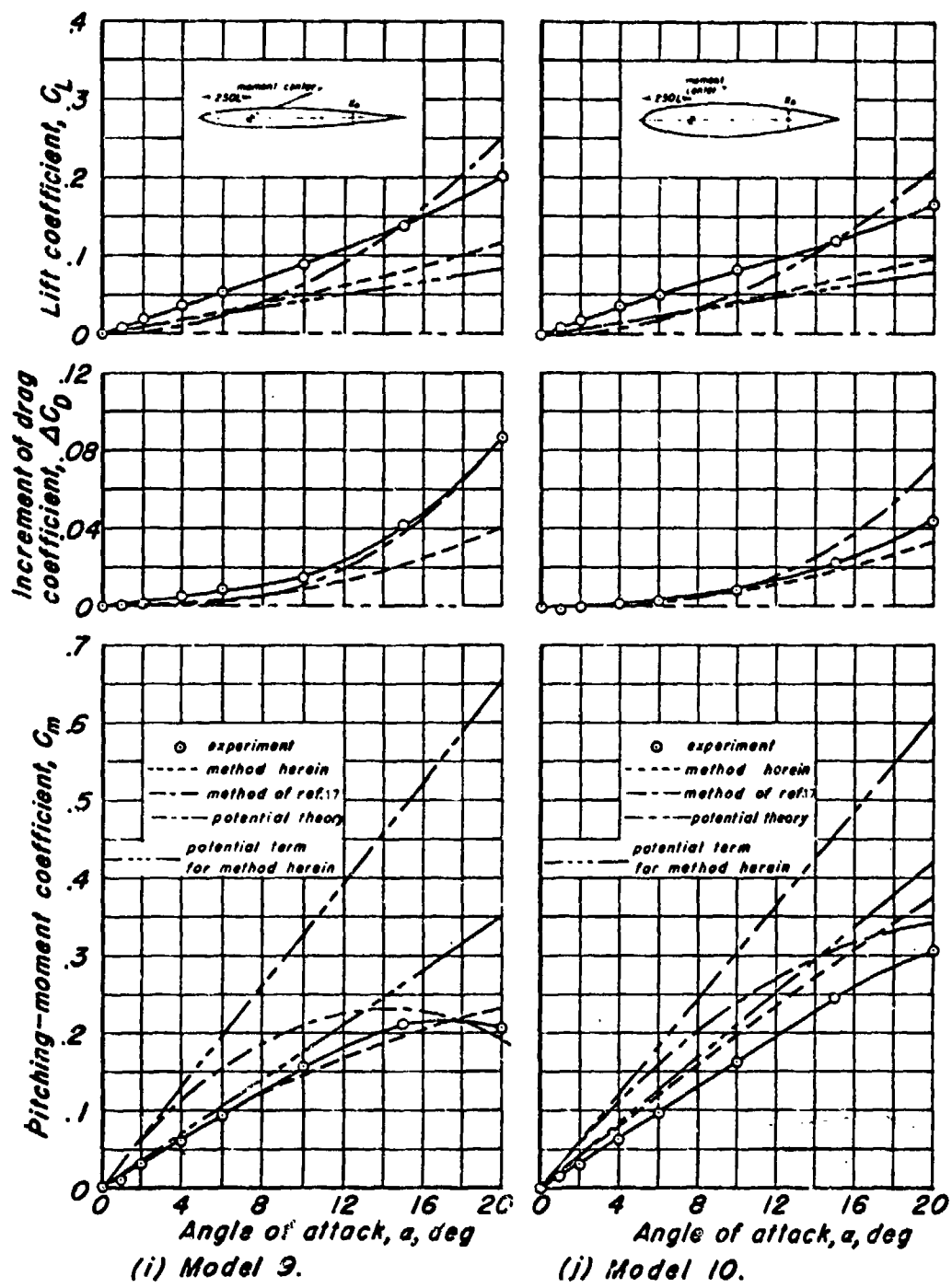


Figure 14. Continued.

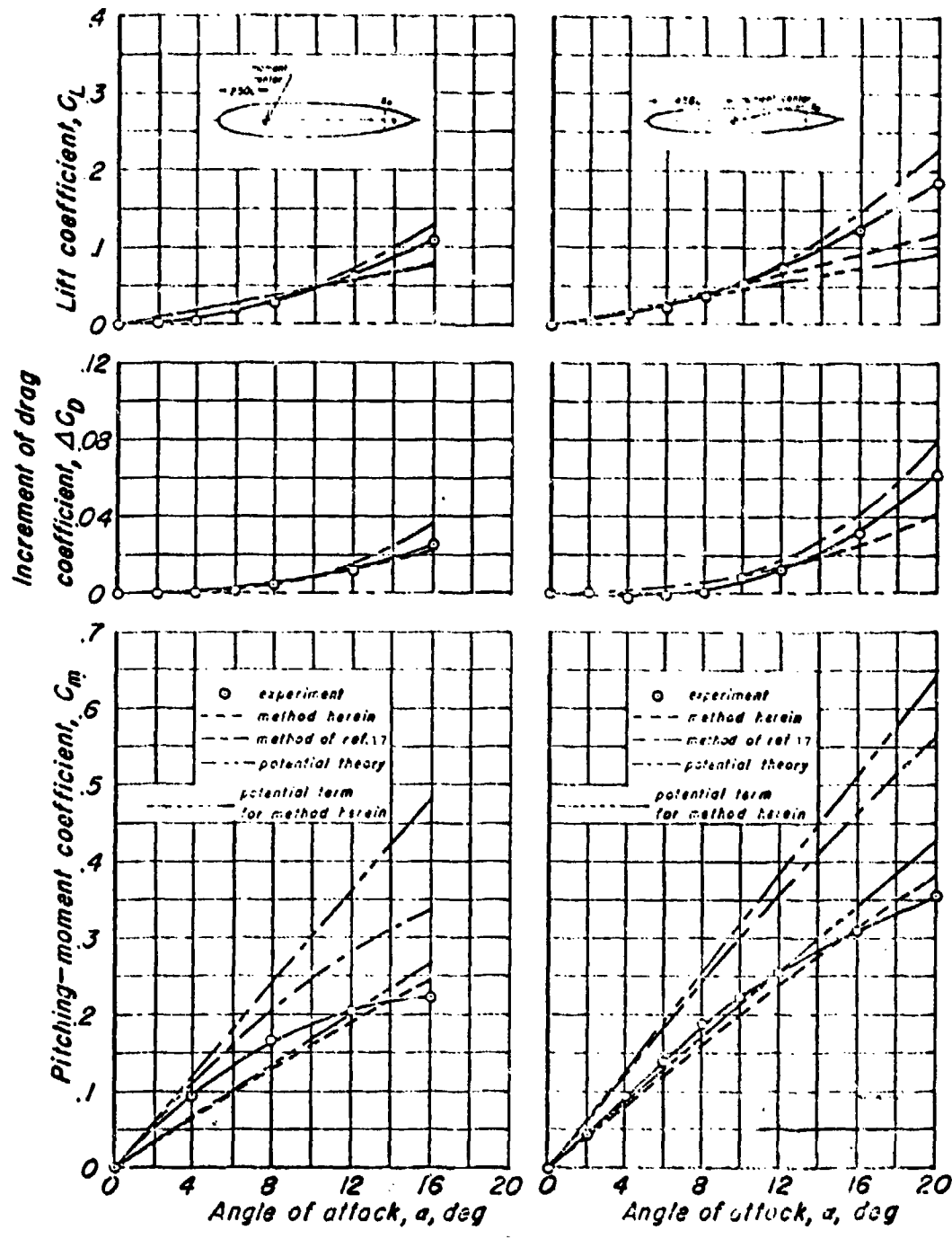


Figure 14. Continued.

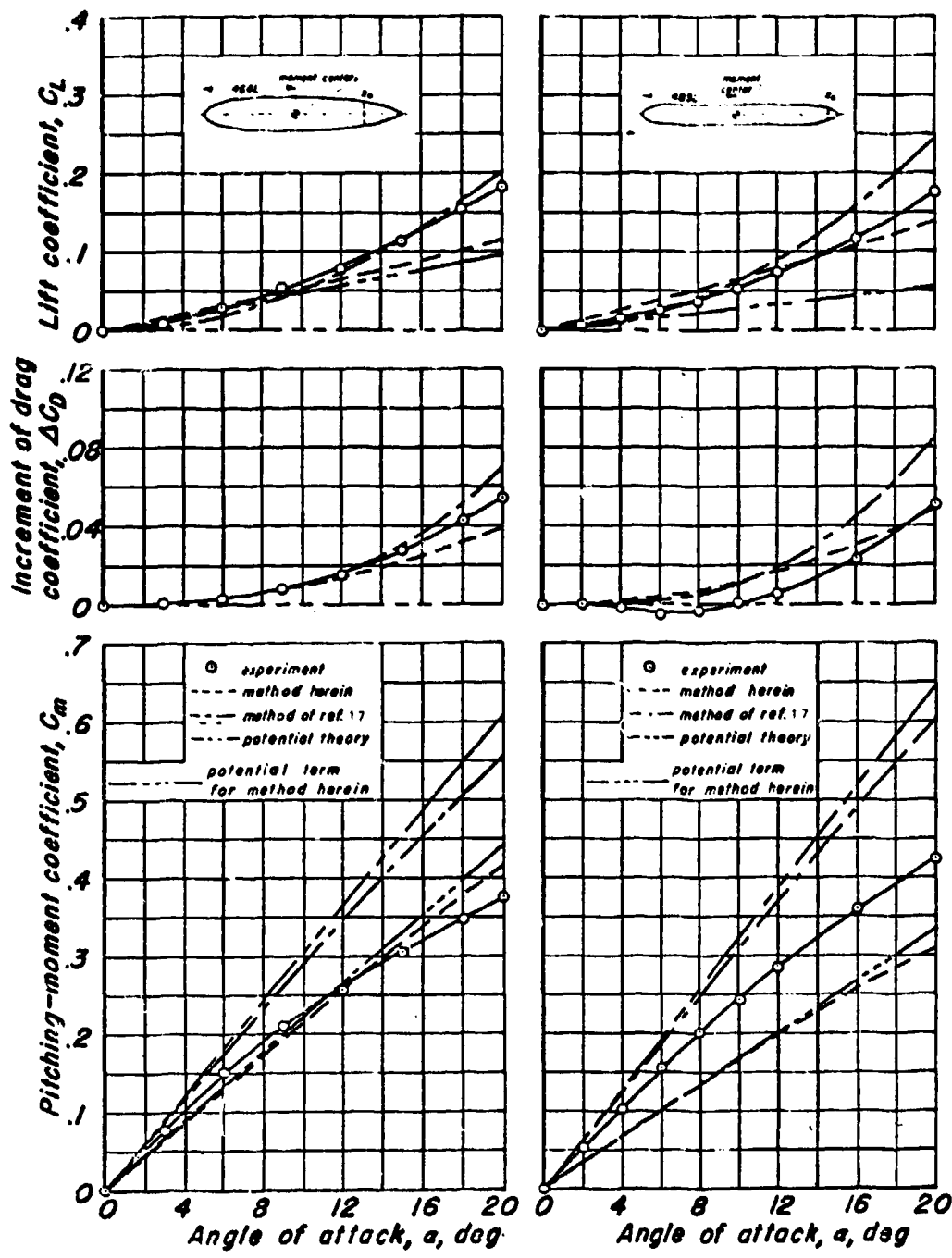


Figure 14. Continued.

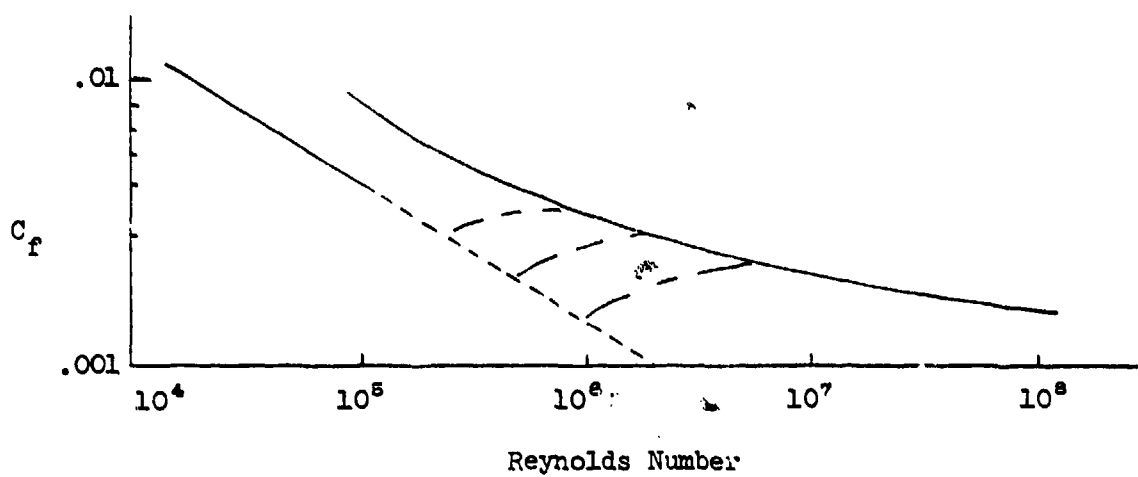


Figure 15. Skin Friction Drag Coefficient as a Function of Reynolds Number.

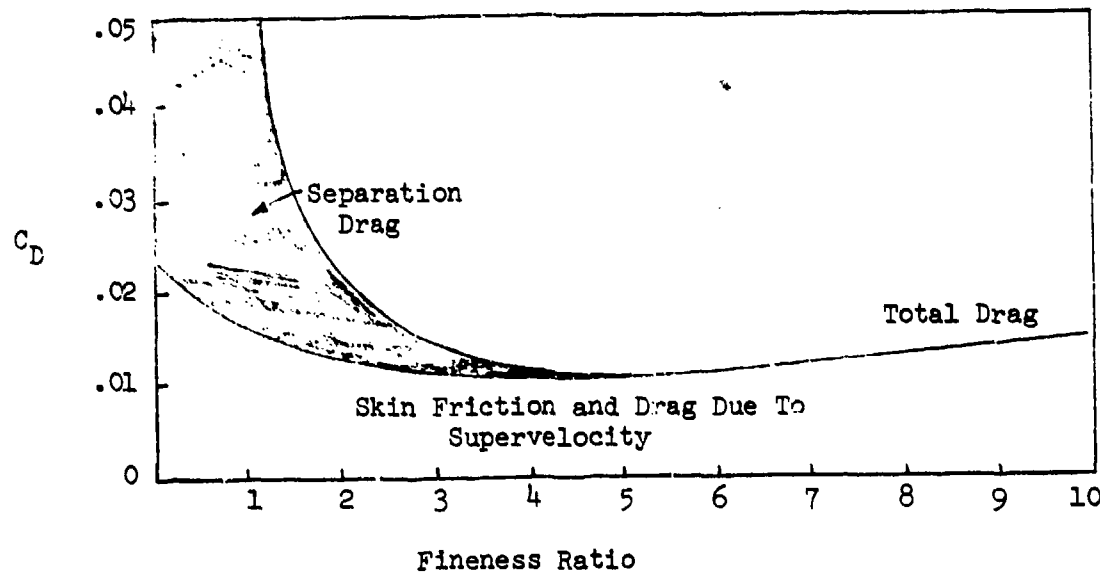


Figure 16. Drag Coefficient on a Body of Revolution as a Function of Fineness Ratio as Calculated by Hoerner's Formula.

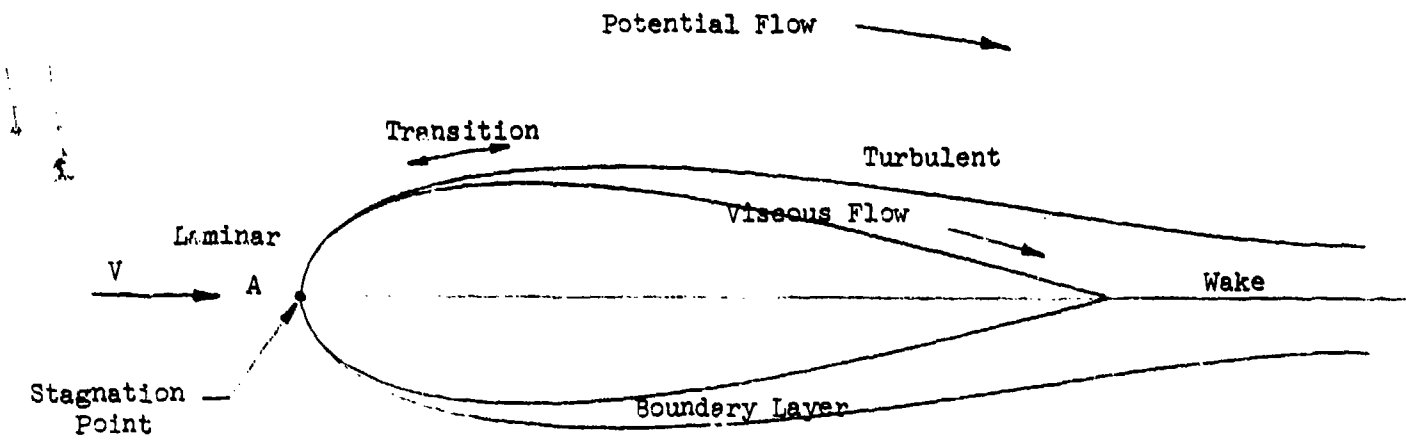


Figure 17. Flow Model For Zero-Lift Drag Prediction on Bcdy of Revolution.

## Bodies of Revolution

### 3.) Angular Damping

In addition to predicting the static forces and moments i.e., their dependence upon angle-of-attack and sideslip, it is important from a stability and control viewpoint to be able to predict the angular damping as well as the possible rate dependence of the forces.

Potential flow theory gives for the moments about the center of buoyancy no dependence upon angular rate or angle-of-attack rate as can be seen from the equations given in an earlier section. There are forces dependent upon these two variables however. Considering for purposes of discussion the vertical force

$$Z = -\lambda_{33} \dot{w} + \lambda_{11} qu - \lambda_{22} pv$$

Linearizing about steady flight at zero sideslip and a trim flight speed  $U_0$

$$Z = -\lambda_{33} U_0 \dot{\alpha} + \lambda_{11} U_0 q$$

This force will give rise to damping moments if the center of gravity or reference point is located some distance  $\Delta x$  ahead of the center of buoyancy.

The moment about the new reference point will be

$$M_{\Delta x} = \lambda_{33} U_0 \Delta x q - \lambda_{33} U_0 \Delta x \dot{\alpha}$$

Equal and opposite values of pitch damping and the angle-of-attack rate moment are produced, i.e.,

$$M_q = \lambda_{33} U_0 \Delta x$$

$$M_{\dot{\alpha}} = -\lambda_{33} U_0 \Delta x$$

that is if the vehicle is pitching and not allowed to heave, then these two effects will cancel and there will be no damping. Comparison of this result with other theories is shown in the previous section. Miles<sup>35</sup> gives results

which are equal to the above results in the case of the slender body where only the limiting value of  $\lambda_{33}$  is employed. That is  $\lambda_{33} \rightarrow \rho V$  as the fineness ratio becomes very large. Care must be taken in using Miles' results owing to the variables used which are characteristic of flutter analysis. At least one paper on the damping in pitch<sup>36</sup> has not made the transfer of variables properly and consequently gives an incorrect result.

There is considerable experimental data on the damping of bare hulls measured by a variety of techniques<sup>37 - 40</sup>. The techniques employed in the experiments involves free oscillations, whirling arm tests and curved model tests. Note that the free oscillation tests measure a damping which is in fact  $(M_q + M_d)$  while the other two techniques measure  $M_q$  directly. The whirling arm experiments are quite difficult to interpret requiring many corrections before the data can be used. The theory of curved models is described in great detail in Reference 39. Further curved model results are presented in Reference 40.

Typical experimental numbers for the damping of bare hulls are

$$C_{M_q} = - .039 \text{ (Ref. 41, oscillation test)}$$

$$C_{M_q} = - .023 \text{ (Ref. 42, oscillation test)}$$

$$C_{M_q} = - .030 \text{ (Ref. 43, oscillation test, Shenandoah)}$$

From curved model test reported in Reference 39.

$$C_{M_q} = - .0335$$

where the dimensional derivative is given by

$$\frac{\partial M}{\partial q} = \frac{1}{4} \rho \frac{U_0^2 l^2 C_M}{q^{2/3}}$$

While Reference 40 also gives curved model results, no data are presented for a bare hull. Reference 40 does however, show good agreement between curved model tests and free oscillation tests indicating that  $\frac{\partial M}{\partial \alpha}$  is very small and probably negligible.

Now the question arises as to the significance of these results since we are comparing a finite value given by experiment to the theory which yields zero. We can obtain some idea of the significance of these damping values by considering the order of magnitude of damping which is provided for the idealized pitching or yawing motion of an airship. For single degree-of-freedom pitching motion the equation of motion of the airship would be

$$(I + I') \ddot{\theta} - \left( \frac{\partial M}{\partial q} \right) \dot{\theta} - \frac{\partial M}{\partial \alpha} \theta = 0$$

where  $\frac{\partial M}{\partial \alpha}$  has been neglected. Using the theoretical potential flow value for the pitching moment variation with angle-of-attack since our object here is to obtain an order of magnitude result

$$\frac{\partial M}{\partial \alpha} \approx \rho U^2 l$$

Further assuming that the moment of inertia of the vehicle is equal to the apparent moment of inertia arising from the dependence of the aerodynamic moment on angular acceleration

$$I + I' \approx 2 \left( \frac{\rho}{20} \pi l^2 \right)$$

The equation of motion becomes

$$\frac{\rho + \ell^2 \ddot{\theta}}{4} - \frac{\rho + 2/3 L^2 U_0}{4} C_{Mq} \dot{\theta} - \rho U_0^2 \dot{\theta} = 0$$

Non dimensionalizing the time scale by  $\frac{L}{U_0}$ , and dividing through by the coefficient of the second derivative term, the equation of motion becomes

$$\theta'' - \frac{5}{2} \frac{\ell}{\sqrt[3]{3}} C_{Mq} \theta' - 10 \theta = 0$$

Now

$$\frac{\ell}{\sqrt[3]{3}} = \left(\frac{3}{\pi}\right)^{1/3} (FR)^{2/3} = 1.365 (FR)^{2/3}$$

For a fineness ratio of five the equation becomes approximately

$$\theta'' - 10 C_{Mq} \theta' - 10 \theta = 0$$

For a typical value of  $C_{Mq}$  the value - .03 is taken. Thus the equation of motion is

$$\theta'' + .3 \theta' - 10 \theta = 0$$

It can be seen that this value of damping will have almost no influence on the divergence produced by the unstable angle-of-attack gradient.

The bare hull damping is thus quite small and probably the experimental values given above which are very similar for a number of different hulls are quite satisfactory for estimates of the bare hull damping as there does not appear from those results to be a strong dependence of this term on hull shape.

## AERODYNAMIC CHARACTERISTICS OF DELTA-SHAPED PLANFORMS

### INTRODUCTION

The aerodynamic characteristics of low-aspect ratio delta-shaped bodies in the low angle-of-attack flight regime are adequately predicted, with some notable exceptions, by at least one of several lifting line theories. At higher angles-of-attack and at aspect ratios less than approximately unity, empirical corrections are necessary to account for experimentally-observed non-linearities. Such empirical corrections, experimentally-determined and corroborated, are available to account adequately for the non-linear character of the aerodynamics in symmetrical flow.

Exceptions to the predictive accuracy of the lifting line theories occur primarily in the lateral-directional derivatives, particularly  $C_{N_B}$ . It should be pointed out, however, that little experimental data exist to qualify the theoretical predictions of many of the important rate derivatives such as  $C_{\ell_p}$ ,  $C_{\ell_r}$ ,  $C_{M_q}$ ,  $C_{n_p}$  and  $C_{n_r}$  and the theoretical predictive ability in most cases can only be inferred.

In general, there is no adequate treatment of non-linearities in the lateral-directional derivatives at large amplitudes of sideslip comparable to the empirical representation of the longitudinal case. Therefore, discussion of the lateral-directional characteristics herein will be confined to small-perturbation representations linearized about zero steady-state sideslip and angular rates.

### Lifting Line Theories

The lifting line theories considered here are all based upon 2-dimensional approximations of the 3-dimensional lifting surface integral

equation. Historically and logically the approaches follow the work of Munk (Ref. 1) in his slender body theory in which for slender bodies the flow is considered 2-dimensional in a chordwise sense analogous to the manner in which in Prandtl's (Ref. 6) lifting line theory for high aspect ratios the flow is considered 2-dimensional in a span-wise sense. As a consequence of the chordwise 2-dimensionality, that is 2-dimensionality in the direction of motion of the vehicle, each portion of the body sees the flow as being undisturbed by the presence of the remainder of the body. To an observer stationary with respect to the fluid the resulting flow picture on a spanwise strip across the body is that of the potential flow around a flat plate, of width equal to the body local span, being started in motion in a fluid initially at rest. A representation of such a potential flow is shown in Figure 18. The results of such an approach as applied to slender bodies of revolution are discussed in the section on Bodies of Revolution.

Following Munk's reasoning with regard to the chordwise (hence streamwise) 2-dimensionality of the flow, Jones (Ref. 14) developed a low aspect ratio lifting line theory applicable to delta shaped wings with straight trailing edges. The essential difference between Jones' low aspect ratio lifting line theory and subsequent theories, to be discussed, is that his 2-dimensional approximation to the 3-dimensional lifting surface integral assumes the lift to be constant along a ray emanating from the vertex of a delta wing while subsequent workers allow more general chordwise lift distributions. For a comprehensive discussion of the basic similarities and differences among the various

low aspect ratio lifting line theories, as well as discussion of their analogy to Prandtl's high aspect ratio lifting line theory, the reader is referred to Reference 44.

Although Jones' theory is somewhat over-simplified to serve as the exclusive representation of delta-wing aerodynamics, it is used as the basis of potential flow representation of the stability derivatives of delta-shaped bodies (Ref. 5 and 45) some of the results of which are presented in Table I. Additionally, it contains the important descriptive characteristics of the flow about such bodies in a clear and understandable manner and thus warrants further discussion and continued comparison with the more exact representations.

The 2-dimensional potential distribution resulting from the delta-planform flow pictured by Jones is as shown in Figure 18 and has an elliptical spanwise distribution given by the expression

$$\phi = V \alpha \sqrt{y_1^2 - y^2} \quad (1)$$

According to potential theory, the local pressure difference across the surface,  $\Delta p$ , is given by the local rate of increase of potential. That is,

$$\frac{\Delta p}{2\rho} = \frac{\partial \phi}{\partial t} . \quad (2)$$

Since for a delta-planform the local span,  $y_1$ , is a linear function of the chordwise coordinate,  $x$ , and in the frame of reference fixed with the fluid  $x$ , and hence  $y_1$ , increases linearly with time, the indicated differentiation gives in terms of a local pressure coefficient,

$$\frac{\Delta p}{q} = 4 \alpha \frac{y_1}{\sqrt{y_1^2 - y^2}} \tan(90 - \Lambda_{l.e.}). \quad (3)$$

This expression is plotted in Figure 19 and shows hyperbolic local spanwise pressure distribution at any chordwise station,  $x$ , with a resulting infinite pressure peak along the leading edge.

Although, as shown, the local spanwise pressure distribution is hyperbolic, when this distribution is integrated in a chordwise direction to determine the lift distribution, it is seen that the total spanwise lift distribution is elliptical;

$$\frac{\partial L}{\partial y} = \int_0^C \Delta p \, dx = q \frac{\alpha}{4} \sqrt{\left(\frac{b}{2}\right)^2 - y^2}. \quad (4)$$

Figure 19 illustrates this sometimes confusing result of a hyperbolic spanwise local pressure distribution integrating to give an elliptical spanwise lift distribution and points out the importance of distinguishing between the local spanwise loading and the average spanwise loading. Further, equations (1) and (2) indicate that the local spanwise loading is independent of planform shape although planforms other than delta will not possess an elliptical average spanwise lift distribution and hence will not exhibit a constant downwash and minimum induced drag.

The resulting elliptical lift distribution demonstrated by Jones' theory gives rise to the important conclusion that the induced downwash at the lift surface will be uniform and have its minimum value

$$\epsilon = \frac{C_L}{\pi AR} \quad (5)$$

and correspondingly the induced drag will be a minimum and given by

$$C_{D_1} = \frac{C_L^2}{\pi AR} . \quad (6)$$

An interesting corollary to the elliptical lift distribution result on a delta-shaped planform is that when the spanwise distribution is integrated across the maximum span, the lift is proportional to (maximum span)<sup>2</sup> and not surface area;

$$\int \frac{\partial L}{\partial y} dy = L = q \frac{\pi}{2} \alpha b^2 . \quad (7)$$

Substituting the definition of  $AR = 2 \frac{b}{c}$ , for a delta, gives the familiar slender wing result

$$C_{L_\alpha} = \frac{\pi AR}{2} . \quad (8)$$

The further developments of lifting-line theories by Weissenger (Ref. 46) Lawrence (Refs. 44 and 47), although not restricted to low aspect ratios, contain the essential representation of the aerodynamics of low aspect ratio delta-shaped lifting surfaces to be used for predicting the aerodynamic characteristics at low angles-of-attack and sideslip. The two approaches differ only in that Weissenger assumes a non-constant chordwise distribution of lift and proceeds to calculate the spanwise distribution from the 2-dimensionalized lifting surface integral whereas Lawrence assumes a spanwise distribution, as given by Jones, and calculates the chordwise distribution. Both theories give virtually the same result on the average and it is only if one particularly desires detailed spanwise or chordwise lift distribution that a choice between the theories is clearly indicated.

Additionally, in Reference 48 are presented expressions which represent with good accuracy the results of a complete lifting surface theory approach

to the low angle-of-attack delta wing aerodynamics. Although these expressions are strictly curve-fitting mathematical representations and thus contain no physical explanation of the aerodynamic phenomena, they are in good agreement both with the lifting surface theory results to which they were fit and with the results of Lawrence and Weissenger. Their inclusion here is intended as an aid in estimation and calculation rather than as an assistance in understanding the phenomena.

#### Prediction of Aerodynamic Coefficients

Discussion of techniques to predict the aerodynamic coefficients of delta-shaped low-aspect-ratio bodies will be divided into consideration of longitudinal and lateral/directional characteristics. The longitudinal case, including the lift, drag and pitching moment coefficients, will be further divided into low and high angle-of-attack regimes.

#### Longitudinal Characteristics: Lift and Pitching Moment

The lifting line theories of Lawrence and Weissenger may be used to predict the lift and pitching moment coefficients on delta-shaped planforms across the low-angle-of-attack range for which the lift curve slope is linear. The accuracy with which these coefficients are predicted is shown in Figures 20 and 21 in which are presented the theoretical lift curve slopes and aerodynamic center locations for delta-shaped planforms as functions of aspect ratio and compared to experiment. Also shown in Figures 20 and 21 are the predictions of Jones' lifting line theory as well as the lifting-surface theory curve-fitting expressions from Reference 48.

It should be noted that, although both the Lawrence and Weissenger theories, as well as the lifting surface theory curve fit, all give good

predictions of experimental lift curve slopes, only the Lawrence theory and lifting surface theories have adequately-detailed representations of chordwise lift distribution to predict accurately the aerodynamic center location.

The experimental data presented in Figures 20 and 21 are taken from References 48 and 49 and are for delta-shaped bodies with well-rounded leading edges. This distinction is important not only from the standpoint of our present interest in delta shapes as applied to buoyant assisted lift vehicles wherein rounded leading edges are to be expected. It is also important from the standpoint of the applicability of lifting line theories, the range of angle-of-attack over which the lift curve slope is linear and the theories are applicable, as well as the behavior of the lift and pitching moment coefficients at large angles-of-attack. In Figure 22 are presented experimental data taken from Reference 44 comparing the lift coefficient of sharp and round leading-edge delta shaped planforms, indicating significant differences in their lift characteristics, particularly at higher angles-of-attack.

The range of angle-of-attack over which the linear portion of the lift curve extends and where the lifting line theories are applicable is studied in Reference 48. Data from experiments of this reference are presented in Figure 23 showing lift coefficient as a function of angle-of-attack and Pitch Moment Coefficient vs. Lift Coefficient all for round-leading edge delta planforms of various aspect ratios. Also shown in Figure 23 are the lifting surface theory curve-fit approximations derived in Reference 48. Note that the experimental data are from cambered bodies and that the lifting surface theory gives adequate

predictions of both the angle of zero lift and the zero-lift pitching moment coefficient. A technique is developed in Reference 48 which relates the extent of the linear portion of the lift curve to the 2-dimensional pressure distribution on the airfoil section from which the delta planform body is generated. An example of this technique as well as a step-by-step procedure for its application is presented in References 48 and 50. The work of Reference 48 further concludes that there is an aspect ratio for round leading-edge delta planforms above which the lift curve slope is linear and constant for all angles-of-attack (presumably up to stall) and where the lifting surface and lifting line theories could be expected to apply throughout the practical range of angles-of-attack. This aspect ratio is given by the expression

$$AR = 1.71 \left\{ \sin \left[ \frac{1}{2\sqrt{1 + (\frac{2}{AR})^2}} \right] \right\}^{\frac{1}{4}} \quad (9)$$

and when evaluated for a delta planform gives a value of  $AR = 1.21$  as that aspect ratio above which the lift curve slope is entirely linear and constant.

The treatment of non-linearities in the lift curve given in Reference 48 represents a distinct departure from previous work in the field, notably that of Reference 44 and 51. The earlier work followed the lines of Allen (Ref. 18) and postulated a cross-flow drag force, as discussed in the section of Bodies of Revolution, to account for the non-linearities in lift curve slope observed on delta planforms with sharp leading edges as shown in Figure 22. As recognized in Reference 48, this approach did not

predict adequately the lift characteristics of round-leading-edge delta planforms. By means of combined force and moment measurement and flow visualization experiments it was determined in Reference 48 that a more proper representation of round-leading-edge delta planforms was as shown schematically in Figure 24, taken from Reference 48, wherein the lift curve is composed of one or more distinct linear slopes each of which is associated with a distinct observed upper surface flow pattern. The details of application of this lift curve representation are presented in References 48 and 50, and the experimental data employed to develop the representation are presented in Figure 23.

A similar approach to the prediction of the non-linear (or non-constantly linear) regime of pitching moment coefficient is developed in Reference 48 and the application procedure is detailed in References 48 and 50; the pertinent experimental data are presented in Figure 23.

#### Longitudinal Characteristics: Drag Coefficient

Discussion of techniques for predicting the drag coefficient will be divided according to the principal physical contributions to drag coefficient, profile and induced drag. Discussion of induced drag contributions will be further divided into considerations of induced drag in the angle-of-attack region where the lift curve slope is linear and predicted by lifting-line theories and the higher angle-of-attack region where non-linear effects are important.

#### Profile Drag

Prediction of drag at zero-angle-of-attack for bodies of revolution

has been discussed extensively in Reference 52 and elsewhere in this report.

By far the most important contribution in these bodies, in the range of fineness ratios of interest, is the skin friction drag. This also holds true in the case of delta-shaped planforms, however, the empirical formulation required to account for shape effects on skin friction drag must be modified to accommodate the 3-dimensional non-axisymmetric shapes. Such an empirical representation has been developed in Reference 23 which accounts approximately for form (pressure) drag as well as skin friction drag:

$$C_{D_p} = 2 C_F [1 + 2 (\frac{t}{c}) + 60 (\frac{t}{c})^4] \quad (10)$$

where  $C_F$  is the turbulent flat plate skin friction coefficient. A further refinement to 10 is developed in Reference 48 in an effort to control better for camber and position of maximum thickness effects:

$$C_{D_p} = C_F [\frac{A_w}{S_w} + 2 G (\frac{t}{c}) + 120 (\frac{t}{c})^4] \quad (11)$$

where  $G = 0.8 (1 + 5 x_t^2) (1 + 6000 x_c y_c^2)$ . (12)

It should be noted that for the case of no camber,  $A_w/S_w = 2$  and for maximum thickness position  $x_t \approx 0.32$ , expression (11) reduces to

$$C_{D_p} = 2 C_F [1 + 1.2 (\frac{t}{c}) + 60 (\frac{t}{c})^4] \quad (13)$$

which is the expression suggested in Reference 23 for sections with maximum thickness aft of approximately 0.3c. Expression (11) is recommended here as being the most complete representation of shape effects on skin friction drag.

The turbulent flat plate friction coefficient  $C_F$  is adequately represented in the Reynolds number range of interest ( $10^7 - 10^8$ ) by either of two formulations due to Schoenherr (Ref. 23) and Prandtl-Schlichting (Ref. 53). Although Hoerner recommends the Schoenherr expression

$$\frac{0.242}{C_F} = \log_{10} (R_N C_F), \quad (14)$$

the Prandtl-Schlichting expression

$$C_F = \frac{0.455}{(\log_{10} R_N)^{2.58}} \quad (15)$$

is recommended by the authors of Reference 9 and is the more easily employed. Both expressions are correlated in the high Reynolds number range with the same data (Kempf) in Reference 23 and 53, respectively,

A comparison of predicted and measured  $C_D$  is presented in Figure 25, taken from Reference 48, which shows the wind tunnel test measurements of  $C_D$  plotted against  $C_D$  as predicted by use of expressions (11) and (15), after suitably accounting for the effects of transition strip roughness used in the tests of Reference 48. The agreement indicated in Figure 25 is quite good, with a singular deviation being exhibited by the very thin (10%) configuration.

To obtain greater accuracy in the prediction of  $C_D$  than afforded by the technique demonstrated in Figure 25 would require a complex analysis analogous to that employed in Reference 27 for bodies of revolution. Such techniques are not available, however, for arbitrary 3-dimensional

non-axisymmetric shapes with a full-turbulent boundary layer and, in the absence of specific test data, accuracies approximating those demonstrated in Figure 25 must be accepted.

#### Induced Drag

The induced drag coefficient for delta-shaped planforms at low angles-of-attack is predicted by a parabolic drag polar represented by the expression

$$C_{D_i} = \frac{C_L^2}{\pi AR e} \quad (16)$$

This representation is commensurate with the minimum value of induced drag associated with constant downwash resulting from the elliptic span loading shown by the various lifting line theories. Inclusion of an "efficiency factor",  $e$ , is required to account for real fluid effects on the development of the leading edge suction required by imposition of the Kutta condition at the trailing edge. The correlation of  $e$  with leading edge radius Reynolds number developed in Reference 54 is presented here in Figure 26 taken from Reference 48. The relationship shown in Figure 26, in conjunction with the expression (16), is applicable to uncambered delta planforms with round leading edges as shown in Figure 27 which shows the experimental results of Reference 49 compared with the suggested representation for induced drag. Highly cambered shapes such as those tested in Reference 48, exhibit an unexplained deviation from the Rutherford-Frost representation of  $e$ . In Reference 48 it is suggested, but not confirmed, that the leading edge suction may have been influenced by the leading edge roughness used to promote transition on the wind tunnel test models; such roughness was not employed in the models of Reference 49. All of the correlations of test with theory for induced drag presented in

Reference 48 are in fact self-correlations wherein an effective  $\epsilon$  is determined from the data and then used to predict the data and are therefore possibly inapplicable to other data.

Induced drag in the range of angles-of-attack where the lift curve slope departs from the lifting surface theory prediction can be predicted by the methods of Reference 48. The accuracy of this prediction technique is demonstrated in Figure 28 and in Figure 27 where it is applied to the AR = 1 data from Reference 49. The approach consists basically of assuming that the non-linear lift (discussed previously) acts normal to a line joining the trailing edge of the airfoil section chord line to the section maximum upper surface ordinate as shown in Figure 29.

#### Lateral/Directional Characteristics: Directional Stability

The directional stability derivative,  $C_{N_B}$ , is predicted to be identically zero by the lifting line theories of Jones, Lawrence and Weissinger since all consider only planform and cross-flow (in the vertical plane) effects. Although, as previously mentioned, these theories require round leading edges and hence finite thickness to be applicable, they do not include thickness effects in their formulation.

Experimental data on delta-shaped planforms from References 49, 55 and 56 are presented in Figure 30 and show significant levels of de-stabilizing  $C_{N_B}$  on bare delta-shaped hulls. Physically it can be reasoned that thick delta-planform bodies, particularly at lower aspect ratios, in transverse flow closely resemble bodies of revolution at least in the nose portion. Thus, it might be expected that, at least in the forward portion of the

vehicle where the cross sectional area is increasing in the flow-wise direction the destabilizing leading edge nose negative pressure peak predicted by potential theory (Ref. 4) would exist. It is more difficult to conceive however, that the corresponding negative pressure peak on the opposite side of the after portion of the body also predicted by potential theory for bodies of revolution would exist. Some insight into the degree to which the potential flow picture is applicable can be obtained by considering the lateral center of pressure location. In Figure 31 are presented experimental data on the center of lateral pressure location obtained from the data of Reference 49 by dividing  $C_N$  by  $C_y$  and averaging over the range of yaw angles tested. In order for  $C_N$  to arise from the forward pressure peak only, the center of pressure would be very near the nose. Conversely, for the potential flow picture, with a corresponding windward-side negative pressure peak on the after section of the body, to be valid the center of pressure would be infinitely ahead of the nose. Examination of Figure 31 indicates that neither case is precisely true; at the lowest aspect ratios tested the center of pressure is in fact well ahead of the nose, indicating the existence of at least part of the aft pressure peak. At the higher aspect ratios, however, the center of pressure approaches the trailing edge, indicating that the potential flow representation, even at the leading edge, is seriously questionable. Based upon the meager data available it can only be stated that the slender body theory approach seems applicable at aspect ratios around unity; at higher aspect ratios it is highly questionable.

With regard to the magnitude of the  $C_{N_B}$  derivative it is of course arguable that the volume used in the slender body theory expression for  $C_{N_B}$  should be the volume of the actual body rather than that formed by revolving the center-line section. The comparison with experiment presented in Figure 30, however, indicates that the lesser volume formed by revolution of the center-line section gives better agreement with experimental data. In view of the rather crude justification for the application of slender body theory, the scarcity of corroborative experimental data, and the simplicity of the suggested approach it does not seem worthwhile to belabor the point. Suffice it to say that the suggested approach provides the sign and magnitude of the  $C_{N_B}$  derivative and although the thickness dependence implicit in the slender body expression is not confirmed by comparison with experiment it is also not refuted. The apparent aspect ratio dependence of the moment derivative coefficient indicated by the experimental data is in actuality a span independence of the dimensional moment derivative which, in non-dimensionalizing by the span and planform area, produces the trend with aspect ratio. This span independence is consistant with the slender body theory approximation suggested.

#### Lateral/Directional Characteristics: Dihedral Effect

In Reference 46 is presented an expression for dihedral effect for delta shaped planforms which provides an adequate representation of this derivative. In the notation of this report this expression is given as

$$C_{L_B} = \frac{C_L}{2} \left( 0.5 + \frac{1}{AR + \frac{1}{4}} \right) \sqrt{\frac{0.75}{\left(\frac{AR}{4}\right)^2 + (0.75)^2}} .$$

Comparison of this expression with the experimental data of Reference 49 and 19 as well as with Jones' theory as given by Nielsen and Ribner (Ref. 5 and 45) is presented in Figure 23. Although the experimental data do not appear to confirm the aspect ratio dependence stated by Weissenger, it seems clear that this representation is superior to that given by Jones' theory.

TABLE I

STABILITY DERIVATIVES OF LOW-ASPECT-RATIO TRIANGLE  
TO FIRST ORDER A,  $\alpha$ , AND  $\Gamma$

Stability derivatives	Principal axes (Origin at $\frac{2}{3}c$ from vertex)	Stability axes (Origin at distance $x_{cg}$ ahead of $\frac{2}{3}c$ )
$c_{L_0}$	$\frac{5}{2}A$	$\frac{5}{2}A$
$c_{L_{\alpha}}$	$\frac{5}{2}A$	$\frac{5}{2}A$
$c_{L_{\Gamma}}$	$\frac{5}{2}A$	$\frac{5}{2}A + \frac{x_{cg}}{6}$
$c_{m_0}$	0	$-\frac{\pi}{2} - \frac{x_{cg}}{6}$
$c_{m_{\alpha}}$	$-\frac{11}{16}A$	$-\frac{11}{16}A - \frac{x_{cg}}{2} - \frac{x_{cg}^2}{6}$
$c_{m_{\Gamma}}$	$-\frac{35}{16}A$	$-\frac{3}{16}A - \frac{x_{cg}}{2} - \frac{x_{cg}^2}{6}$
$c_{I_B}$	$-\frac{2}{3}\alpha - \frac{4}{6}\Gamma$	$\frac{2}{3}\alpha - \frac{4}{6}\Gamma$
$c_{I_p}$	$-\frac{1}{32}A$	$-\frac{1}{32}A + \left(\frac{5}{18} + \frac{8}{9}\frac{x_{cg}}{6}\right)\Gamma_a$
$c_{I_r}$	$\frac{40}{9}A + \frac{2}{9}\Gamma$	$\left(\frac{40}{9}A + \frac{\Gamma}{18}\right)\left(1 + \frac{x_{cg}}{6}\right) + \frac{\Gamma}{6}$
$c_{n_B}$	0	$\frac{4}{6}\Gamma_a$
$c_{n_p}$	$-\frac{40}{9}A + \frac{\Gamma}{18}$	$\left(-\frac{40}{9}A + \frac{\Gamma}{18}\right)\left(1 + \frac{x_{cg}}{6}\right)$
$c_{n_r}$	$-\left(\frac{1}{6} + \frac{4}{9A^2}\right)c_{D_0}$	$-\left(\frac{1}{6} + \frac{4}{9A^2}\right)c_{D_0} - \left(\frac{5}{18} + \frac{8}{9}\frac{x_{cg}}{6}\right)\Gamma_a$
$c_{T_B}$	0	0
$c_{T_p}$	$\frac{2}{3}\alpha - \frac{4}{3}\Gamma$	$\frac{2}{3}\alpha - \frac{4}{3}\Gamma$
$c_{T_r}$	0	$\frac{4}{3}\Gamma_a$

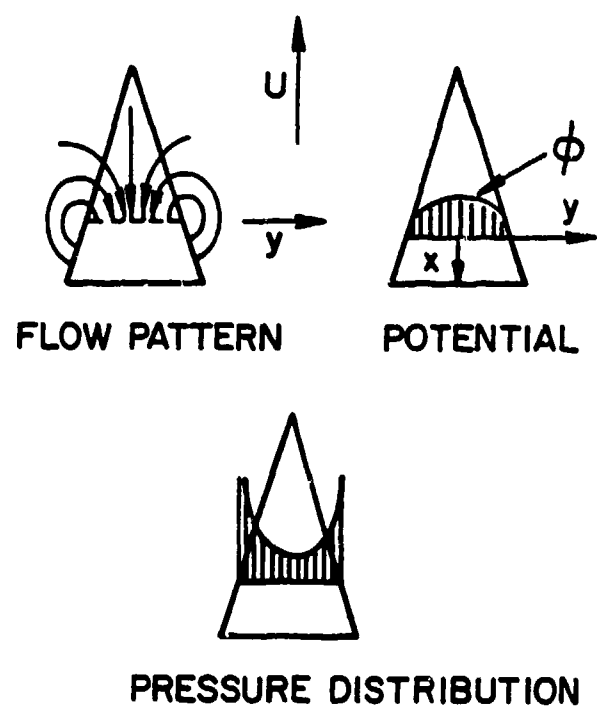


Figure 18. Potential Flow on Triangular Wings of Low Aspect Ratio.

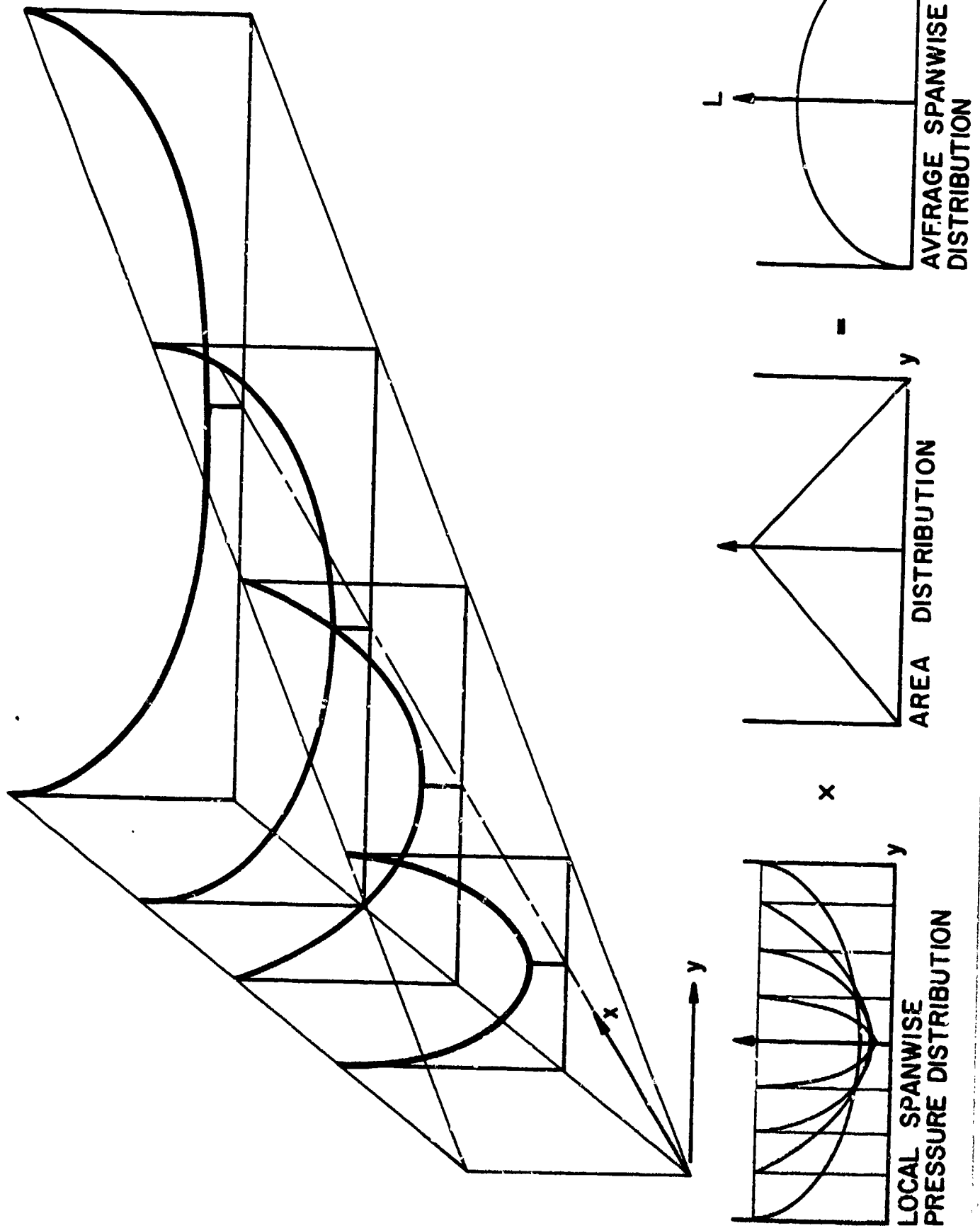


FIGURE 19. Pressure and Lift Distribution on Delta Wing,  
Jones' Theory

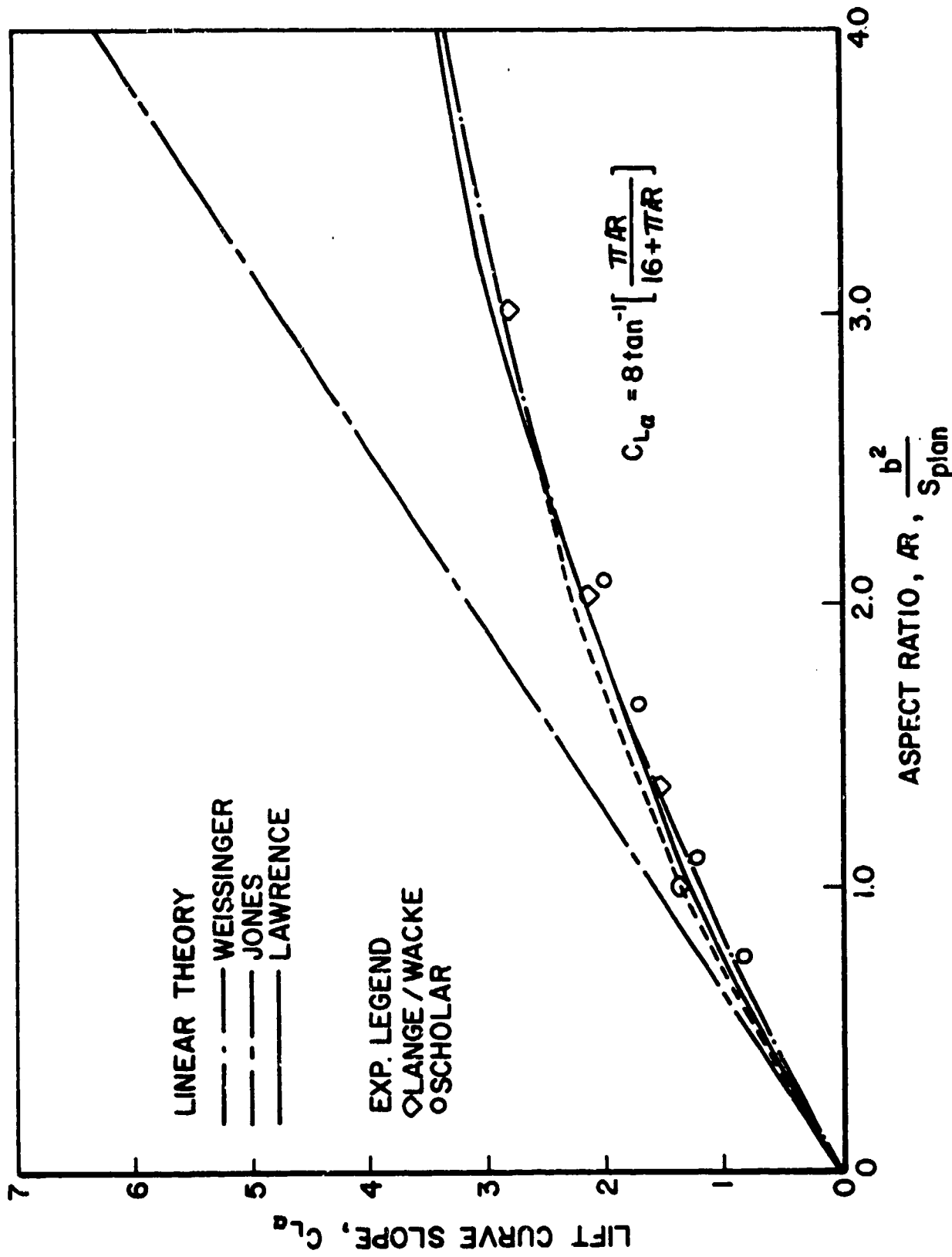


FIGURE 20. Lift Curve Slope vs. Aspect Ratio for Triangular Wings

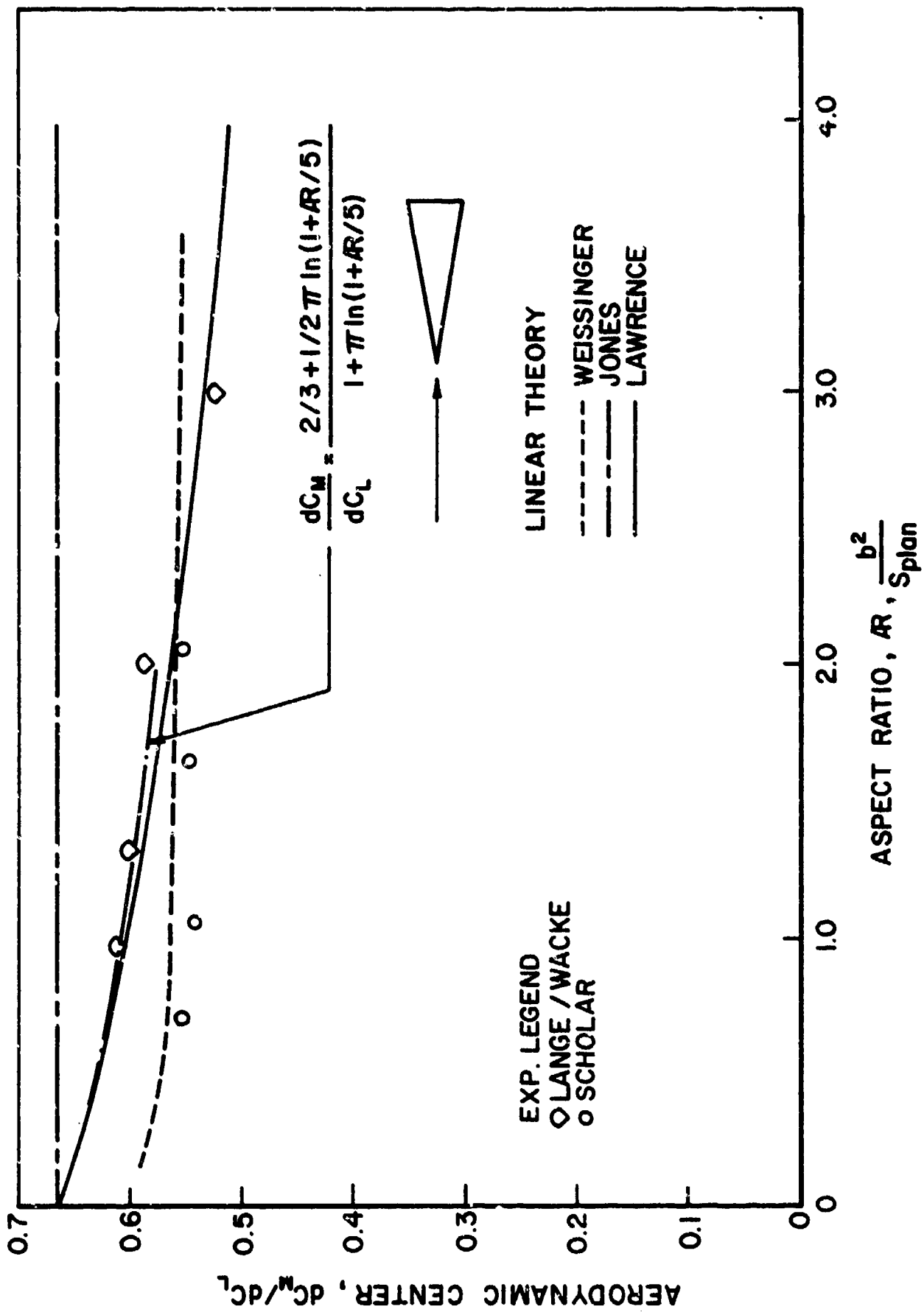


FIGURE 21. Center of Pressure vs. Aspect Ratio for Uncambered Delta Wings

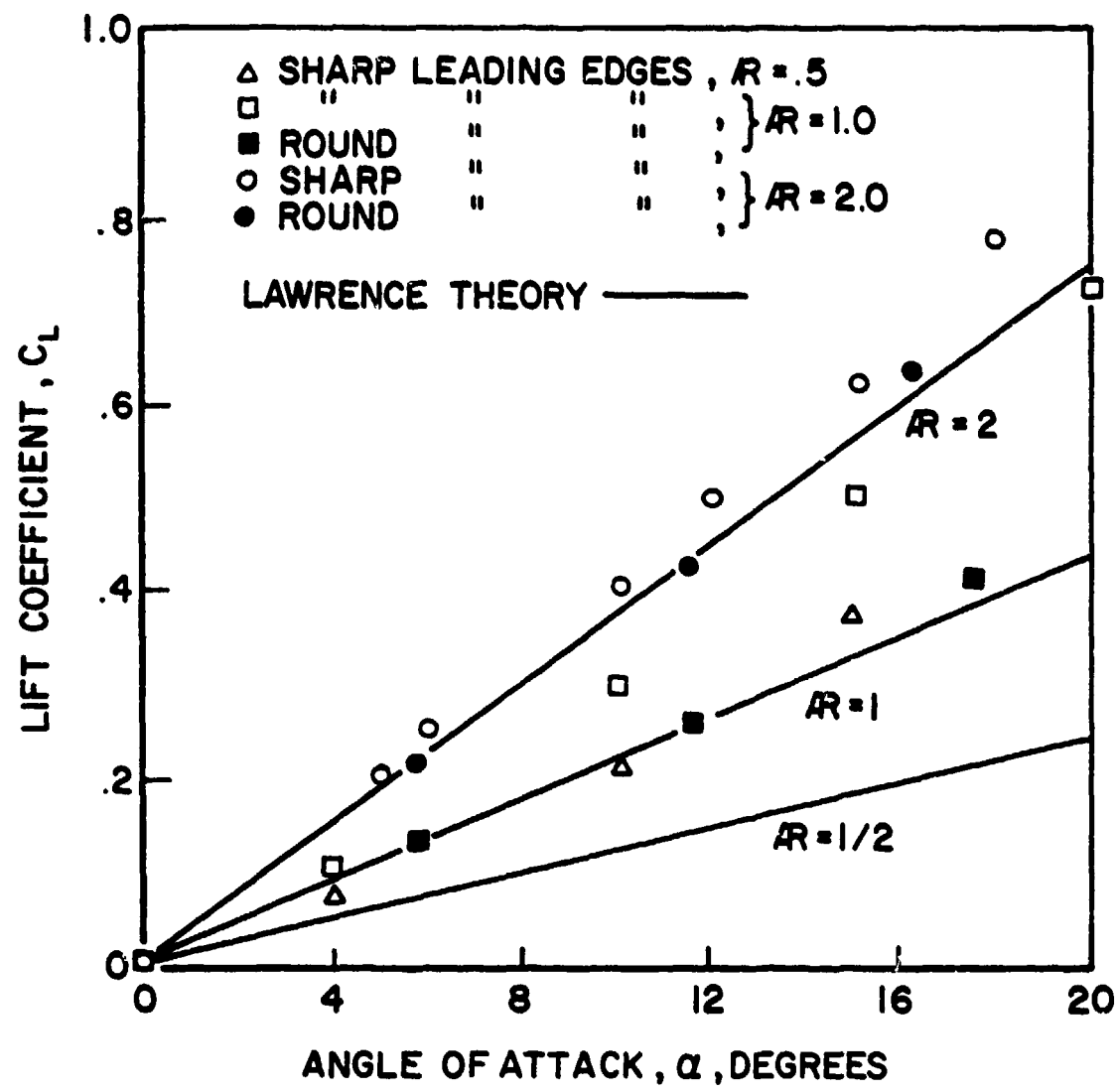


Figure 22. Lift Characteristics of Sharp and Round Leading Edge Delta Planforms.

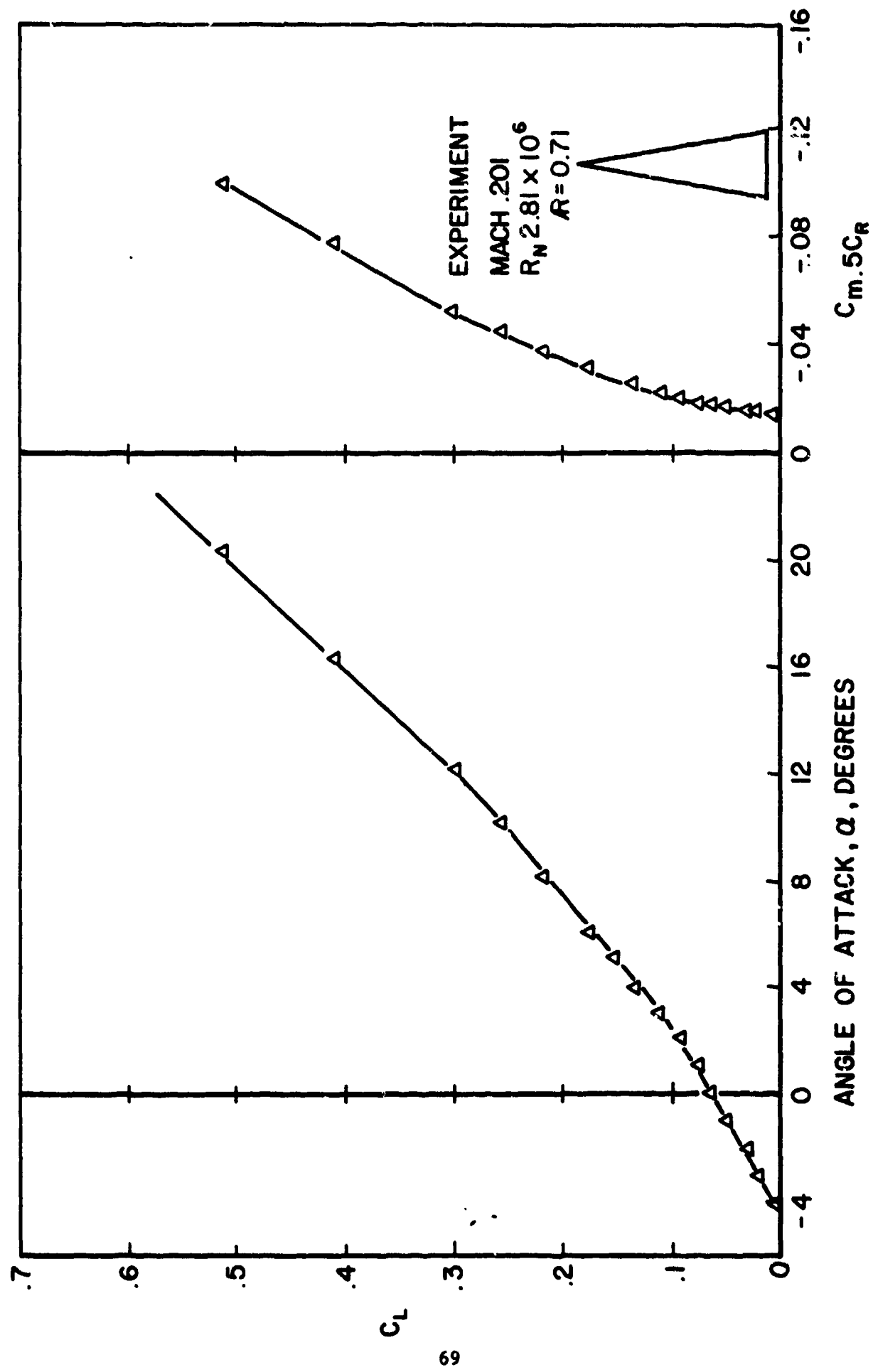


Figure 23. Comparison of Prediction Method and Experimental Lift and Moment Data.

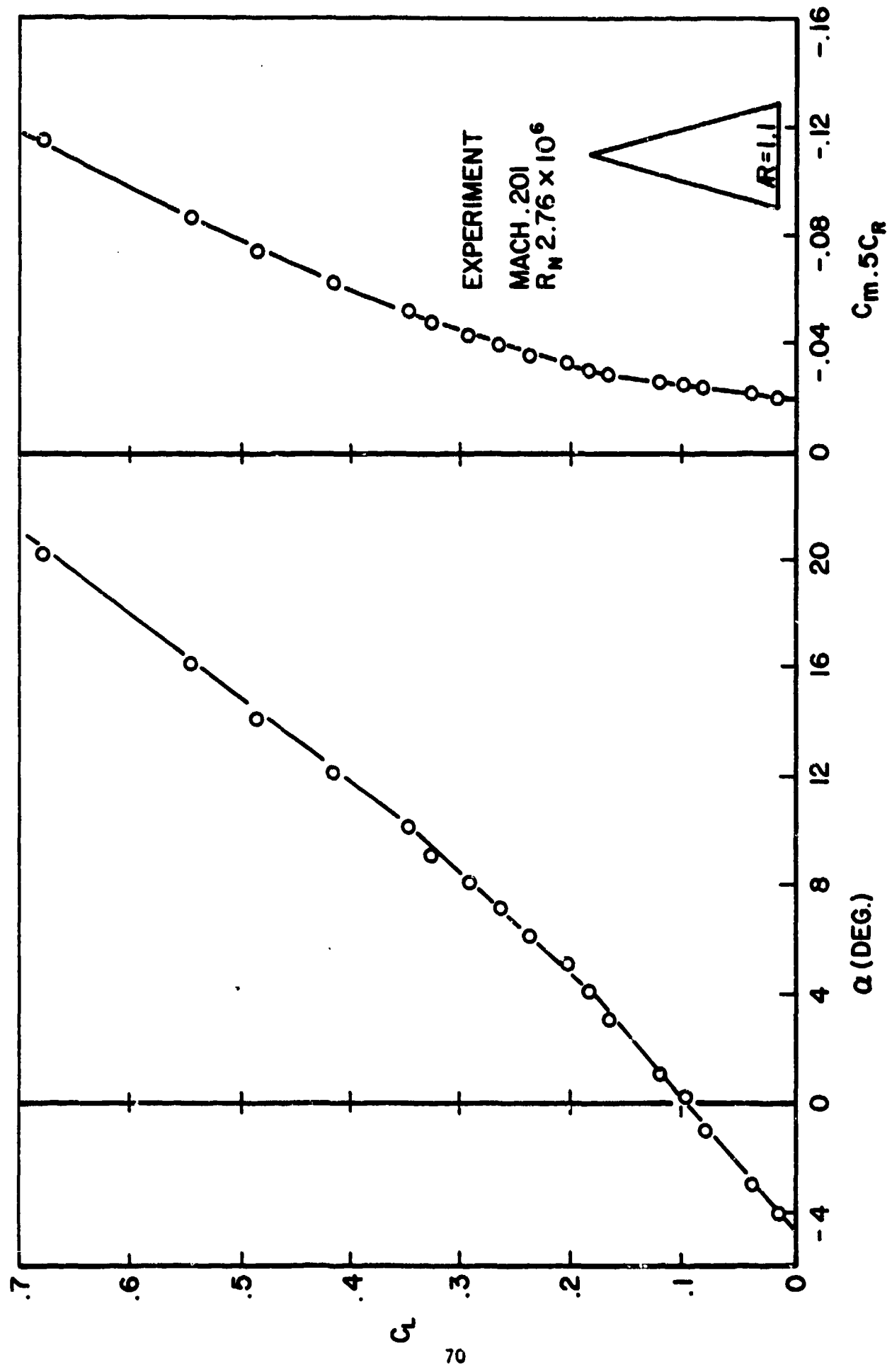


Figure 23. Continued.

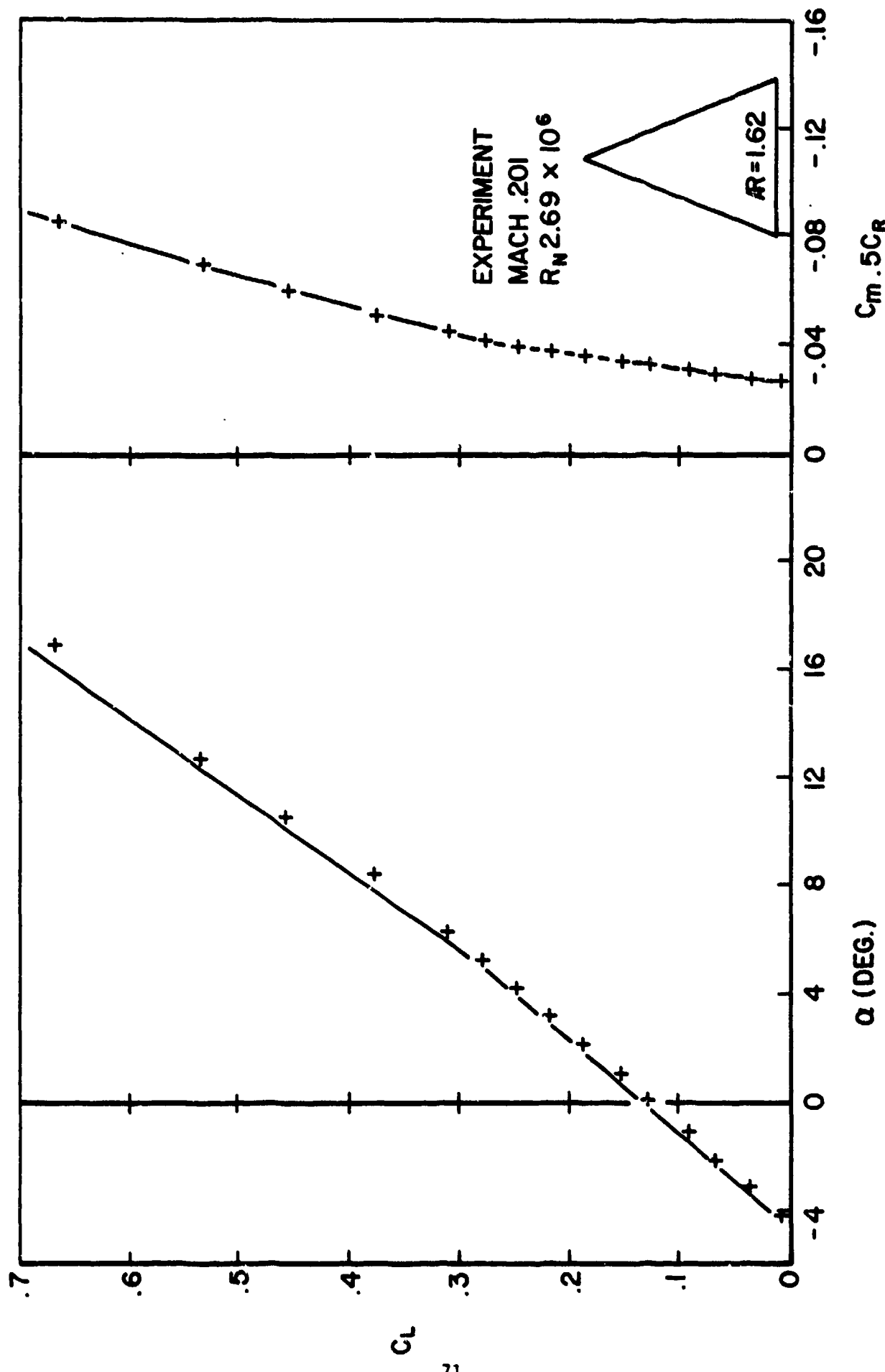


Figure 23. Continued.

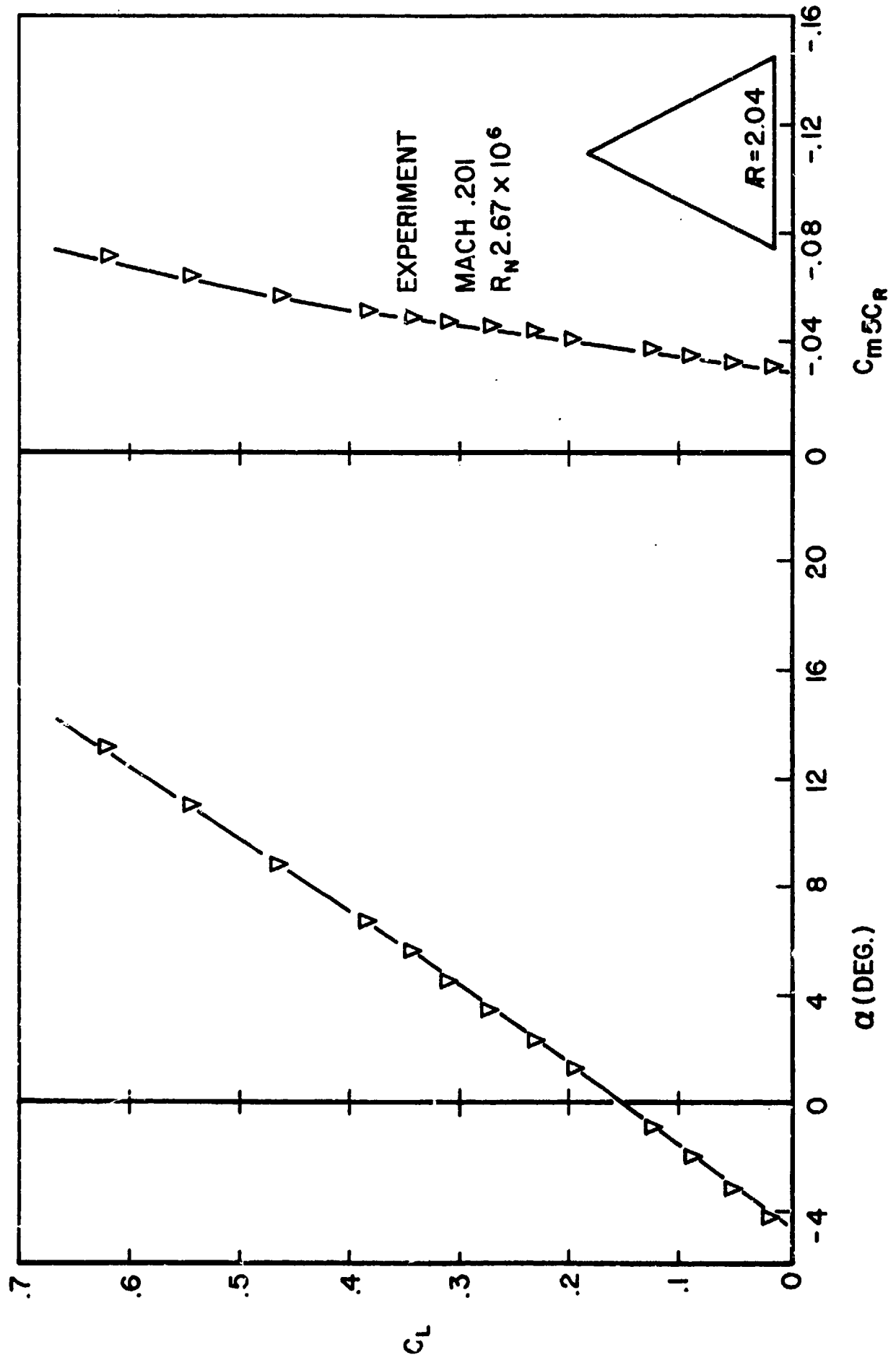


Figure 23. Continued.

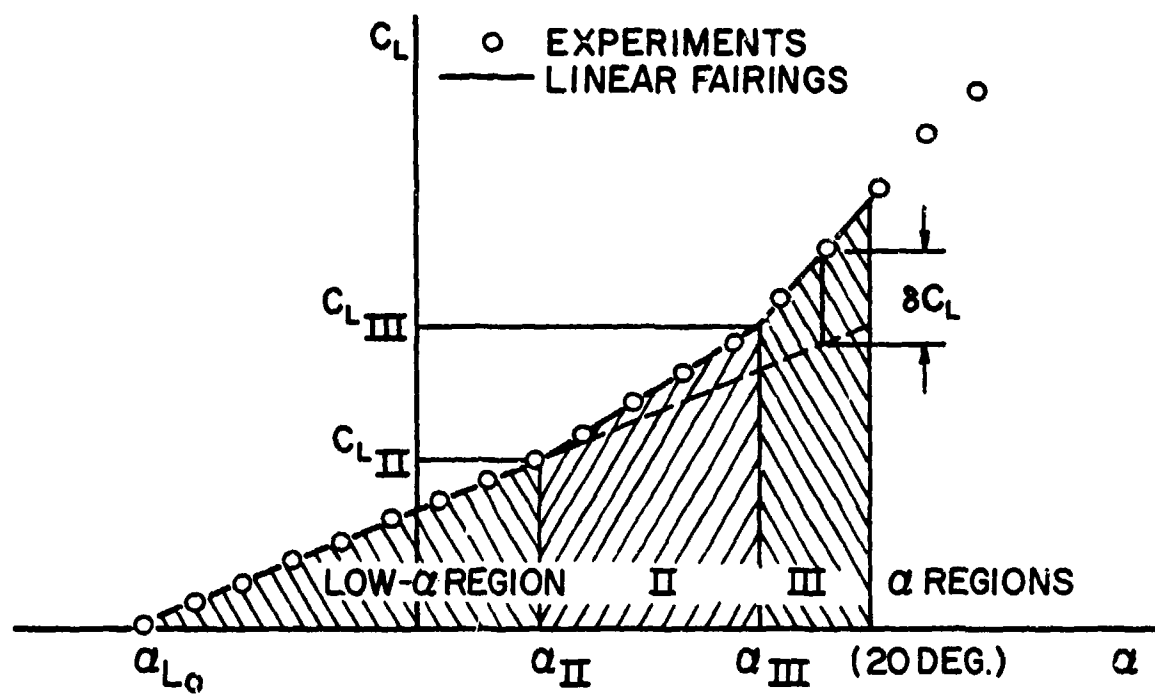


Figure 24. Definition of Lift Curve Regions.

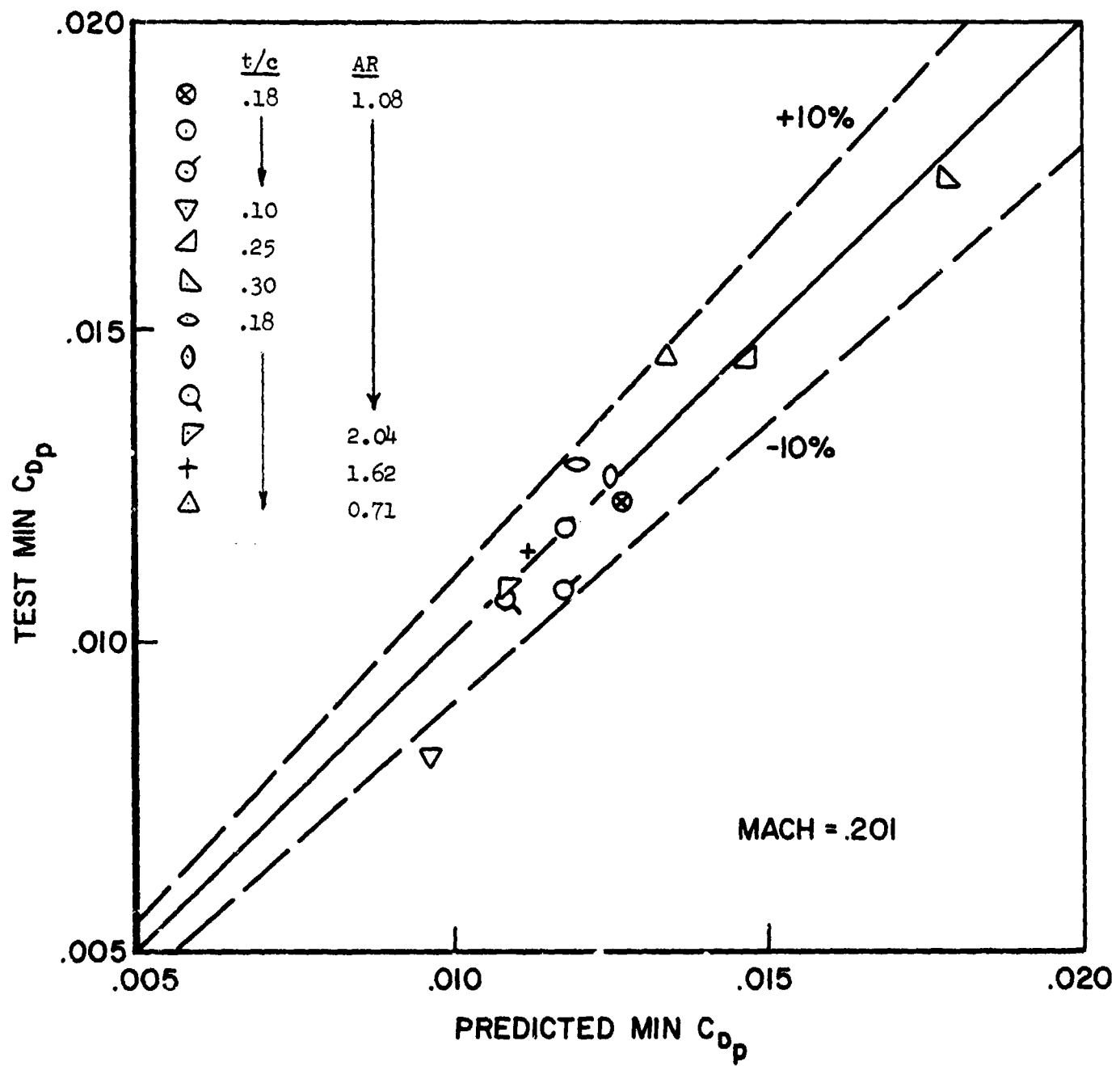
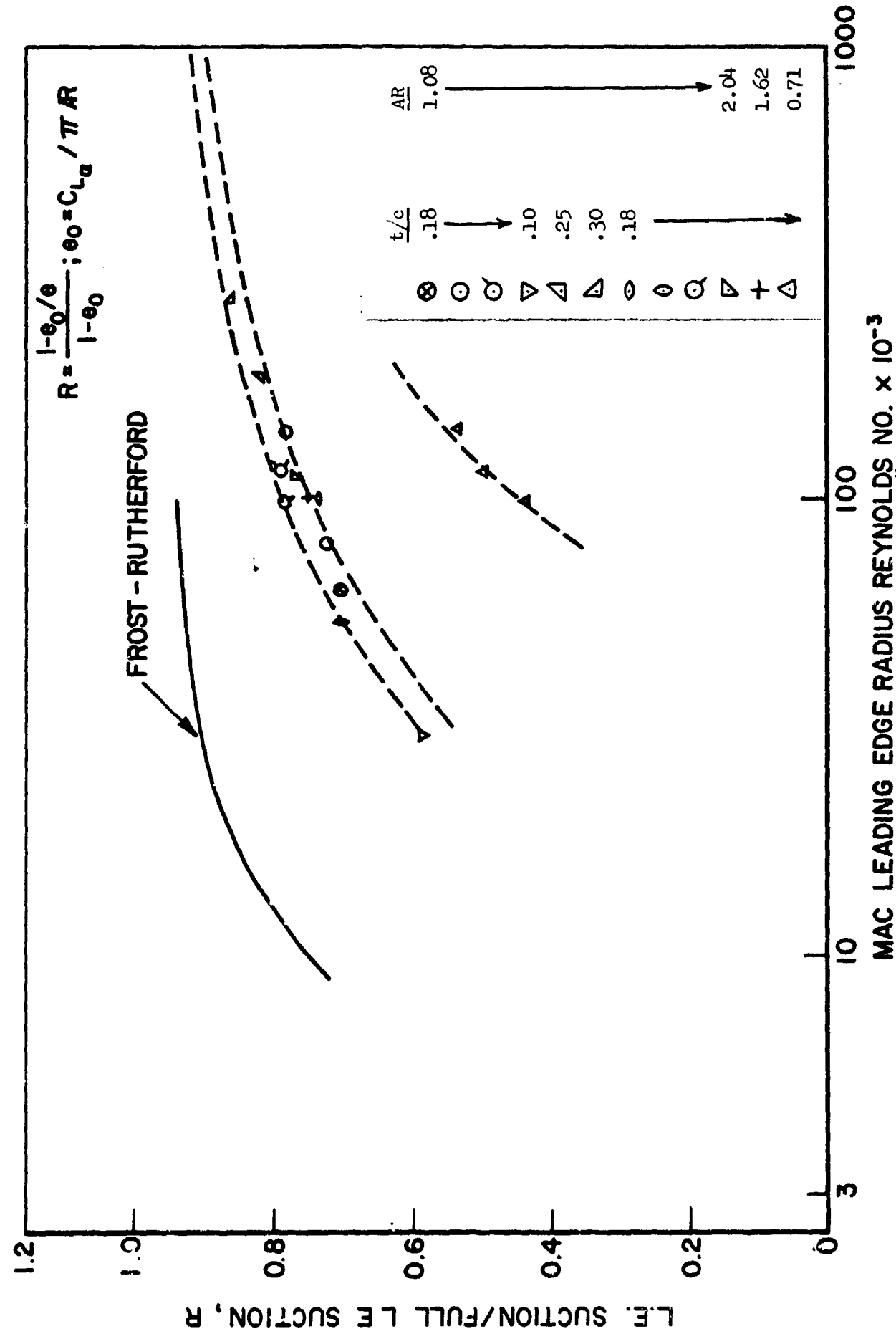


FIGURE 25. Comparison of Prediction Method and Experimental Data for Profile Drag



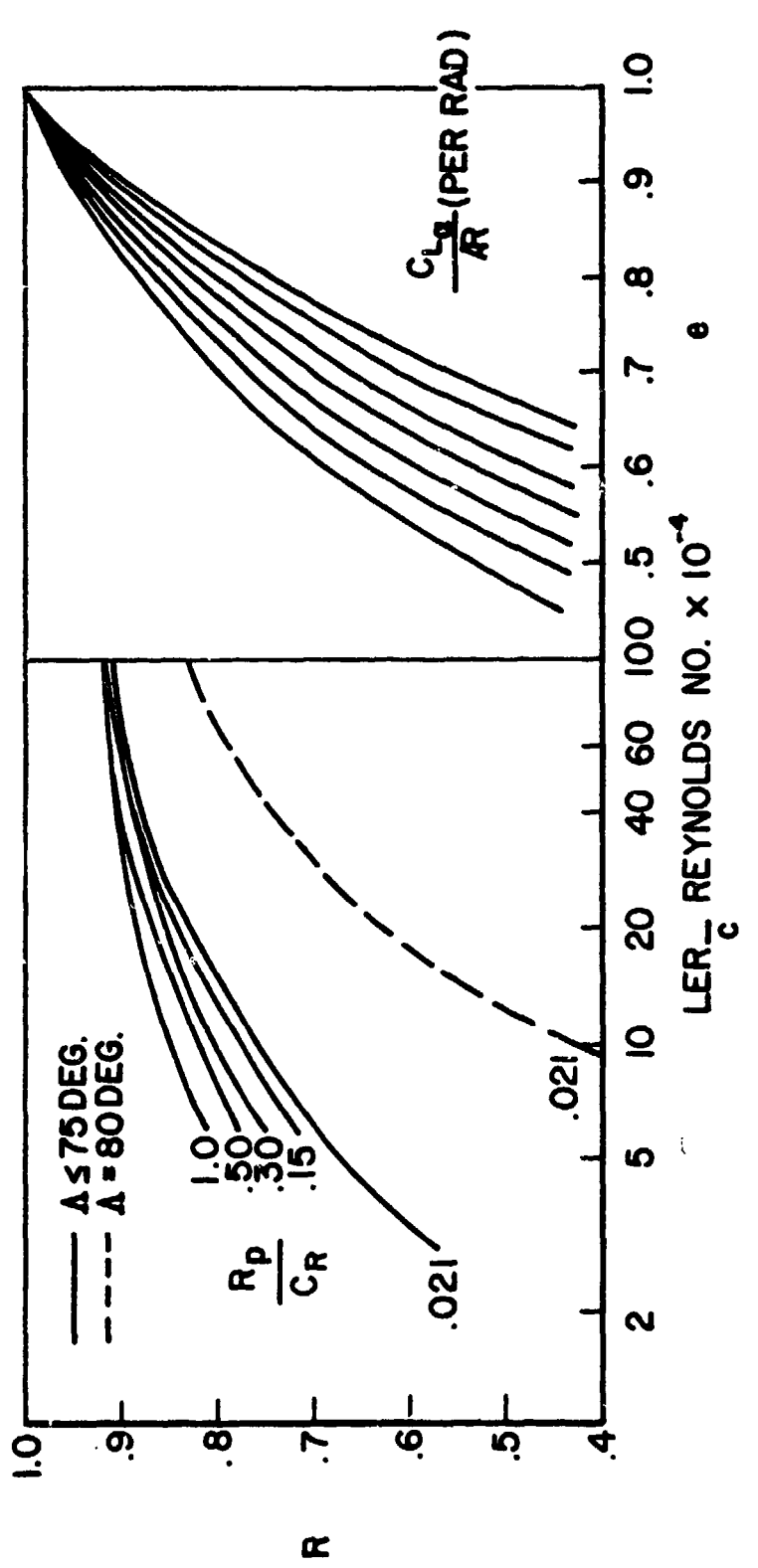


FIGURE 26. Determination of Efficiency Factor for Induced Drag  
(continued)

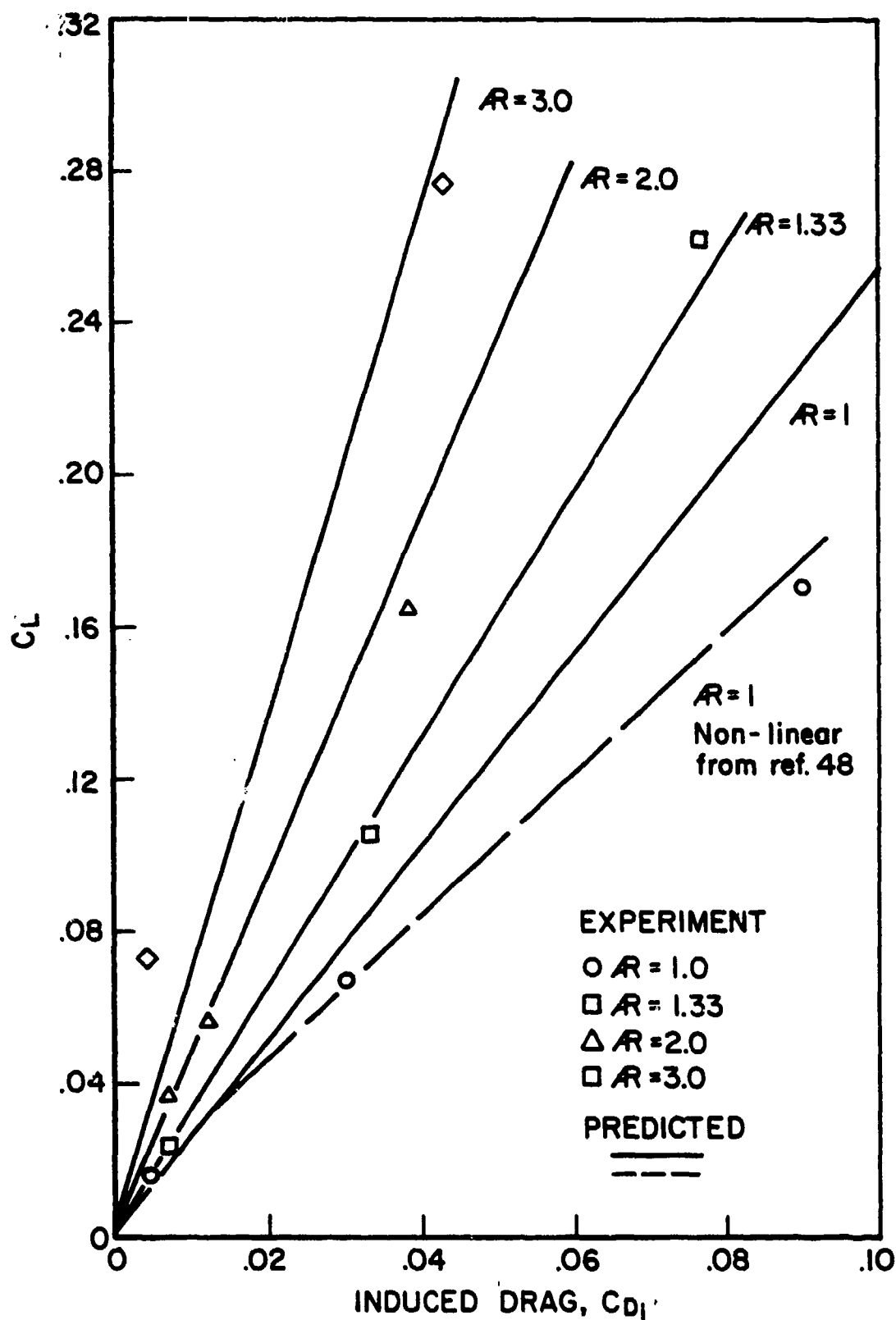


FIGURE 27. Comparison of Predicted and Measured Drag at Low Angles-of-Attack

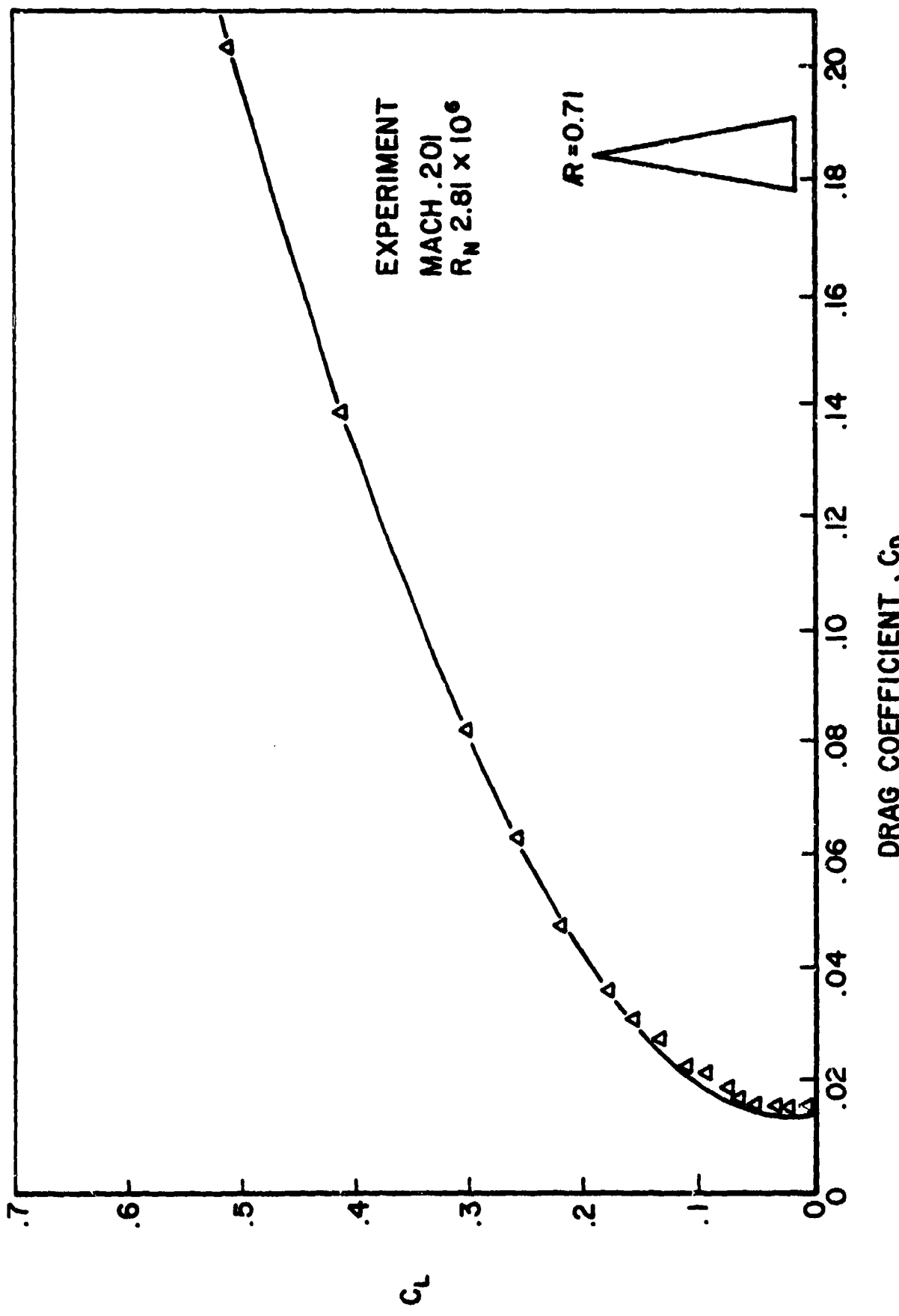


Figure 28. Comparison of Predicted and Measured Drag at High Angles-of-Attack.

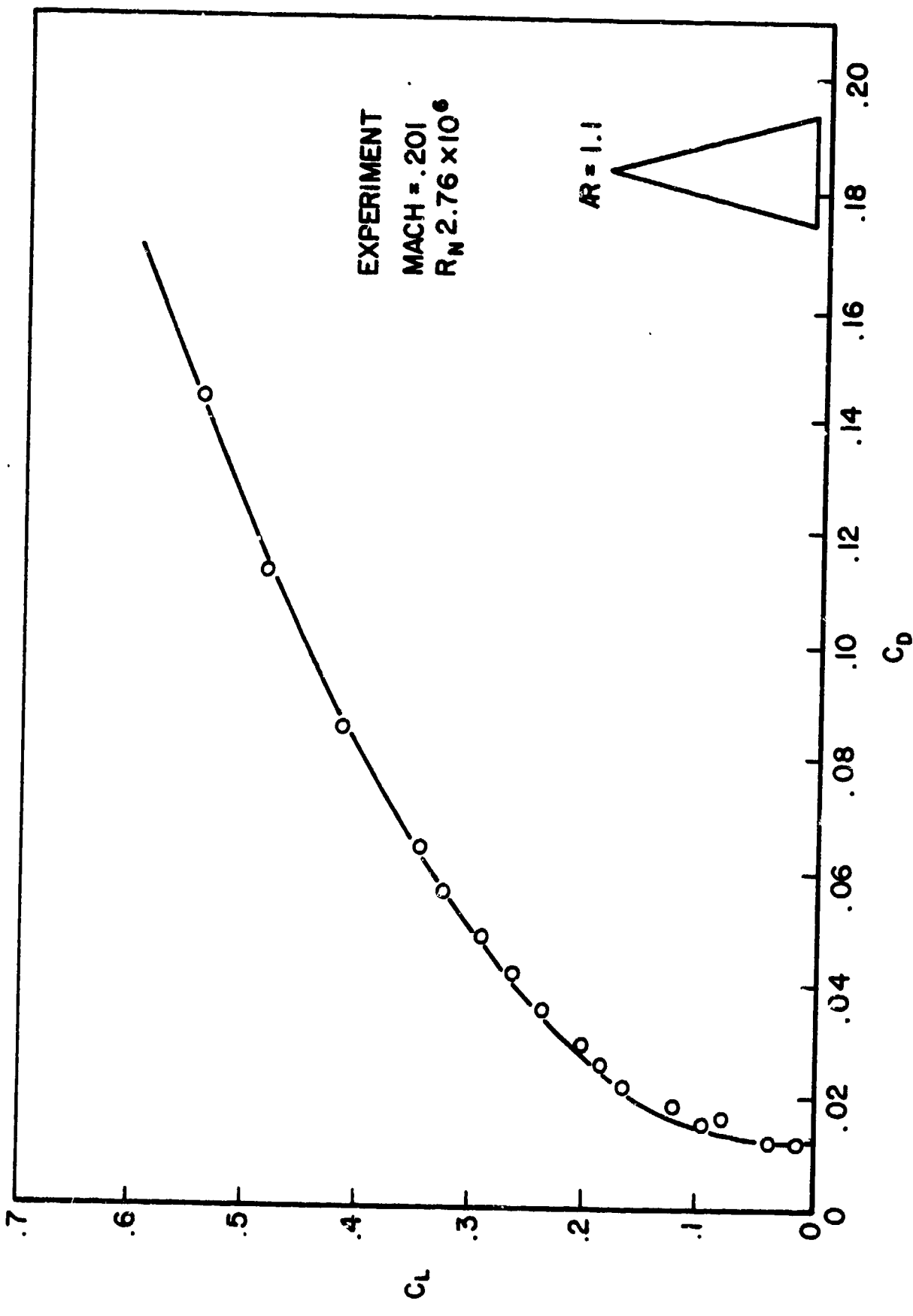


FIGURE 28. Comparison of Predicted and Measured Drag at High Angles-of-Attack (continued)

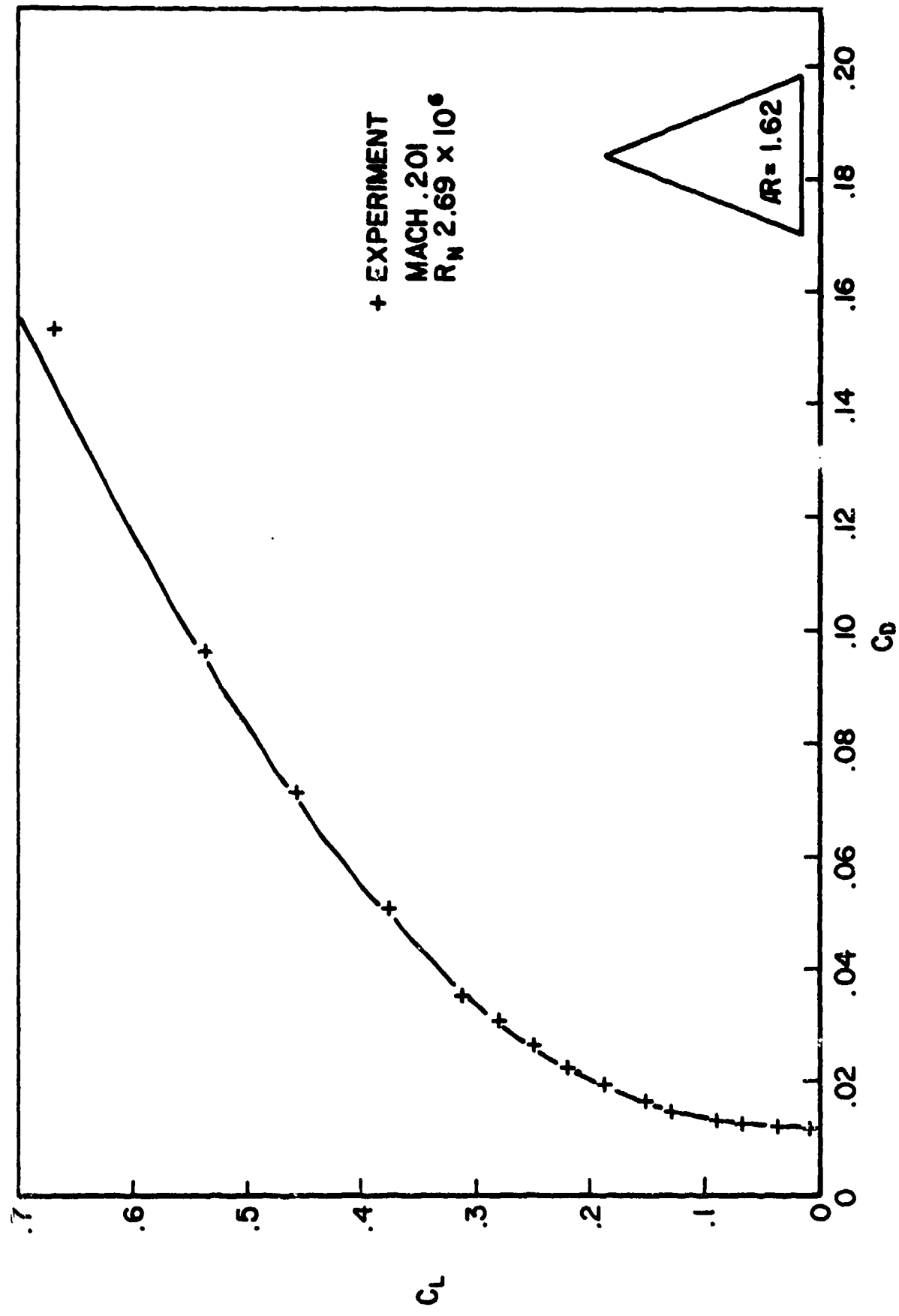


Figure 28. Continued.

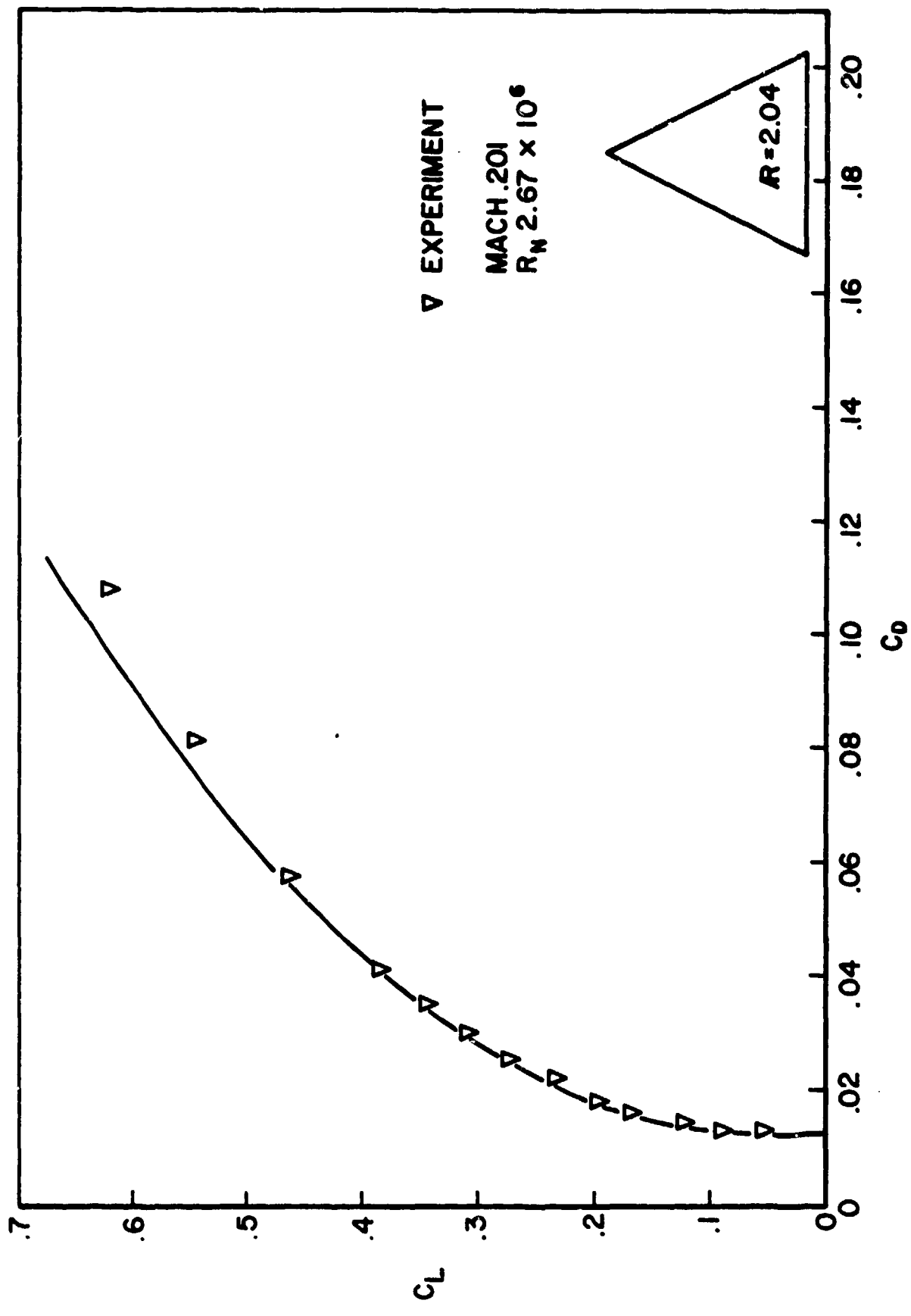


FIGURE 28. Comparison of Predicted and Measured Drag at High Angles-of-Attack (continued)

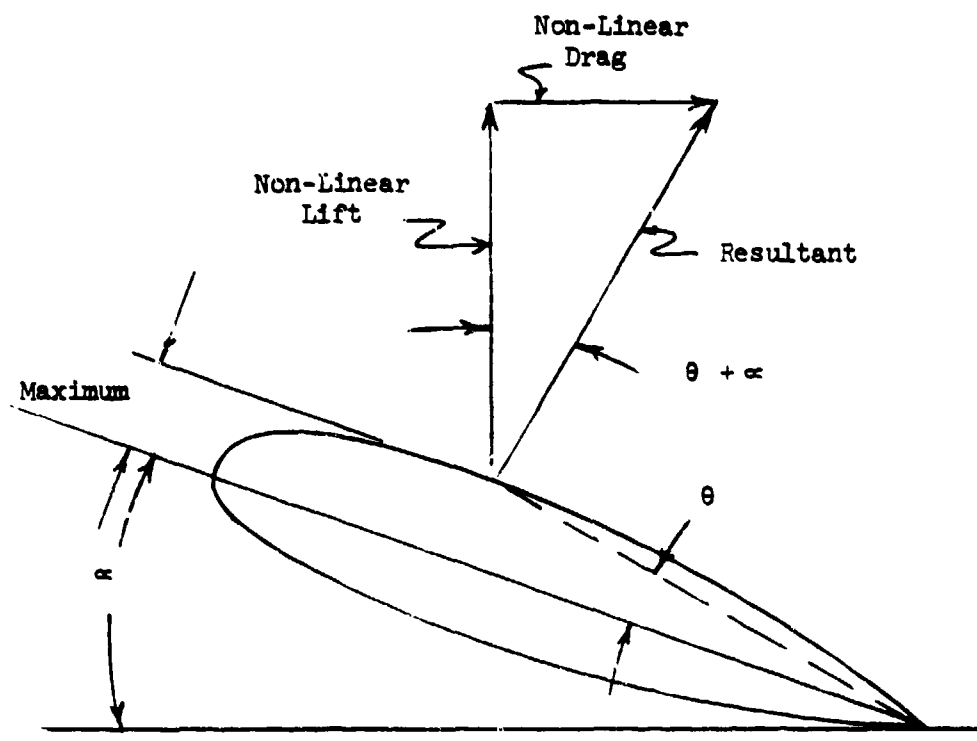


FIGURE 29. Method of Application of Non-Linear Drag

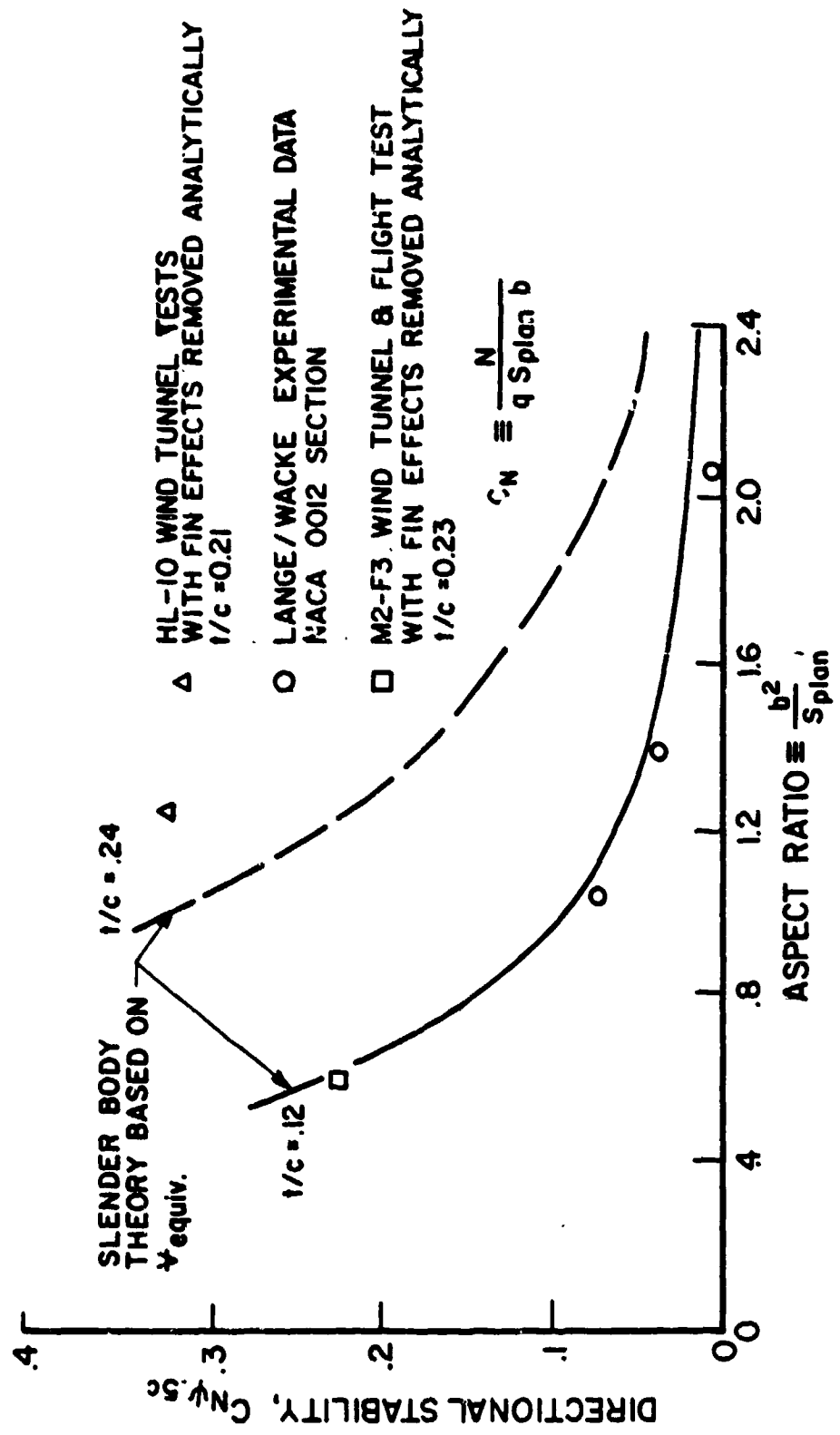


FIGURE 30. Directional stability derivative

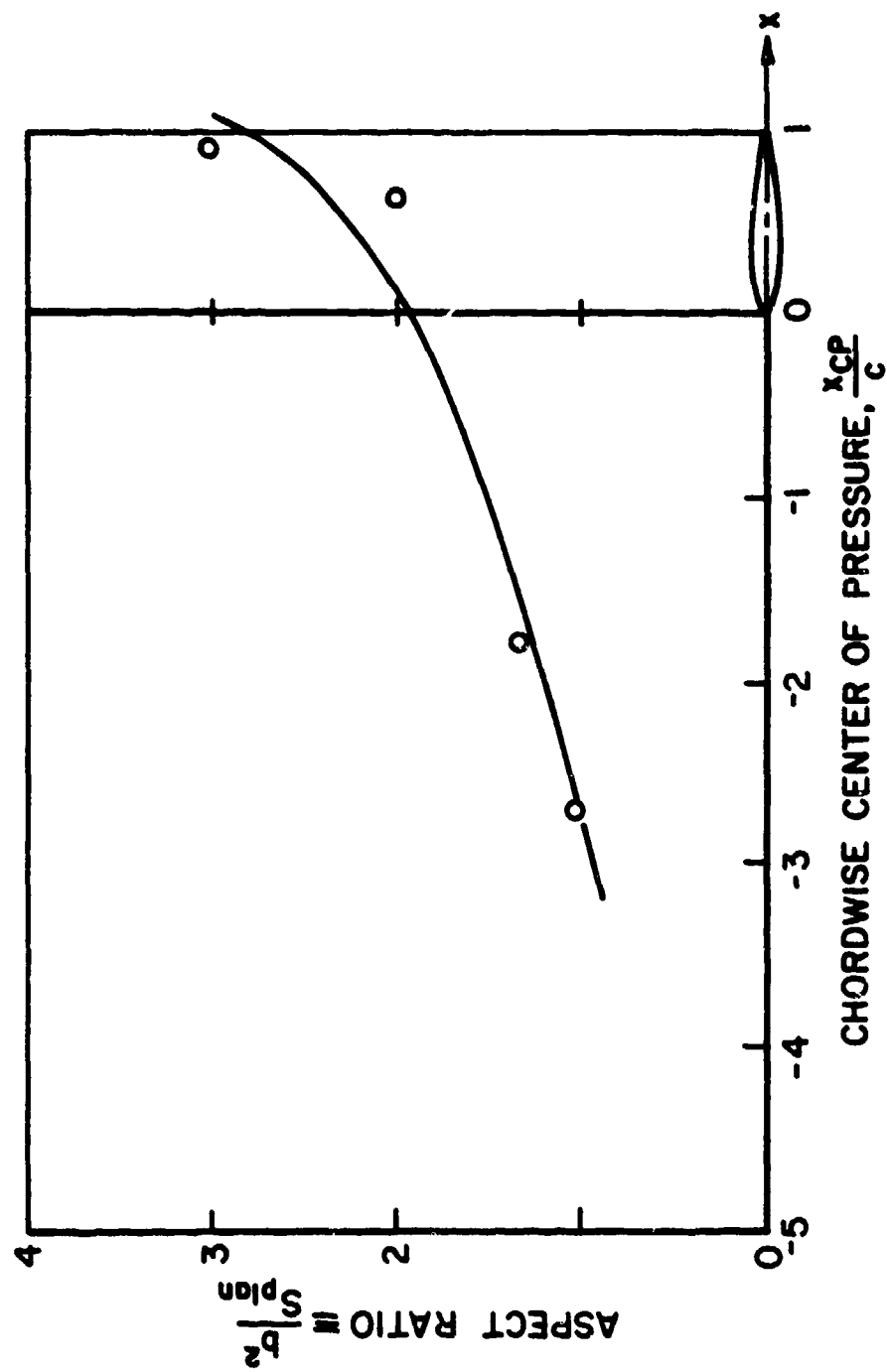


Figure 31. Center of Lateral Pressure Location.

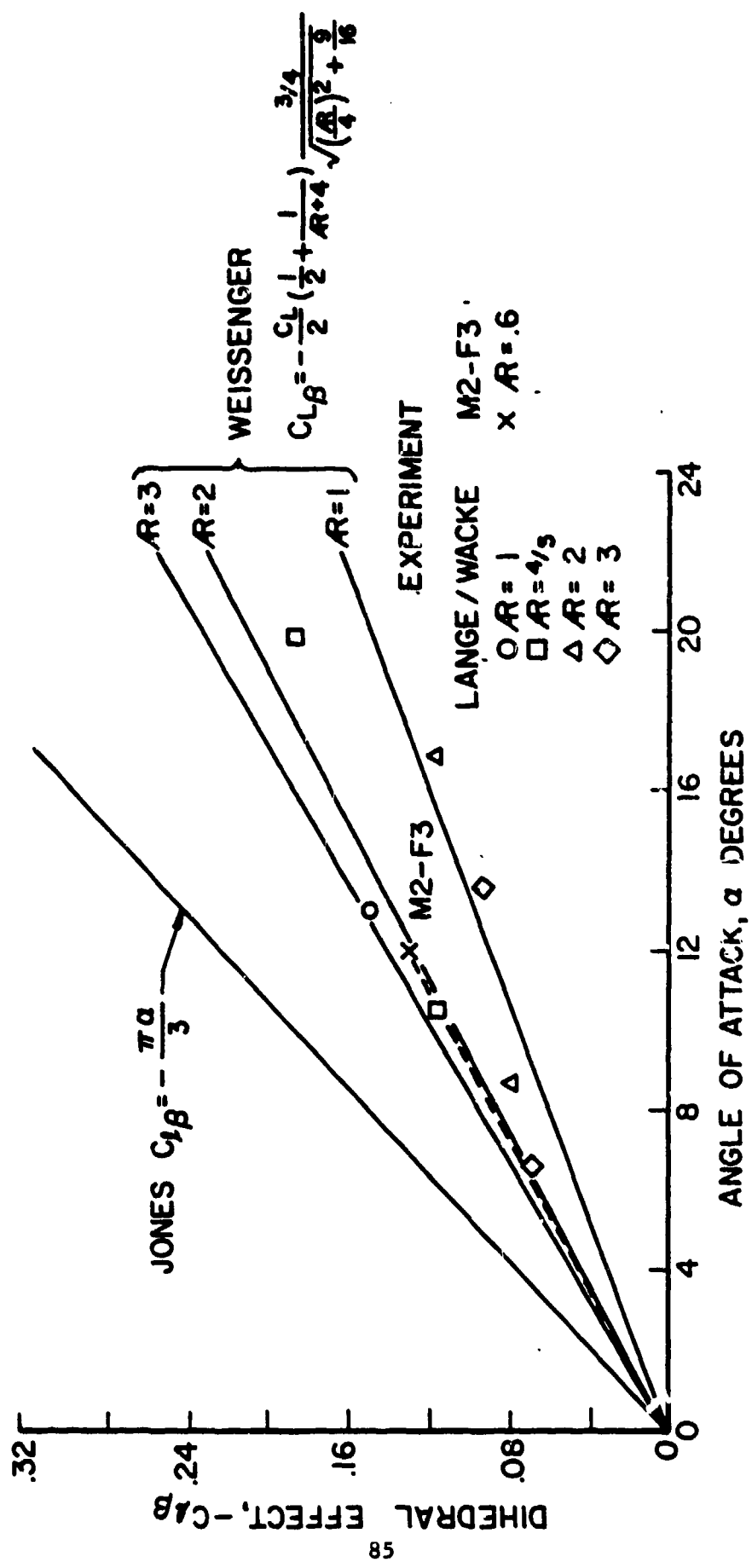


Figure 32. Dihedral Effect Derivative.

## AIRSHIP DRAG REDUCTION

The motivation for examining the possibilities for drag reduction of LTA vehicles is that even a small reduction in drag coefficient or power requirements, when considered over the relatively long duration of a typical mission, can result in a large increase in fuel economy, flight endurance, or payload capability. Basically, all means of drag reduction in some way or other involve controlling the boundary-layer flow either passively, by means of shaping or flow control slots, or actively, by means of blowing or suction. The following discussion reviews and evaluates these various methods as they pertain to conventional airships. Unfortunately, the amount of experimental verification is limited and in most cases insufficient to draw concrete conclusions. There is little doubt at this point that a great performance improvement over the past generation of airships is possible; however, it is also obvious that this benefit can not be realized without considerable further research and development.

### Drag Minimization Through Shaping Alone

The principle underlying the design of low-drag bodies by means of shaping is that of attempting to maintain a laminar boundary-layer along the body to the maximum extent possible without encountering boundary-layer separation on the aft portion of the body, References 57-62. It is desirable to have the position of transition (from a laminar to a turbulent boundary-layer), as far aft on the surface as possible without the risk of separation over the range of normal flight angles-of-attack. This situation is schematically depicted in Figure 33. Therefore, the approach depends on

the less-than-perfectly-understood subject areas of boundary layer transition and separation on three-dimensional bodies and consequently, relies heavily on empirical findings. For example, it is known from a combination of experiment and theory that the major factors affecting transition on a flat plate are: 1.) surface condition; 2.) free-stream turbulence level; and 3.) Reynolds number based on local length,  $Re_x$ . In addition, on a surface or body having thickness and therefore a pressure distribution, it is known that a proverse pressure gradient (decreasing) promotes the extent of the laminar boundary-layer, but that transition to turbulent flow occurs almost immediately when an adverse pressure gradient is encountered. Furthermore, the larger the unfavorable gradient over the rear portions of a body, the more likely is the occurrence of boundary-layer separation. Thus, in designing low-drag shapes, as the position of minimum pressure is located further aft the fraction of length over which pressure recovery can take place is less; the result is a larger unfavorable pressure gradient over the rear of the body and consequently, a greater likelihood of separation.

No analytical method exists to determine an optimum configuration for minimum drag based on the above considerations. At best, various analytical techniques all generate likely laminar flow shapes and it depends largely on the analyst to justify how many such bodies should be generated in searching for an optimum. Although no techniques exist for determining a true minimum-drag body, once a velocity (pressure) distribution has been specified, numerous mathematical methods exist to

calculate the corresponding body shape and vice-versa.

The factor which limits the extent of laminar flow is the critical Reynolds number. This is the value above which the boundary-layer becomes unstable and turbulent flow exists regardless of the surface condition or pressure gradient. If a significant portion of a hull is below the Reynolds number at which transition occurs, then it is possible to maintain laminar flow over the hull's forebody. Since the turbulent boundary-layer has the ability to negotiate an adverse pressure gradient over the rear of the body and resist separation, it is advantageous to design for transition to occur just at the maximum thickness point. If, however, the transition Reynolds number is reached before the maximum thickness point, the boundary-layer will become turbulent. As it will be demonstrated later, in the case where the transition Reynolds number is reached on the forebody before the maximum thickness point, the overall Reynolds number based on length determines whether or not the drag may be reduced by attempting to extend the length of laminar flow. The precise value of the transition Reynolds number is dependent on a number of factors and continues to be the subject of discussion. The values normally given for the flow over a flat plate in the absence of any external pressure gradient range from  $3.5 \times 10^5$  to  $5.0 \times 10^5$ . Under ideal conditions, the value most often cited in the case when an external pressure gradient is present is on the order of  $3 \times 10^6$ , although under particular circumstances, higher values have been observed.

A basic reference concerning the design of low-drag, laminar flow bodies is that of Young and Owen (Reference 57) in which a simplified

mathematical method is developed for calculating a given body shape from a pressure distribution that has been specified using the same principles as utilized in the design of low-drag airfoil sections. The technique is valid over a small range of yaw angles and for bodies with thickness ratios up to thirty percent. A more qualitative discussion of the problem, as well as some general background information, is given in the paper by Hertel (Reference 58), and that of Hamill (Reference 59). The paper by Galvao (Reference 60) outlines and justifies a straight-forward method for obtaining potential low-drag three-dimensional body shapes on the basis of tabulated laminar flow airfoil ordinates but, unfortunately, does not offer any means of obtaining the body's aerodynamic characteristics from those of the airfoil.

Carmichael's paper (Reference 61) is perhaps the most interesting in that it discusses a body shape for which the transition Reynolds number was as large as  $2 \times 10^7$ . Although this value was verified experimentally, it is probably not directly applicable to airships because it was obtained in the near ideal, low turbulence conditions of a deep-ocean drop-test with near-perfect body surface conditions. What is of importance is an excellent discussion and quantification of the maximum benefits that are to be gained by optimizing the body fineness ratio to achieve the largest gains possible in the drag trade-off between maximizing the extent of the laminar boundary-layer and flow separation. The results shown in Figure 34, taken from Reference 61, indicate the maximum downstream position at which the transition point can be located on a body of given fineness ratio without the occurrence of separated flow as a result of the pressure recovery region over the aft portion of the body. Although this figure is

for one particular Reynolds number, a similar one could be obtained for any value.

Of further interest is the potential drag reduction which can be obtained by designing for laminar flow with increasing values of Reynolds number. This discussion is summarized by Figure 35, also taken from Reference 61, in which the horizontal scale is the Reynolds number based on length while the vertical scale is the ratio of the body wetted area drag coefficient to the turbulent flat plate friction coefficient. As shown in the figure, slender bodies can achieve the benefit of laminar flow up to a length Reynolds number of  $6 \times 10^6$ , after which low fineness ratio is necessary to extend the range up to  $4 \times 10^7$ . Above a Reynolds number of  $1 \times 10^8$ , all body shapes will have very little laminar flow and the wetted area drag coefficient will exceed that of a turbulent flat plate by an amount which increases as fineness ratio decreases.

In addition to an excellent discussion on designing bodies of low drag, Carmichael's paper also specifies some of the practical limitations and causes of premature transition and should be of particular concern for a laminar flow designed airship hull operating in the atmosphere.

The last paper referenced that deals with drag reduction through shape manipulation is that of Parson, Goodson, and Goldschmied (Reference 62). This article actually develops an automated shape-synthesizing procedure in which a digital computer is utilized to optimize numerically a minimum drag body. Although the approach does not introduce anything new from a qualitative point of view, it should be of value in the designing of low-drag shapes.

In considering the potential of drag reduction by shaping for future airship applications, it seems clear that designing for laminar flow would be of some benefit to a small dirigible operating at low flight speeds and merits further investigation; however, it would assuredly be of little value on a large airship operating over any reasonable flight speeds. For example, consider the results of calculations presented in Figure 36. Two airships of different lengths are considered. The drag coefficient of these airships is expressed as a ratio of the drag coefficient of a fully turbulent flat plate as a function of flight velocity. The 350 ft long airship shows some significant drag reductions due to laminar flow design throughout most of the flight velocity range considered while the benefits to the 1,000 ft long vehicle are negligible except at extremely low flight velocities. In fact, at a flight speed of 40 mph, even under the most optimistic of circumstances, laminar flow can only be maintained on the forward 5 percent of body length.

From the preceding discussion and, in particular an examination of Figure 35, the problem of designing a laminar flow airship which must operate over a variation in flight velocities is also apparent. While a particular vehicle might enjoy all of the benefits of laminar flow at low and intermediate cruise, if its dash speed causes it to encounter a Reynolds number larger than  $1 \times 10^8$ , then it would have had less drag at that speed if it had not been designed with a low-fineness ratio, laminar flow shape. Thus, it is especially important that a modern LTA vehicle have its mission specified and its design point carefully selected.

As far as the actual practical implementation of laminar flow designs, there are several potential problem areas which are reason for caution, if not skepticism. For example, much of the current advocacy of laminar flow lighter-than-air vehicles is based on Carmichael's ocean drop-test result of a transition Reynolds number of  $2 \times 10^7$ . It should be emphasized that the free-stream turbulence level of the atmosphere is many times that found in the ocean depths, and consequently, the actual transition Reynolds number can be expected to be significantly smaller. The importance of a high transition Reynolds number to the argument for laminar flow airship design is shown in Figure 36 in which the drag reductions due to a laminar flow with  $Re_{trans} = 2 \times 10^7$  are superimposed with those for a more widely accepted value of  $Re_{trans} = 5 \times 10^6$ . While the lower transition value practically eliminates consideration of laminar flow design for airships, the actual attainable benefits probably fall between the two cases. One area in which further research is needed is in determining the maximum Reynolds number to which transition can be delayed under practical conditions.

Further limitations on the employment of laminar flow designs are the operational problems encountered in a real-world environment. The minimum surface conditions of roughness and waviness which are necessary to prevent premature separation (Reference 61) are actually fairly severe and could quite possibly by themselves be a prohibitive situation in that rain drops, insects, dirt, etc., are all sufficient to promote transition. Furthermore, if a laminar flow body is implemented but not

maintained to the required surface condition causing transition to occur forward of the maximum velocity position, then the drag of the hull will be larger than if the body had been designed for less laminar flow with the minimum pressure location coinciding with the actual transition location.

In concluding this section, it can be stated that while it is certainly probable that some gains in airship performance can be made by shaping alone, and because these gains are essentially free and should therefore be exploited, that designing for laminar flow is basically limited to smaller vehicles. At higher Reynolds numbers, the drag minimization will basically be that of eliminating separation while minimizing wetted area. This will involve an optimization of fineness ratio and will undoubtedly result in hull shapes which do not differ greatly from those of the past.

#### Active Boundary-Layer-Control by Suction

The pursuit of boundary-layer control (BLC) by blowing or suction has been the subject of active research since the time of Prandtl and numerous references are available in the literature discussing a variety of means by which active BLC may be obtained. Therefore, in order to limit the scope of this topic, only those approaches which suggest possible application to the drag reduction of modern airships will be considered. In evaluating the potential of a BLC system, the amount of useful volume taken up by the system's internal ducting and power requirements must be considered in the context of size and construction techniques likely for current LTA proposals. Furthermore, it is important that the overall power requirements are examined rather than just the

reduction in the hull drag coefficient. If the reduction in propulsive power due to the external drag reduction is greater than the internal power expended in restoring energy to the boundary-layer, then a net gain will be realized. Thus, boundary-layer-control by blowing is not discussed at all in that it is generally accepted, that for applications of most interest to airships, suction is capable of achieving the same benefits with much lower mass flows and therefore lower power expenditures. A brief general background in boundary-layer-control can be found in Thwaites (Reference 11) and Schlichting (Reference 53). An excellent source of more detailed information, much of which is of interest in BLC application to airships, is that of Lachmann (Reference 63).

Extending the laminar boundary-layer on airships by distributed, or area, suction has been proposed; the motivation for this follows from the preceding discussion. By such methods, it is possible to stabilize the boundary-layer to a transition Reynolds number that is over one hundred times larger than would normally be obtained (Reference 63). However, the same arguments concerning the diminishing benefits of laminar flow with increasing Reynolds number still apply, albeit not quite as severely. This can be demonstrated by a simple argument if one considers the skin-friction drag on a flat plate with suction as a function of Reynolds number, Figure 37. As the aim of distributed suction is to maintain a constant laminar boundary-layer thickness, and because of the rapid decrease in the turbulent skin-friction drag coefficient with Reynolds number, it can be seen that in order to obtain a drag coefficient that is proportionally lower than the turbulent value, the quantity of boundary-

layer that must be removed increases rapidly with increasing Reynolds number. Thus, with increasing Reynolds number, the point is eventually reached where the reduced drag coefficient does not offset the additional power requirements of the suction system. All in all, it is apparent that any possible benefits of using suction to maintain laminar flow are limited to airships of a small size operating at relatively low flight speeds. In addition, a number of practical limitations exist which include the fact that the porous skin is structurally weak and especially prone to failure from fatigue, the suction holes are easily clogged in an operational environment, and finally, the system requires a large amount of internal ducting which could occupy a great deal of the airship's useful volume.

The method of boundary-layer-control which shows the greatest promise for use in future airships is that of slot suction to prevent excessive boundary-layer thickening and flow separation on the stern portions of the hull. Basically, the minimization of drag on an axisymmetric body is a matter of optimizing the relationship between skin-friction drag and pressure drag due to flow separation. Without suction, for a given volume, drag due to flow separation becomes less as the fineness ratio is made large. Conversely, the drag due to skin-friction is minimized by reducing the wetted area suggesting a small value of fineness ratio. Thus, the minimum drag value for a given hull volume is obtained at a fineness ratio that optimizes the trade-off between skin-friction drag and separation drag. This is shown in Figure 38 which has been adopted from Goldschmied (Reference 64) for a representative body of revolution.

If the application of slot suction can prevent flow separation on the aft portion of the body, then it becomes possible to reduce significantly the wetted area drag by utilizing bodies with fineness ratios on the order of 1.5 to 3. A net drag reduction will then be realized if the sum of the hull drag plus the equivalent suction power drag is less than the drag of a body of equal volume without suction as shown in Figure 38. Note that once the fluid has been sucked into the body, it must be returned to free-stream static pressure and velocity so that it can be ejected ideally at zero velocity relative to the body. If it is ejected at any higher velocity it will generate thrust; therefore, the power in excess of that used to re-energize the boundary-layer fluid to the free-stream level is more appropriately charged to propulsive power rather than suction power.

An excellent discussion of the fundamental principles of designing for low-drag utilizing a singular suction slot is that of Goldstein (Reference 65). Briefly however, what is involved is an attempt to shape the body such that the adverse pressure gradient, necessary for pressure recovery over the rear of the body, becomes concentrated over a short longitudinal distance. By applying suction at this location, energy is supplied which stabilizes the boundary-layer and prevents flow separation. An example of such a shape and its calculated velocity distribution is presented in Figure 39. In this case, the adverse pressure gradient is concentrated at eighty-three percent of the body length while the pressure distribution at all other body stations is favorable.

In evaluating the potential of the application of single-slot suction boundary-layer-control for airships, it is fortunate that there is both theoretical and experimental work, References 64-69, from which to draw conclusions. For the most part, all of these references are based on a relatively extensive research program by Goodyear during the mid-fifties in which the potential of a BLC airship was investigated. The original reports, References 66-68, develop a theoretical method for considering a BLC airship and verify the result by an experimental program carried out by the David Taylor Model Basin (NSRDC). On the basis of these tests, a comparison is made between the BLC airship and a representative Navy blimp, the XZS2G-1.

The shape chosen in the Goodyear single suction-slot BLC research program was that of a thirty-four percent thick Lighthill airfoil rotated about the longitudinal axis to yield a body of revolution having a 3.1 fineness ratio. It is important to point out that in choosing this shape, no attempt was made to find an optimum but rather it was selected arbitrarily as one offering enough potential to permit a valid initial evaluation of the BLC concept. In the wind tunnel experiments at DTMB, a model of the BLC airship's bare hull was compared to that of the XZS2G-1. Both models were tested over a Reynolds number range from  $4.0 \times 10^6$  to  $1.2 \times 10^7$  with transition artificially stimulated at the ten percent body station in order to achieve a turbulent boundary-layer over most of the length as would be the case in full-scale. Without suction, the BLC shape had a drag coefficient nearly fifty percent higher than that of the XZS2G-1. With suction applied, the value of the ideal drag coefficient, of the BLC airship, in which the boundary-layer is isentropically returned to

free-stream conditions, was from twenty percent to thirty-eight percent lower than that of the blimp over the entire range of Reynolds numbers tested. A summary of the experimental results is shown in Figure 40, taken from Goldschmied (Reference 64), in which these results are compared to data taken from other sources\*. The results obtained in these experiments were in good agreement with those obtained theoretically by the method developed in Reference 68 and thus provide some credence to the full-scale calculations and comparisons.

To determine the full-scale potential of a BLC airship, in Reference 68 the experimentally verified theory was used to predict the bare-hull drags of both a BLC airship as well as that of a conventionally-shaped blimp hull. A volume of one million cubic feet was chosen for both hulls as this enabled the theoretical drag prediction of the conventional hull to be correlated with actual flight test data. The comparison was carried out for the Reynolds number values of  $1 \times 10^8$  and  $2 \times 10^8$ , which corresponds to flight speeds of 35 knots and 70 knots respectively. In reviewing this theoretical performance comparison of the two airships, it is apparent that every attempt was made to obtain conservative results and that they are as realistic as possible in relation to the experimental data available. The results, which include a conservative estimate of ducting losses, pump efficiencies, etc., indicate that at the lower value of Reynolds number, the BLC airship has a bare-hull drag coefficient twenty-three

---

\*It should be pointed out that the DTMB experiments also included a study of a BLC airship in which an aft-mounted, auxiliary ring-wing was used in an attempt to passively achieve the same effects as obtained with slot-suction. Although the experimental findings were not encouraging, it was emphasized that the testing was not extensive enough to generate any firm conclusions.

percent less than that of the conventional hull and at the large value of Reynolds number, it is twenty percent less. Thus, because of the conservatism in the approach and the wide margin of improvements, on the basis of this comparison, it is clear that this type of BLC is capable of producing a significant reduction in drag over that of a conventional airship. Note, however, that once the boundary-layer fluid has been sucked into the body and brought up to zero velocity relative to the body, it is in a condition to be used most effectively by the propulsion system in generating thrust. Therefore, as emphasized in the Goodyear study, in order to realize the full potential in the overall reduction of an airship's power requirements, the use of BLC must be integrated with the vehicle's propulsion system as will be discussed in a later section.

#### Stern Propulsion for Airships

The potential benefits of a stern-mounted propulsion system hold a great deal of promise for producing a significant reduction in the overall power requirements of modern airships, References 70-72. The mechanism for achieving these benefits can be demonstrated by momentum theory considerations alone. The thrust produced by a propeller operating in axisymmetric flow is given by

$$T = \rho A_p (V_1 + v) 2 v$$

and the corresponding propulsive power (exclusive of profile effects) is

$$P = T (V_1 + v),$$

where  $V_1$  is the local flow velocity and for wake propulsion considerations is generally less than the free stream velocity. Combining,

$$P = \frac{T}{2} \left( V_1 + \sqrt{V_1^2 + \frac{2T}{\rho A_p}} \right)$$

which indicates that for a given thrust and propeller size, the propulsive power will decrease as the propeller remote inlet velocity  $V_1$  decreases. Hence, a wake-immersed propeller can produce the same thrust for less power than one operating in the free stream. In addition to the reduction of propulsive power requirements, other possible advantages cited by proponents of stern-drive are: 1.) that because of less noise and vibration, an isolated stern-mounted power unit is less disturbing to crew members and instruments than a conventional, hull-mounted power system, 2.) the stern-drive system permits the removal of a number of external drag sources such as engine nacelles, brackets, etc. It has also been suggested that the stern-mounted propeller allows for the possibility of generating turning moments for control by means of cyclic-pitch from an articulated rotor and thereby allow a further reduction in drag by reducing control surface size. This approach, however must be carefully studied owing to the relatively low thrust forces required and the resulting small control moments available from articulated rotors.

Much of the support for implementing an open-wake propeller comes from the report by Cornish and Boatwright (Reference 70), in which full-scale drag and boundary-layer measurements were made on the Navy ZS2G-1. In these experiments, it was found that most of the drag was due to skin-friction rather than separation. This fact prompted a considerable effort to clean-up the airship hull and appendages which resulted in a twelve

percent reduction in drag. In addition, it was recommended that the vehicle be reconfigured with a wake-mounted propeller which, on the basis of the experimental data, was shown to provide at least a ten percent reduction in power requirements over the entire range of flight speeds from 35 to 70 knots. This report also proposes the development of an articulated, helicopter-type rotor for the wake propeller so that cyclic pitch can be used to generate control forces. Thus, a further reduction in drag could be realized by the removal of the empennage and external bracing. Through the implementation of the refinements outlined, it was estimated that the design shown in Figure 41 would have a drag only forty-two percent of the value measured for the original configuration.

The subject of a paper by McLemore (Reference 7) is a series of wind-tunnel tests using a self-propelled, 1/20 scale model airship of 5:1 fineness ratio and utilizing an open-wake stern propeller. These experiments were performed in the full-scale tunnel at the NASA-Langley Research Center. The model, representative of the last operational Navy airship, was tested at Reynold numbers of  $1.2 \times 10^7$  and  $1.8 \times 10^7$ .

Before considering McLemore's results, it should be noted that in the case of an airship propelled by stern-drive, the propeller and propulsive efficiencies in excess of one hundred percent are attainable. This is not too surprising considering, that in an absolute frame of reference, the propulsor makes use of energy put into the boundary-layer by skin-friction. Furthermore, the standard definition of propeller efficiency,

$$\eta = \frac{TV_{\infty}}{P}$$

where

$T$  = propeller thrust, lb.

$V_\infty$  = free-stream velocity, ft/sec.

$P$  = shaft power, ft-lb/sec.

involves the free-stream velocity while the propeller actually operates in the reduced velocity flow-field. Because of this lower velocity in the wake, the propeller can produce more thrust per horsepower than it could in the free-stream. Thus, the results of the wind tunnel experiments, Reference 72, found propeller efficiencies as high as one hundred forty percent at reduced thrust conditions and concluded, that by properly designing propellers specifically for operation in the wake of an airship, it should be possible to obtain the high efficiencies even at full-thrust levels.

In order to determine if the values of propeller efficiency were obtained at the expense of some additional factor, such as an increase in hull drag, the value of propulsive efficiency was calculated as

$$\eta_e = \frac{C_{T_E}}{C_p} \frac{V_\infty}{nD}$$

in which

$C_{T_E}$  = propeller propulsive thrust coefficient,  $\frac{\pi^{2/3}}{2D^3} C_{D_e} \left(\frac{V_\infty}{nD}\right)^2$

$C_p$  = power coefficient  $\frac{P}{\rho n^3 D^5}$

$n$  = propeller rotational speed, rad/sec

$D$  = propeller diameter, ft

$C_D$  = measured drag coefficient,  $\frac{\text{Drag}}{q_\infty \frac{V^2}{2}}$

$C_{D_e}$  = effective drag coefficient,  $C_{D_e} = C_D - C_D$

$C_{D_0}$  = drag coefficient, propeller off:  $C_{D_0} = 0.021$

$V$  = hull volume, cu. ft.

$q_\infty$  = free-stream dynamic pressure, lb/sq. ft.

$\rho$  = mass density of air, slugs/cu. ft.

The case of a measured propeller efficiency in equilibrium cruise of one hundred twenty-two percent yielded a value of one hundred three percent for the propulsive efficiency. This decrease was attributed to an increase in hull pressure drag, similar to flow separation drag, when the wake propeller was operating. Thus, it was concluded that the gains produced by an open-wake propulsion system are somewhat offset by an increment in the drag coefficient from ten percent to twenty percent, depending on the hull-propeller combination. The propulsive efficiency for an airship with a conventionally-mounted propeller was found to be only fifty-nine percent. Thus, the stern-mounted propeller accounts for a decrease in the power required by a conventional airship of over forty percent. If these results are extrapolated to include the case of a properly designed wake-propeller which retains a high efficiency at high thrust levels, then the stern-driven airship would be expected to require less than fifty percent of the power required by the conventional design. In addition to the benefits to be derived from the use of stern-wake propulsion, there are a number of potential problems which

must be considered. For example, as found in the wind tunnel testing of Reference 72, the high values of propulsive efficiency obtained with an open wake propeller are very dependent on the airship's angle-of-attack. Furthermore, it is important to keep all of the propeller's diameter in the boundary-layer wake. For maximum efficiency, the design of the wake propeller must take into account the non-uniform inflow velocity arising from the boundary-layer's normal velocity gradient.

In reviewing both the potential advantages and difficulties associated with the stern-mounted, open-wake propeller, it is concluded that an internal, shrouded propulsor with a boundary-layer intake duct provides an obvious alternative which capitalizes on the advantages of stern-drive and eliminates many of the disadvantages of an open-wake propeller. Not only does this system assure that the whole propulsor is immersed in fluid from the boundary-layer, but also helps to alleviate the separation-like drag associated with the open-wake propeller. In addition, unlike the performance of the open-wake propeller which deteriorates rapidly with angle-of-attack, the internal propulsor is estimated to allow an angle-of-attack variation up to a specified angle (for instance,  $7^{\circ}$ ) without adverse effects (Reference 64). Furthermore, as shown in Figure 42, the ducted propulsion system's boundary-layer intake can be combined with an annular suction-slot boundary-layer-control system, as previously discussed, in order to prevent separation on a low fineness ratio, low-drag body. Thus, the application of boundary-layer-control and stern propulsion are complimentary and, to achieve the maximum benefit of each, should be considered as an integrated system in the design of an advanced-concept airship.

### Integrated Hull Design: Boundary-Layer-Control and Propulsion

Although it has been concluded that the application of both boundary-layer-control and stern propulsion can improve the performance of a modern LTA vehicle, it was emphasized in the Goodyear BLC airship study that, in order to realize the full potential of these principles, it is necessary to combine them properly into modern airship design, Reference 64-69. Once the boundary-layer-control fluid has been brought into the body and returned to the ideal (minimum drag) discharge velocity of zero relative to the vehicle, it is in a condition to minimize the propulsion power if it is used by the propulsor to generate thrust. In concept, the moving vehicle puts kinetic energy into the fluid which is dragged along by the body. This energy is stored in the moving boundary-layer and, unless recovered and re-energized, is wasted when the fluid from the boundary-layer passes into the airship's wake.

A schematic diagram of a combined suction/propulsion system is shown in Figure 42. Conceptually, the BLC section and the propulsion section of the design comprise two separate stages in the pumping system. The BLC stage of the system includes the annular suction-slot intake and the annular duct leading to the impellor. For analysis purposes the power input into this stage is assumed to be just that which is sufficient to bring the ingested fluid to free-stream conditions, as any discharge level in excess of this must be charged to propulsion rather than suction. The propulsion system includes an additional pump stage to provide thrust and the fluid exit duct. A common impeller is shared for the pumping duties of each of the stages.

The study of an airship which combined boundary-layer-control with an advanced propulsion system was the topic of the BLC airship investigation by Goodyear previously cited and described. The final report of that program, Reference 68, culminates in a theoretical comparison, based on experimental verification, of the propulsion requirements of a combined hull design, boundary-layer-control and stern propulsion airship (BLC-P), to that of a conventional airship of an equivalent volume (one million cubic feet). These two vehicle designs are shown pictorially in Figure 43. For the BLC airship, it was assumed that the reduction in structural weight due to the lower fineness ratio, as well as the savings attributable to the removal of the supporting structure necessary for the car mounted propulsion units, was just offset by the weight of the installed BLC system. Thus, both vehicles were considered to be of equal weight and would therefore have equal fuel capacities. In calculating the propulsive requirements, momentum theory for ducted propellers was used for the BLC-P design and the propeller efficiency was assumed to be ninety-five percent. For the conventional airship, momentum theory for free-propellers was used and the efficiency was taken as ninety percent. Although it was found to have little effect, the propeller diameter on the BLC-P vehicle was allowed to vary from 11 to 26 feet. The conventional airship's power requirements were calculated for the cases of a single 16.5 ft. diameter propeller and two 16.5 ft. propellers.

Because of the considerable structure required in the stern for the BLC system, the study design allowed cantilevered tail surfaces such that the drag due to empennage bracing cable was eliminated. Furthermore, the

removal of car-mounted propulsion units eliminated the external drag of outriggers and engine nacelles, although a similar drag increment had to be included in calculating the ducting losses. Thus, on the basis of a component drag build-up, the BLC-P airship was found to have twenty-one percent less accessory drag area than the conventional design.

The results of this detailed comparison were such that the BLC-P configuration was found to have fifteen percent to twenty percent lower power requirements than the conventional airship. If for lower thrust requirements, however, the conventional airship is unable to drive two propellers off a single engine as is generally the case, then below 40 knots the BLC-P airship would show a twenty-five percent to thirty percent power improvement. For cruising flight at neutral buoyancy, a twenty to twenty-five percent increase in endurance was calculated for the BLC-P design, and improved to forty percent at lower speeds. Clearly, these calculations indicate that a significant performance advantage over the conventional airship is possible with the combined hull design. Furthermore, in considering the results of the Goodyear study, they should be regarded as being as realistic as possible on the basis of the information available and, where assumptions had to be made, it is apparent that efforts were taken to keep them conservative.

In addition to the performance benefits of the BLC-P design proposal, the Goodyear study also makes note of several operational advantages. (1) In reducing the fineness ratio from 4.5 to 3.0, the static instability of the envelope decreases on the order of fifteen percent. Because the tail

moment from the center-of-buoyancy remains essentially unchanged, as shown in Figure 43, it is a possibility that the area, and therefore the drag, of the tail surfaces might be reduced. In addition, because of the tail-cone strength, it is possible that fins of higher aspect-ratio, and consequently higher lift-curve slopes, might be employed. This modification would provide improved static stability, although possibly at the expense of damping which seems dependent on a favorable aerodynamic hull-fin interference effect proportional to the length of the fin's base chord. In any case, it is evident that the stability and control of the BLC-P configuration would be optimized around design constraints different from those of the conventional airship. Because of a greater flexibility in the choice of the final fin configuration, it is possible that some improvements could be obtained using the BLC-P hull concept. (2) An additional advantage of the BLC-P design is the potential of vectoring the fluid discharge from exit jets in order to obtain low-speed control capability. Similarly, if an articulated propeller is to be utilized for control, the shrouded propulsion provides the propeller with protection from physical damage in flight and ground handling. (3) The placement of the BLC-P airship's propulsion system in the stern of the vehicle isolates both the crew and instruments, such as sonar, from powerplant noise and vibration. This benefits crew comfort as well as mission effectiveness.

A more recent study applicable to modern airship design is that of Goldschmied (Reference 64). Although based on the earlier Goodyear BLC-airship research, this less-conservative approach reformulates the theoretical analysis and arrives at an advanced hull design in which boundary-layer-control and stern propulsion are fully integrated (H-BLC-P). This

report further develops the propulsion analysis such that the trade-off between suction power and propulsion power is optimized to obtain the highest efficiency possible and minimize the total power requirements. It was found that the power required for this type of vehicle could theoretically be minimized if the relationship between the equivalent suction drag and the wake drag were in a ratio of approximately two-to-one. For this refinement, the calculated power required was only twenty-eight percent of that required by the conventional airship. While this figure might initially appear overly optimistic, in light of the experimentally determined results of McLemore (Reference 72), as well as Cornish and Boatwright (Reference 70), it might indeed represent a realistic lower boundary on what is attainable. Most likely, however, the truth probably lies between this result and the extremely conservative results presented in the Goodyear study. At any rate, the indication is clear that significant performance gains over past airships are theoretically possible and the use of an integrated hull design shows sufficient potential to merit a considerable research effort in advanced LTA development.

Although some aspects of the stability and control of BLC airships have been mentioned above a number of interesting issues are raised which must be given detailed consideration. If, in fact, the BLC system produces a flow field over the airship hull that closely approximates potential flow then the hull will not generate any side force with sideslip and consequently it will not be possible for the airship to turn. In addition the unstable moments produced by sideslip and angle-of-attack will tend to approach the potential flow value which tends to be 30 to 40 percent larger than the value measured for airship hulls.

It is also possible that a stern mounted propeller will not provide satisfactory levels of control moments. Recall that the thrust of the propeller is constrained to be equal to the drag of the airship, which has been reduced as much as possible by the BLC system. Consequently, the control moments available will become smaller as the flight speed and drag are reduced.

#### CONCLUSIONS AND RECOMMENDATIONS

The potential gains in reducing the overall airship power requirements that might be possible by the employment of the techniques examined in this survey are summarized in the bar-graph of Figure 44. Thus the following conclusions are drawn in regard to possible performance gains of modern airships in relation to those of the past.

- 1.) Designing for low drag by attempting to maintain long runs of laminar boundary-layer on a body can only be of benefit for an airship in which the overall Reynolds number based on length is less than  $1 \times 10^6$ . Thus, passive boundary-layer-control by means of shaping for laminar flow is not effective for large LTA vehicles and moderate speed missions.
- 2.) Based on experimental data, a modern BLC-airship using an annular suction-slot to prevent flow separation on a low-fineness ratio body can conceivably lower the total drag of a hull twenty percent below that of a conventional hull of equal volume.

- 3.) An airship utilizing a stern-propulsion system can realize a power savings of forty to fifty percent over that required by a conventional design with car-mounted propulsion units.
- 4.) In order to insure that the benefits possible with boundary-layer-control and stern propulsion are maximized, it is necessary to properly combine these concepts into a fully integrated design. Under these circumstances, it should be possible to obtain power requirements which are, at the least, a twenty-five percent improvement, and possibly even a fifty-five to seventy percent improvement, over the requirements of a conventional airship.

In order to obtain results from the various analyses and experiments which were the basis from which the preceding conclusions were drawn, a number of assumptions, based on engineering judgement, had to be made. Furthermore, for the most part, these studies were relatively limited in scope. Thus, before the development of an propulsion integrated, boundary-layer-controlled airship can progress further, these studies must be expanded and the numerous assumptions verified. Therefore, the following recommendations are made:

- 1.) The body shape utilized in the majority of the BIC-airship studies to date has been rather arbitrary. As this feature could have a considerable influence on the benefits that might be derived from an integrated hull design, additional experimental and analytical work is necessary in attempting to define an optimum body shape, including fineness ratio, for future advanced LTA vehicles.

- 2.) Wind tunnel experiments using a self-propelled model, such as the one utilized in Reference 72 except employing the complete H-BLC-P concept, should be performed to test the validity of the theoretical conclusions thus far obtained. This program should include an extensive experimental examination of the benefits to be derived from an optimum trade-off between suction power and propulsion power as analytically examined by Goldschmied in Reference 64. In addition, the effects on the H-BLC-P airship of suction-slot geometry and angle-of-attack variation should be investigated.
- 3.) A detailed examination of the practical design requirements of an advanced, integrated-hull airship should be undertaken. Much engineering concerning the ideal ducting arrangements, and so forth, remains to be done.
- 4.) Finally, a detailed stability and control analysis of the H-BLC-P airship has yet to be performed. This should include an evaluation of possible means for obtaining control at low-speeds through the use of vectorable thrust in one form or another. In addition, a question that has yet to be addressed concerns the mechanism by which maneuvering is achieved when BLC causes the flow over the hull to approach that of potential flow. In a true potential flow, although the unstable moment would remain, yawing the hull would no longer generate side forces required to sustain a curved flight path. Although a truly potential flow situation is unlikely, the maneuvering of a BLC-airship may pose an interesting problem.

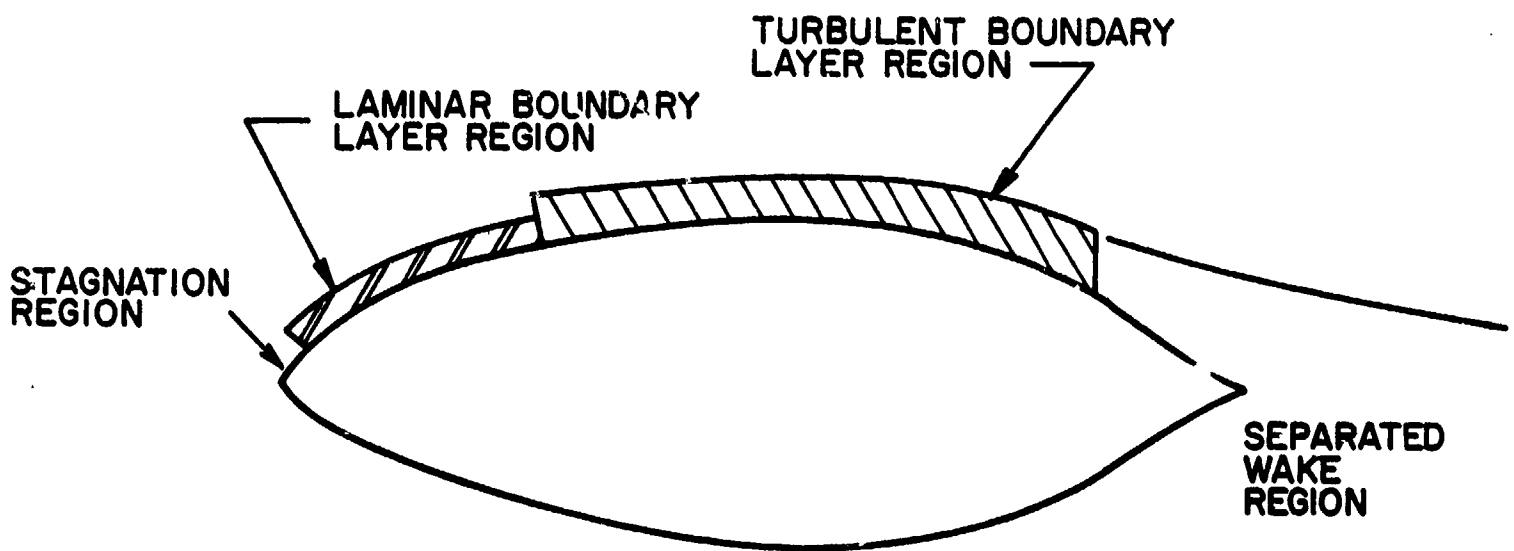


FIGURE 33. Model of Flow Over Body of Revolution

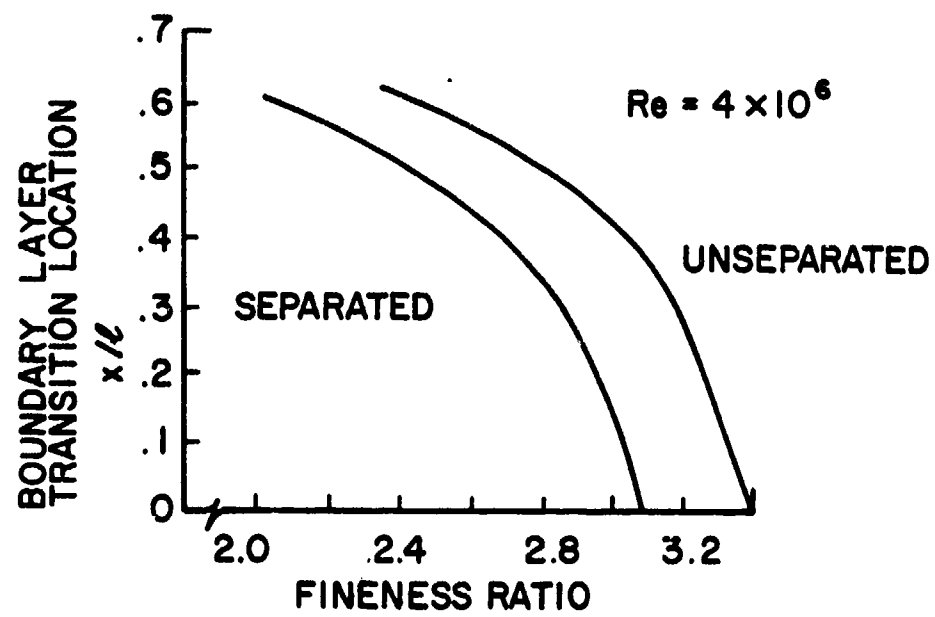


FIGURE 34. Transition Location as a Function of Fineness Ratio and Its Effect on Separation

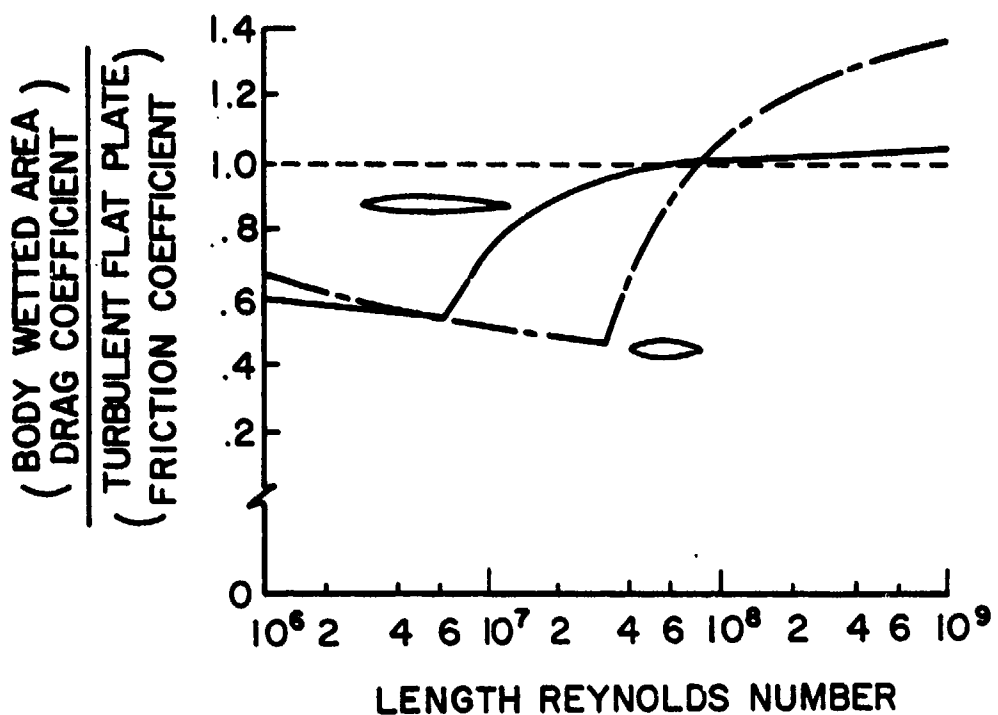


FIGURE 35. Effect on Laminar Flow Design of Increasing Reynolds Number

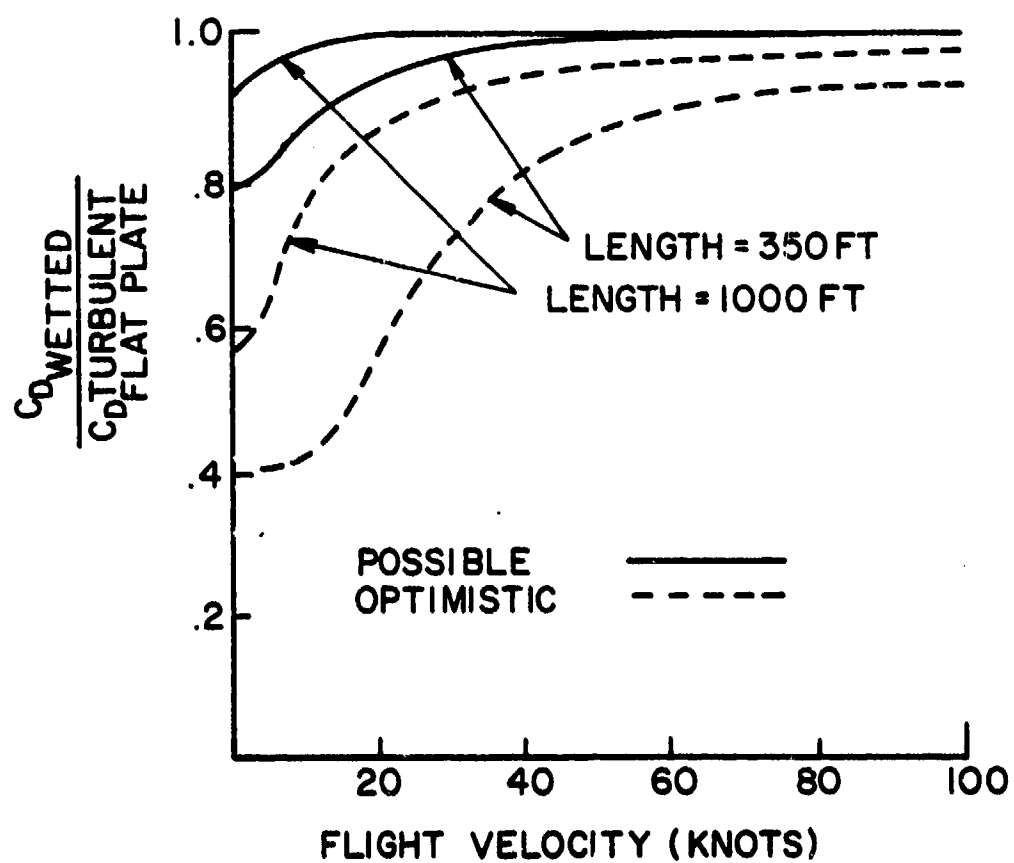


FIGURE 36. Effect of Increasing Flight Velocity on Drag Gains Achieved by Laminar Flow Design

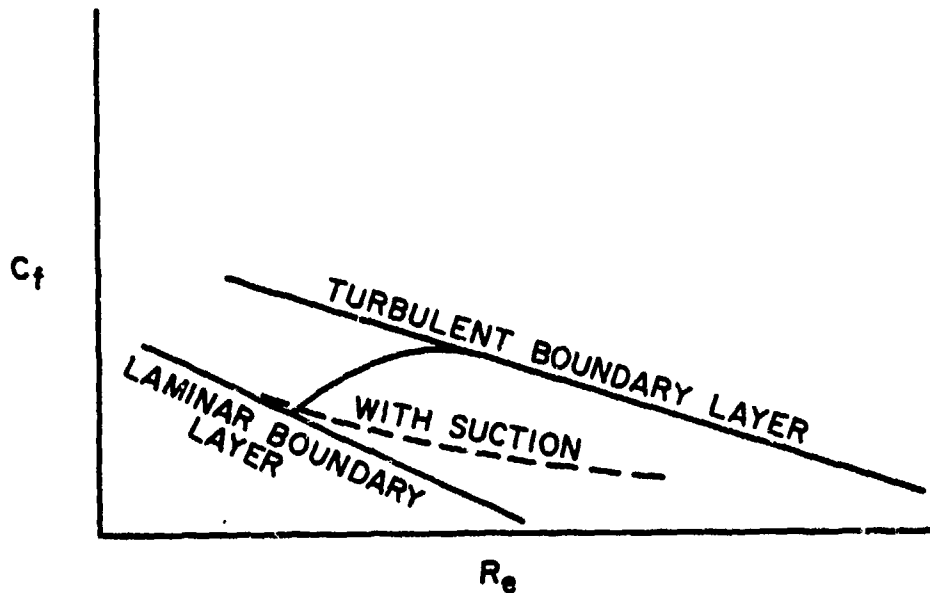


FIGURE 37. Coefficient of Skin Friction of a Flat Plate at Zero Incidence with Suction

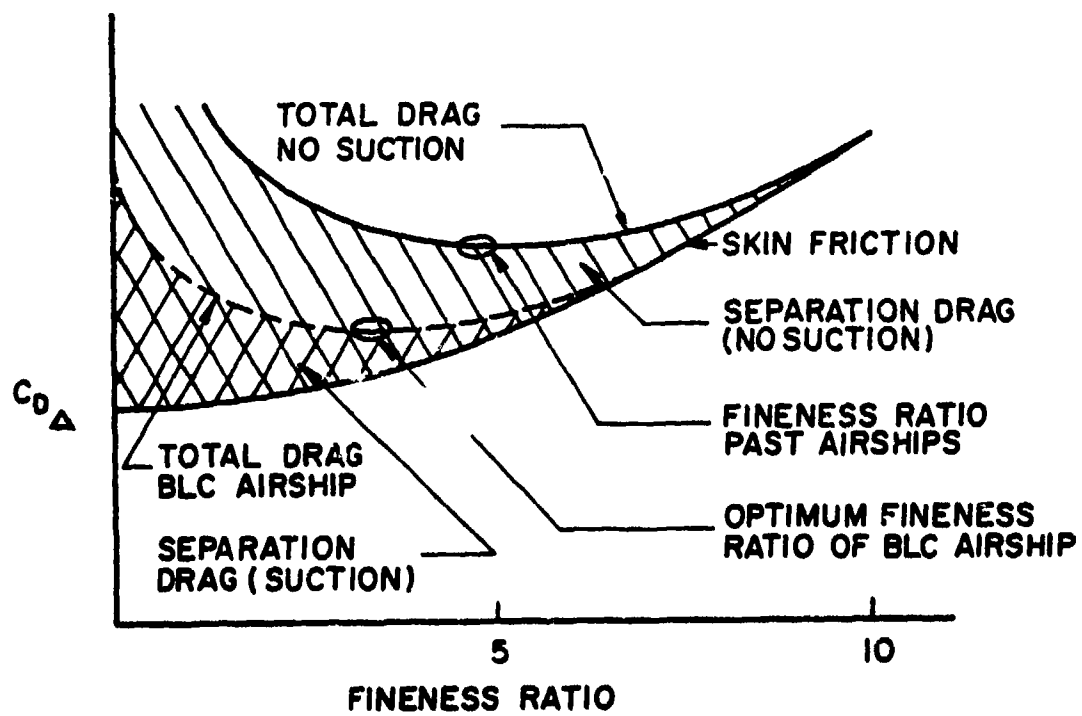


FIGURE 38. Effect of BLC of the Overall Drag of Airships

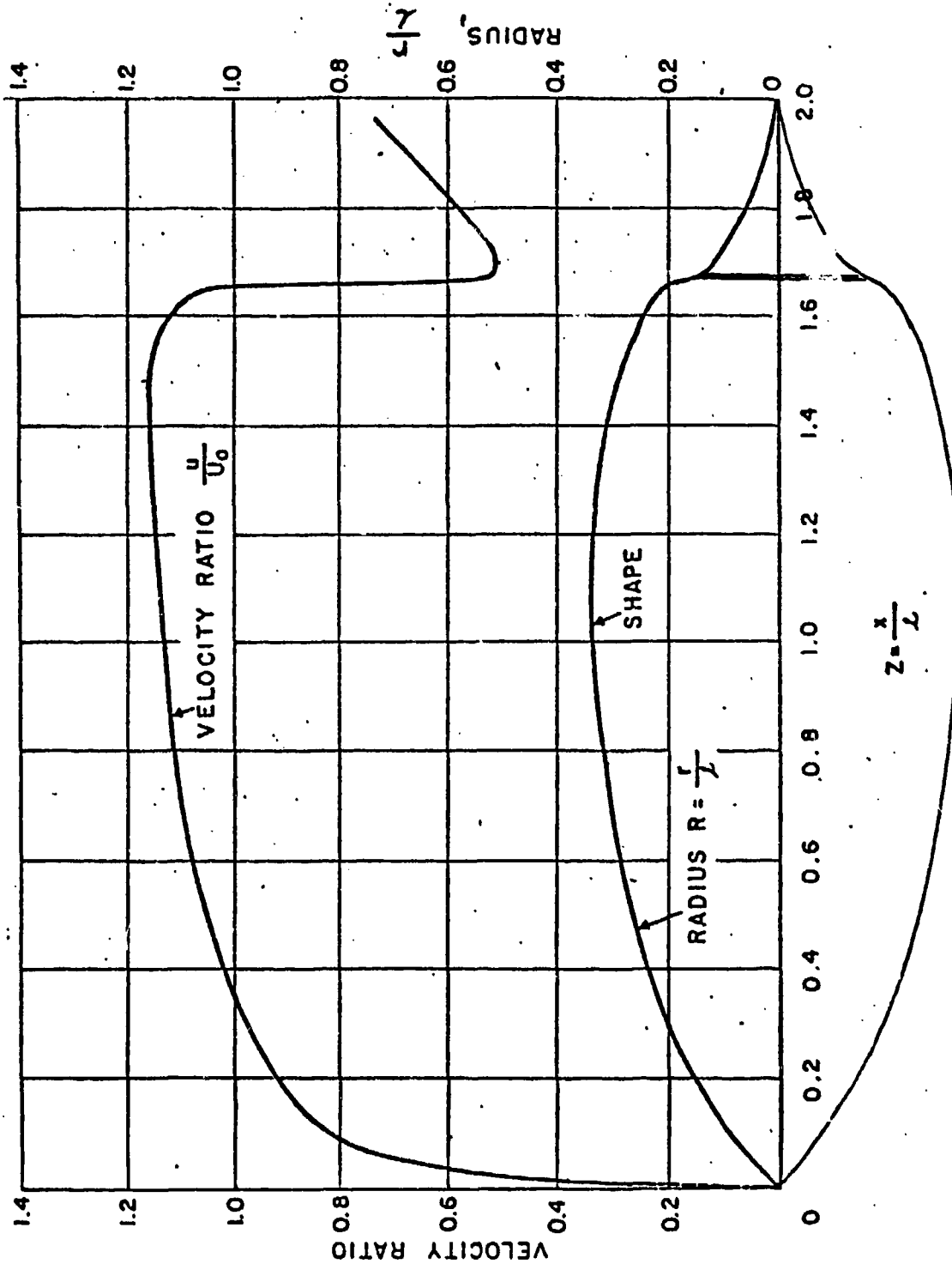


Figure 39. Thirty-four Percent Thick Lighthill Airfoil.  
Body and Velocity Distribution.

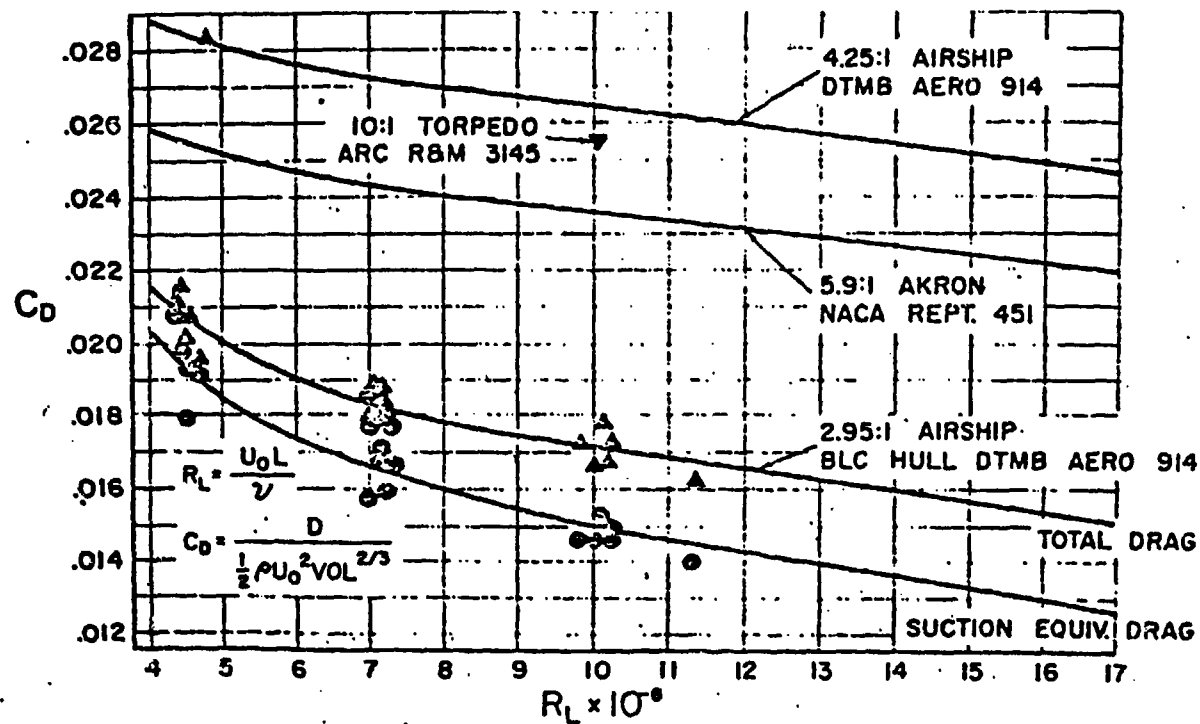


Figure 40. Experimentally Determined Bare Hull Drag.

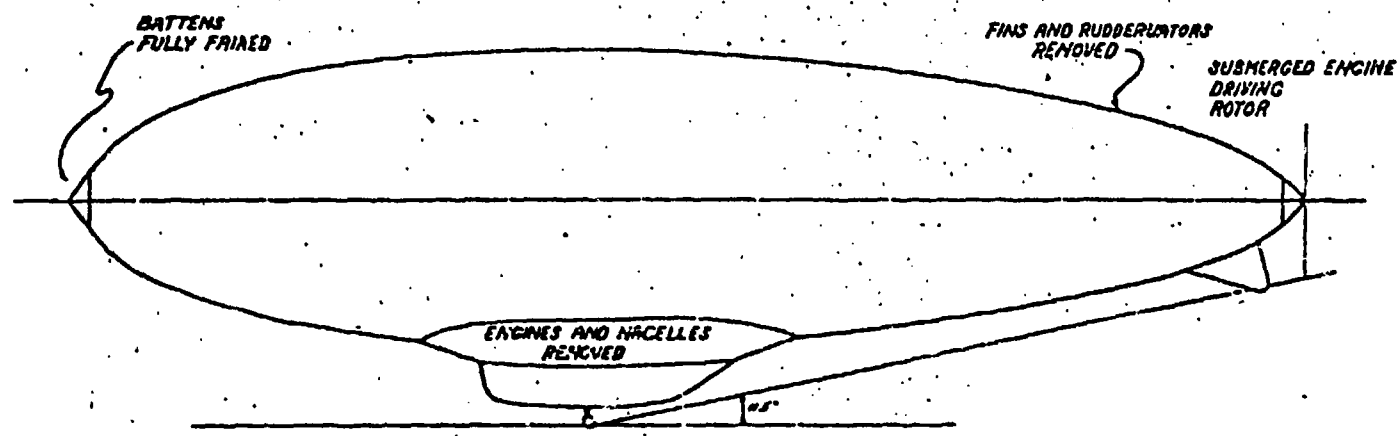


Figure 41. Stern Propelled Airship.

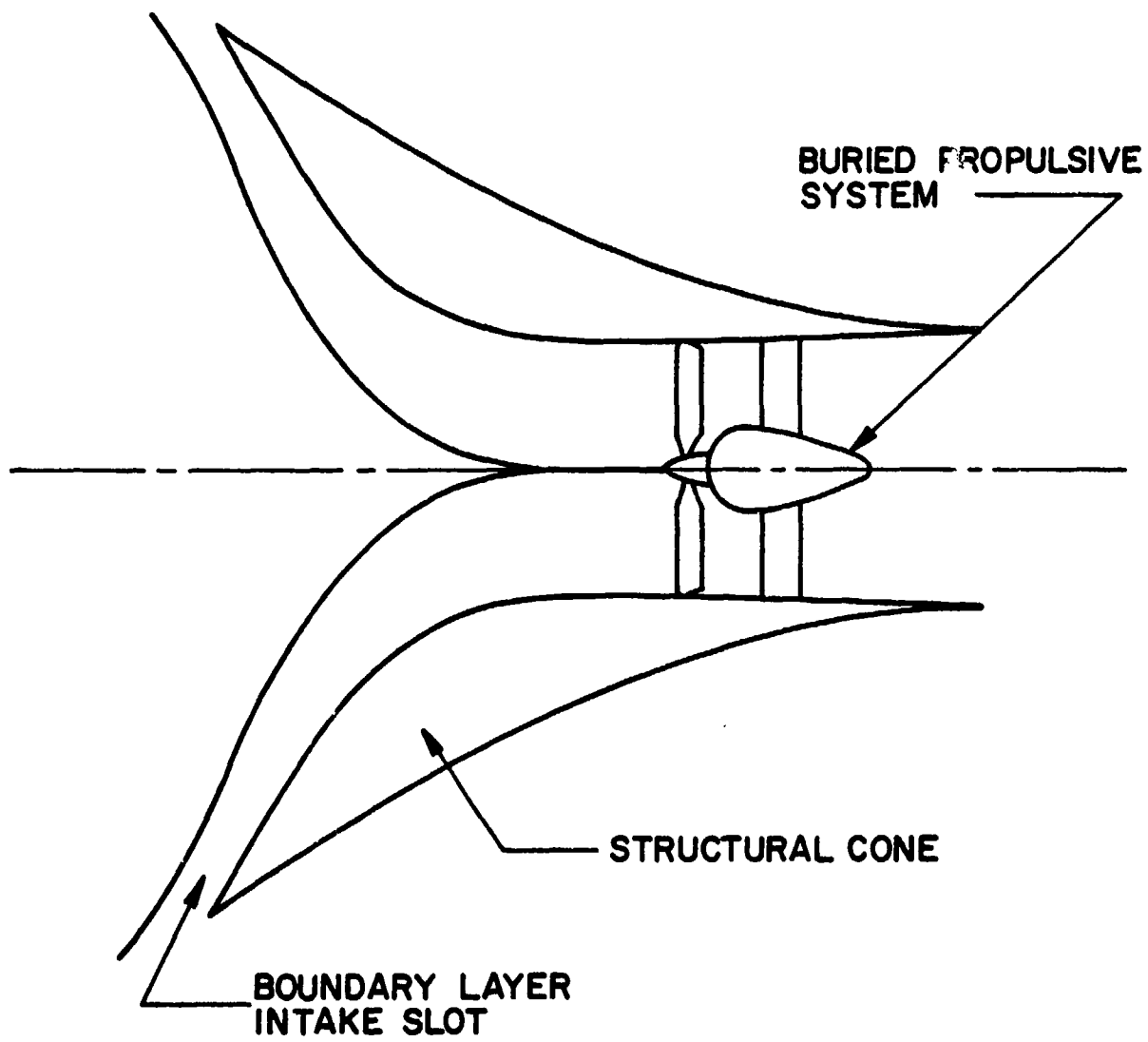


Figure 42. Schematic of BLC Airship Propulsion System.

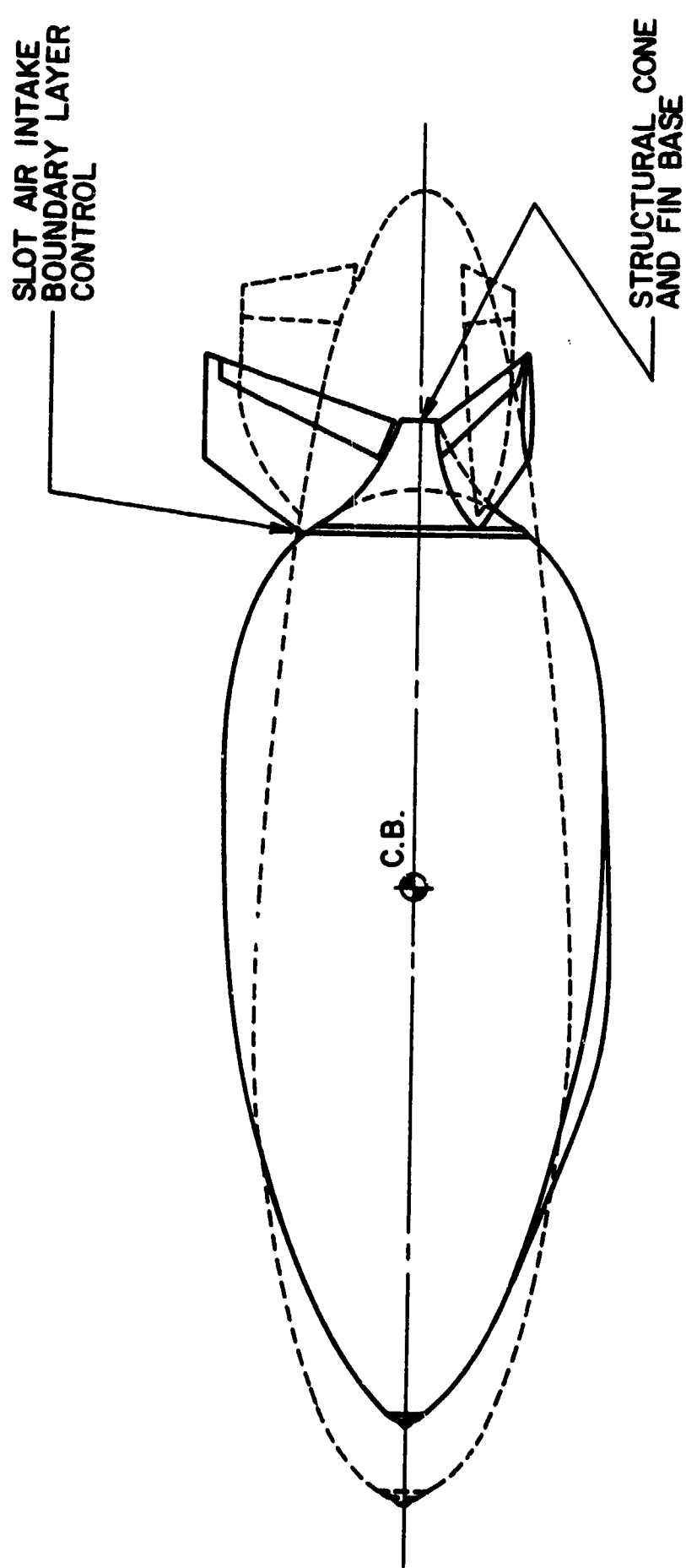
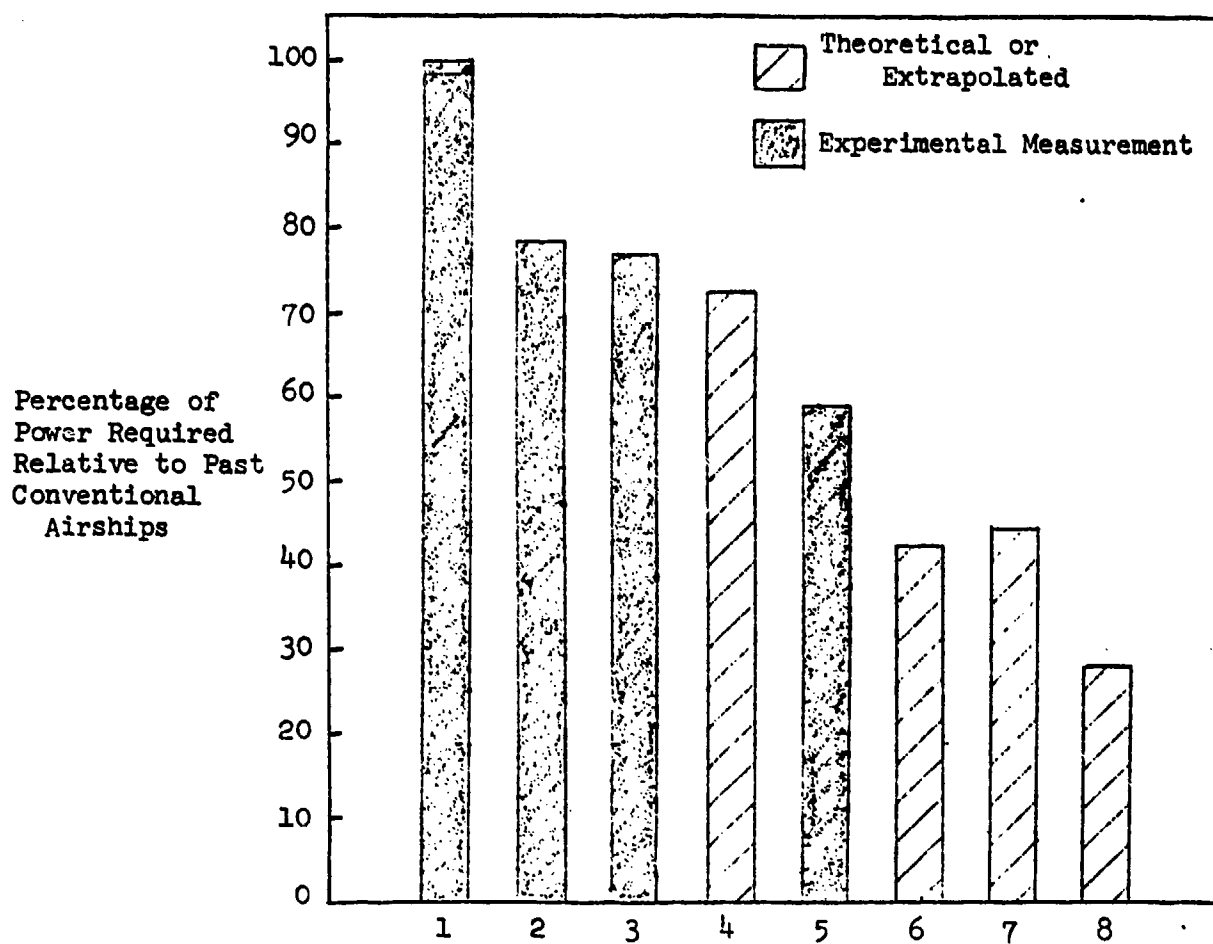


Figure 43. Comparison of BLC Airship with Conventional for Equal Volume.



1. Conventional - McLemore (Wind Tunnel)  
Carreta (Wind Tunnel)  
Cornish and Boatwright (Full Scale)
2. Conventional Airship - Cornish and Boatwright (Full Scale)  
Drag Cleanup
3. Hull BLC - Carreta (Wind Tunnel)
4. BLC with Propulsion Integration (conservative) - Goodyear Study
5. Stern Drive (First Generation) - McLemore (Wind Tunnel)
6. Stern Drive (Second Generation) - McLemore  
Cornish and Boatwright
7. Hull/BLC/Propulsion Integration (First Generation) - Goldschmied
8. Hull/BLC/Propulsion Integration (Second Generation) - Goldschmied

Figure 44 Possible Reductions in the Power Requirements of Airships.

### STABILITY AND CONTROL

This section considers some basic aspects of precision control of Lighter-Than-Air Vehicles in hovering flight. Two aspects of LTA vehicles make it difficult to directly apply existing hovering handling qualities criteria such as are found in the Helicopter Handling Qualities Specifications (MIL 850LA). The large size of LTA vehicles is one aspect which raises the controversial issue of the effect of size on handling qualities. MIL 850L essentially incorporates the effect of size or gross weight on handling qualities in a manner that is consistent with the physical changes which occur as vehicles are made larger, and is not based on trends which have been verified by experiment. The second aspect relates to the control methods to be employed on the vehicle. It appears unlikely that precision hovering would be accomplished by tilting the vehicle to obtain lateral or longitudinal translation as is the case for a helicopter but rather by direct translational force control.

The most relevant studies related to both of these issues are the studies made in connection with the Heavy-Lift-Helicopter (HLH) program. The results of the HLH study reported in Reference 73 indicate that if the specification on precision hovering is to be able to maintain a position within a one foot square then a translational force control must be employed and in addition a ground referenced position feedback is required. This latter conclusion implies that in addition to provision for translational force controls elaborate sensing equipment must be installed in the vehicle in order to obtain a ground referenced displacement measurement.

This section examines some of these questions using typical Lighter-Than-Air Vehicle Parameters. Attention is concentrated on translational force

control, and obtaining order of magnitude estimates of the problem.

One other aspect of the control of Lighter-Than-Air Vehicles must be considered if concepts such as the Heli-Stat are examined. That is the question of control in hovering with zero payload, that is, under circumstances in which the trim thrust of the control rotors is zero. This problem arises because of the non-linear variation of propeller/rotor thrust with blade angle in the vicinity of zero thrust in hovering flight. This problem was experienced on two VTOL aircraft built some years ago (VS-2, XC-142). Aircraft pitch control was obtained by a tail rotor operating at nominally zero thrust in the trim condition. About this equilibrium condition, the propeller thrust essentially varies as the square of the blade pitch angle and consequently a very low gradient of thrust variation with pitch angle is obtained. This feature of the control system design must be examined in detail.

Three problems associated with station keeping in hovering flight are examined in the following. First the power required to keep station in steady winds is estimated for a cross-wind hovering situation with the vehicle hull oriented perpendicular to the wind. Then the control system requirement for keeping station in gusts is examined, first for an automatic control system and then for a human operator. Translational motions are examined and also the level of roll coupling is considered.

#### 1.) Keeping Station in a Steady Wind

First the problem of maintaining station in a steady wind is examined in order to obtain some estimate of the installed power requirements. The most critical case is clearly the requirement that the LTA vehicle be able

to maintain station oriented with the long axis of the hull perpendicular to the wind. Figure 45 shows the thrust required to counter the lateral drag force acting on the hull as a function of wind velocity for two hulls, one characteristic of the Akron ( $V = 6,500,000$  cubic feet) and a somewhat smaller hull ( $V = 2,900,000$  cubic feet). The lateral force is based on an estimated drag coefficient of the hull based on a planform equal to 0.6. In addition, this curve shows the horsepower required for propellers producing thrust to counter lateral force arising from the steady wind velocity. The horsepower required is based on the following equations.

$$T = 2\rho A_p (V + v) v$$

$$P = \frac{T(V + v)}{\eta_p}$$

For simplicity, the propeller profile power is accounted for by an efficiency  $\eta_p$ . A propeller efficiency of 75% was assumed. The calculations indicate that for the Akron, to keep station in a 30 knot wind with eight fifteen foot diameter propellers, 60,000 H, would be required. The installed horsepower of the Akron was 4,400 H, that required to cruise at 75 knots. As a further comparison also shown in the power required to lift a 140 ton payload with four helicopter rotors of 42 foot radius each. This requires 35,000 H which could also be used to counter a lateral sustained wing of 24 knots. Note the very large magnitude of the lateral force generated by a 24 knot wind, equal to approximately one quarter of the gross weight of the Akron (400,000 lbs) without payload. These numbers indicate that any station keeping requirement with the additional requirement that the airship must be maintained perpendicular to the wind will tend to size

the installed power. Similar numbers are shown for the smaller vehicle, i.e., 16,000<sup>H</sup> is required to lift a 75 ton payload with four 36 foot diameter rotors and 26,000 horsepower is required to keep station in a steady 30 knot wind. Owing to the large thrusts required and the low velocities, all of these power computations involve a sizeable induced power. This is shown by the additional curves of power based on thrust times velocity. Thus selection of propeller diameter will have an important impact on power required.

Recall also that if the control rotors countering the lateral gusts are not located at the drag center of the vehicle then there must be additional compensation for the moments produced.

These numbers indicate that requirements for hovering in moderate winds may determine the installed power of the vehicle.

2.) Keeping Station in Gusts

The problem of maintaining a position in gusts is now examined. First the problem is examined with a translational force control and an ideal control system providing velocity and position control. The critical case is of course when lateral gusts are encountered. Then the rolling motion caused by this control system is examined. Then the case of operator control is examined.

The equations of motion of the airship are assumed to arise only from the hull. The side force equation in hovering flight can be written as

$$M' \ddot{y} - \frac{\partial Y}{\partial v} \dot{y} = \frac{\partial Y}{\partial \delta} \delta - \frac{\partial Y}{\partial v} v_g$$

where  $y$  is the position of the vehicle with respect to some point on the ground. The feedback law for an ideal control system is

$$\delta = -K_v y - K_v \dot{y}$$

Where it is assumed that suitable sensors can be provided to measure accurately the position and velocity of the airship with respect to the desired reference position. Substituting the control law and dividing by the inertia term and using the following notation

$$Y_v = \frac{1}{M'} \frac{\partial Y}{\partial v}$$

$$Y_\delta = \frac{1}{M'} \frac{\partial Y}{\partial \delta}$$

$$2\zeta\omega_N = Y_v + K_v Y_\delta$$

$$\omega_N = K_v Y_\delta$$

$$\ddot{y} + 2\zeta\omega_N \dot{y} + \omega_N^2 y = -Y_v v_g$$

Taking the Laplace transform, the transfer function of the vehicle describing the lateral position response to lateral gust velocity is

$$\frac{Y(s)}{V_g(s)} = \frac{-Y}{s^2 + 2\zeta\omega_N s + \omega_N^2}$$

Now we wish to determine the mean square value of the position response to a typical gust power spectrum.

A reasonable model for the power spectrum of horizontal gusts at low wind velocities can be obtained by passing white noise through a low pass filter<sup>74,75</sup>.

The power spectrum of a gust with a mean square gust velocity  $\tilde{U}_g^2$  is given by

$$G_g(\omega) = \frac{2}{\omega_c} \left( \frac{\tilde{U}_g^2}{1 + (\frac{\omega}{\omega_c})^2} \right)$$

where  $\omega_c$  is the cut-off frequency of the low pass filter and is usually assumed to be 0.314 rad/sec as a reasonable match to experimental data on gust spectra<sup>75</sup>.

The power spectrum of the lateral displacement can then be calculated from the transfer function given above.

$$G_y(\omega) = |\Phi|^2 G_g(\omega)$$

where  $\Phi$  is the transfer function. The mean square value of the displacement of the vehicle can then be calculated from<sup>76</sup>

$$\tilde{y}^2 = \frac{1}{2\pi} \int_{-\infty}^{\infty} G_y(\omega) d\omega$$

This calculation can be conveniently made using the integral tables of Reference 76. The result is

$$\tilde{y}^2 = \frac{1}{2} \frac{\tilde{U}^2}{\tau_v^2 \omega_N^4} \left\{ \frac{1}{\zeta} \left( \frac{\omega_N}{\omega_c} \right) \frac{1 + 2\zeta \frac{\omega_N}{\omega_c}}{1 + 2\zeta \frac{\omega_N}{\omega_c} + \left( \frac{\omega_N}{\omega_c} \right)^2} \right\}$$

where  $\tau_v$  is the vehicle time constant in response to a gust, i.e.,

$$\tau_v = \frac{M'}{\frac{\partial Y}{\partial v}}$$

Assuming that the side force varies as the square of the velocity and that the mass of the vehicle including the apparent mass of the vehicle is twice the displaced mass

$$\tau_v = \frac{D}{U_0 C_d}$$

where D is the diameter of the hull,  $U_0$  is the mean wind velocity and  $C_d$  is the drag coefficient of the hull. For a 15 knot mean wind and a diameter of 150 feet and a drag coefficient of 0.6,  $\tau_v$  is 10 seconds.

Note that this is quite a short time constant in a sense for such a large vehicle owing to its very large drag coefficient. Figure 46 shows the dependence of the root mean square value of the displacement on the closed loop vehicle natural frequency and damping ratio for a gust with a root mean square velocity of 5 ft per second. The requirement for a tight control loop can be clearly seen if the RMS displacement is to be held within one foot. Note that we are considering a very large vehicle so that the required closed loop frequency of 1 radian per second implies a high gain control system. This required frequency is similar to that of the HLM positioning system described in Reference 73, which resulted in an RMS displacement of a few inches when flight tested. It should be noted that for this precise positioning, sensing of displacement

and velocity with respect to ground position was required and the vehicle was automatically flown. Data taken with the pilot in control of the helicopter and the conventional automatic stabilization system operating indicated an RMS displacement of 4 feet. These two values are indicated on Figure 46 for reference.

Some appreciation of the magnitude of the control can be seen by noting that

$$\omega_N^2 = 1 \frac{\text{Rad}^2}{\text{Sec}^2} = \frac{K_0}{M'} \frac{\partial Y}{\partial \delta} \frac{\text{Ft./Sec}^2}{\text{Ft.}}$$

may be interpreted as a gain that produces an acceleration of  $1 \text{ ft/sec}^2$  per foot, i.e., for the Akron with a gross weight of 400,000 lbs and an apparent mass equal to this value, the control must produce 25,000 pounds of force per foot of displacement to produce this frequency. The lower natural frequency of  $0.5/\text{rad/sec}$  reduces this requirement by a factor of four and approximately increases the RMS displacement by that same factor. As the position requirements are relaxed the requirements on the control system become considerably less severe. As seen in Figure 46 if the requirement is relaxed to 50 feet then a natural frequency  $\omega_N = 0.05 \text{ rad/sec}$  is satisfactory and it is not necessary to augment the natural damping of the vehicle. As shown below it appears quite possible that this level of position accuracy could be achieved by a human operator as well, eliminating the need for ground position feedback, a considerable simplification in the sensing equipment required.

It is important to note that this analysis contains a number of simplifications. It has been assumed that owing to the low drag coefficient of the hull in the longitudinal direction that there will be no

appreciable motion longitudinally as a result of gusts. Vertical motion is also neglected as well as yawing motion. The attempt here was to obtain an order of magnitude estimate of the problem rather than to obtain precise results.

#### Roll Coupling

Since, in general, it will not be practical to locate the translational force control at the center of drag of the vehicle, the question of roll motion associated with this control is now examined. A fully buoyant vehicle is considered so that there is no translational force produced by rolling and therefore, the RMS displacement is not affected.

The rolling moment equation is given by

$$I' \ddot{\phi} + wh \phi = h \left\{ \frac{\partial Y}{\partial v} (\dot{y} - v_g) \right\} - h_c \frac{\partial Y}{\partial \delta} \delta$$

where  $h$  is the distance between the center of gravity and the center of buoyancy and  $h_c$  is the distance the control is located below the center of gravity. This equation can be written after taking the Laplace transform and introducing some definitions as

$$(s^2 + \omega_\phi^2) \phi(s) = \frac{hM'}{I'} \left\{ \frac{s^2 + K_v Y_s (1 + \frac{h_c}{h}) s + K_\theta Y_\delta (1 + \frac{h_c}{h})}{s^2 + [-Y_v + K_v Y_\delta] s + K_\theta Y_\delta} \right\} \{-v_g(s)\}$$

The nature of the input disturbance to the roll motion as a function of control location,  $h_c$  is then shown in Figure 47. If the control is located at the center of gravity of the vehicle ( $h_c = 0$ ) then the input is essentially the gust input, i.e., the control system has no effect on the roll motion. If the control is located at the center of drag (center of buoyancy) then

the low frequency input is markedly reduced. If the control is located at an equal distance below the center of gravity the low frequency disturbances are markedly amplified by the control system. Above the natural frequency of the translational control system there is little effect from control placement.

#### OPERATOR CONTROL

In order to gain some further insight into the station keeping problem we now consider the problem of translational station keeping with a human operator. A simplified model of the operator is employed. In this case it is assumed that the vehicle has no automatic control system and that the operator applies control proportional to position from a desired position and that his control action is characterized by a first order lag. The equation of motion is

$$\ddot{y} - Y_v \dot{y} - \frac{v}{\tau_o} \delta = Y_v v_g$$

The operator's action is characterized by

$$\tau_o \dot{\delta} + \delta = - K_o y$$

The characteristic equation of this dynamic system comprised of the vehicle and operator is in Laplace notation

$$\tau_o [s(s + \frac{1}{\tau_o})(s + \frac{1}{\tau_v})] + X_o K_o = 0$$

Since this is a third order system, there can be a stability problem with this loop depending upon the time lag of the operator  $\tau_o$  and his gain  $K_o$ . A root locus is shown in Figure 48 for the dynamics of this system as a

function of gain  $K_o$ . The time lag of the operator  $\tau_o$  is assumed to be considerably shorter than the vehicle time constant,  $\tau_v$ , which was shown earlier to be the order of 10 seconds. Neutral stability occurs at a closed loop frequency

$$\omega_o = \frac{1}{\sqrt{\tau_o \tau_v}}$$

And it may be shown that if the operator lag is considerably shorter than the vehicle lag, the closed loop system damping is

$$2\zeta\omega_n \approx \frac{\tau_o \tau_v}{\tau_o + \tau_v} \left\{ \frac{1}{\tau_o \tau_v} - \omega_n^2 \right\}$$

and the natural frequency of the system is

$$\omega_n^2 \approx X_8 K_o \left\{ \frac{\tau_v}{\tau_o + \tau_v} \right\}$$

Notice that the closed loop bandwidth is severely limited for any appreciable operator lag. If the operator lag is 0.1 seconds, then neutral stability occurs at  $\omega_n = 1$  rad/sec the level that was found desirable for tight control in the automatic case, unless the basic vehicle damping is augmented. Recall that augmenting the vehicle damping requires sensing the velocity of the vehicle with respect to the ground.

In order to obtain a quantitative estimate of the implications of these results it is assumed that the operator will produce a closed loop natural frequency which is some fraction  $f$  of the stability boundary. Thus the natural frequency is

$$\omega_n^2 \approx \frac{f^2}{\tau_o \tau_v}$$

and the damping ratio is

$$2\zeta\omega_N = \frac{1 - f^2}{\tau_o + \tau_v}$$

The closed loop system transfer function is

$$\frac{y(s)}{v_g(s)} = \frac{-Y_v(\tau_o s + 1)}{\tau_o[s^3 + (\frac{1}{\tau_o} + \frac{1}{\tau_v})s^2 + \frac{1}{\tau_o \tau_v}s + \frac{\omega_N^2}{\tau_o}]}$$

If the operator time constant,  $\tau_o$ , is relatively short compared to the vehicle time constant,  $\tau_v$ , this transfer function can be approximated by

$$\frac{y(s)}{v_g(s)} \approx \frac{-Y_v}{s^2 + 2\zeta\omega_N s + \omega_N^2}$$

where the natural frequency and damping ratio are given above. This transfer function is now of the same form as the automatic control case and the mean square value of the displacement arising from gust disturbances can be expressed as

$$\tilde{y}^2 \approx \frac{\tilde{U}_g^2}{\tau_v^2 \omega_c} \left\{ \frac{(\tau_o + \tau_v)(\tau_o \tau_v)}{(1 - f^2) f^2} \right\} \left\{ \frac{1 + \frac{1}{\omega_c} \left( \frac{1 - f^2}{\tau_o + \tau_v} \right)}{1 + \frac{1}{\omega_c} \left( \frac{1 - f^2}{\tau_o + \tau_v} \right) + \frac{1}{\omega_c^2} \frac{f^2}{\tau_o \tau_v}} \right\}$$

Again taking the gust cut-off frequency  $\omega_c = 0.314$  rad/sec and the vehicle time constant  $\tau_v = 10$  sec, the RMS displacement can be calculated from this expression. The RMS displacement as a function of operator bandwidth  $f$  and lag  $\tau_o$  is shown in Figure 49. The value of  $f = 0.75$  is approximately the minimum displacement that can be achieved, again showing the importance of a high bandwidth. To obtain precise hovering a short operator lag is required. In general, it appears that the operator must supply lead to achieve precise position control, hovering in gusts.

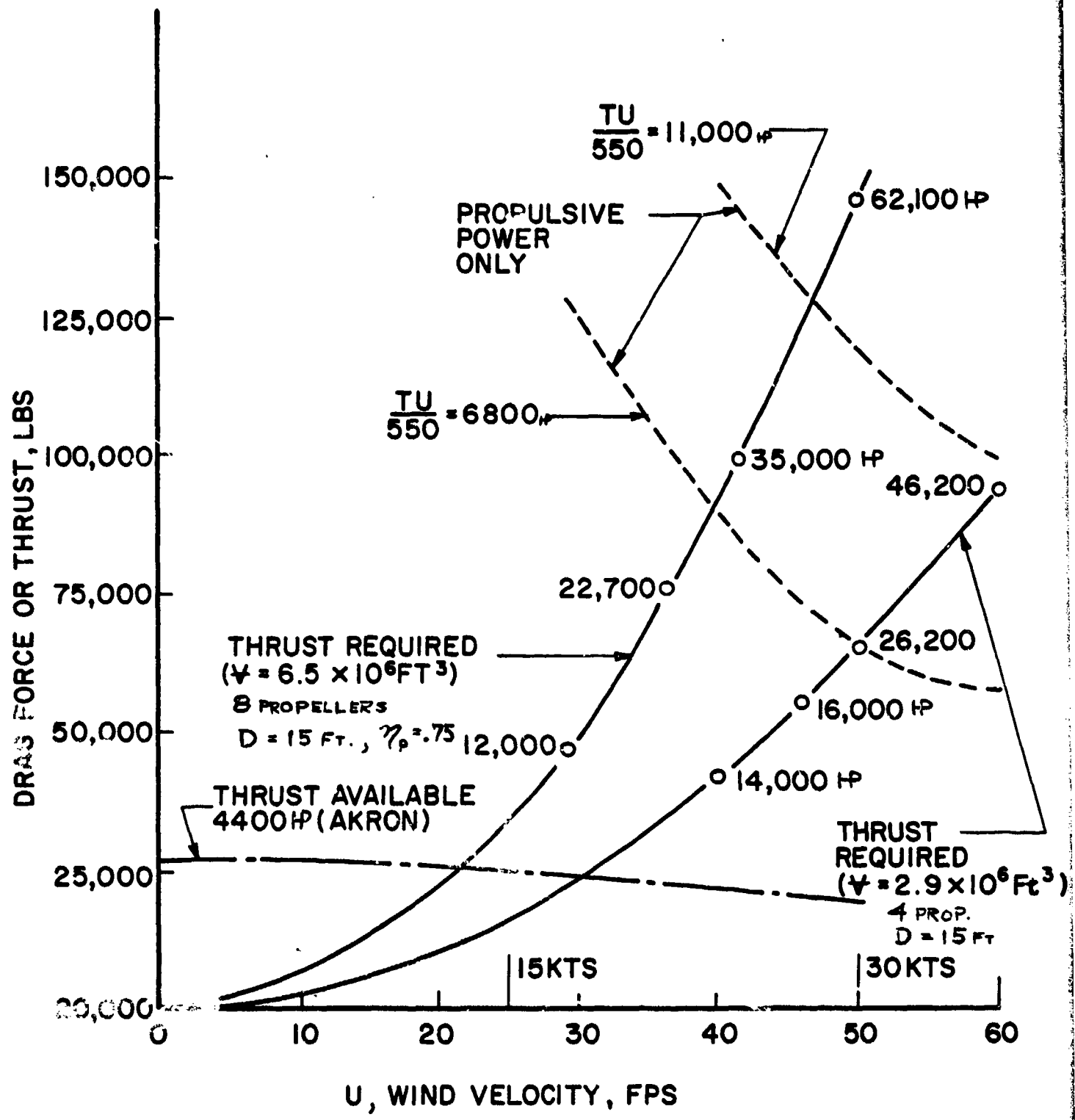


FIGURE 45. Lateral Drag and Propeller Horsepower Required to Balance Lateral Drag at Zero Forward Speed for Various Wind Velocities

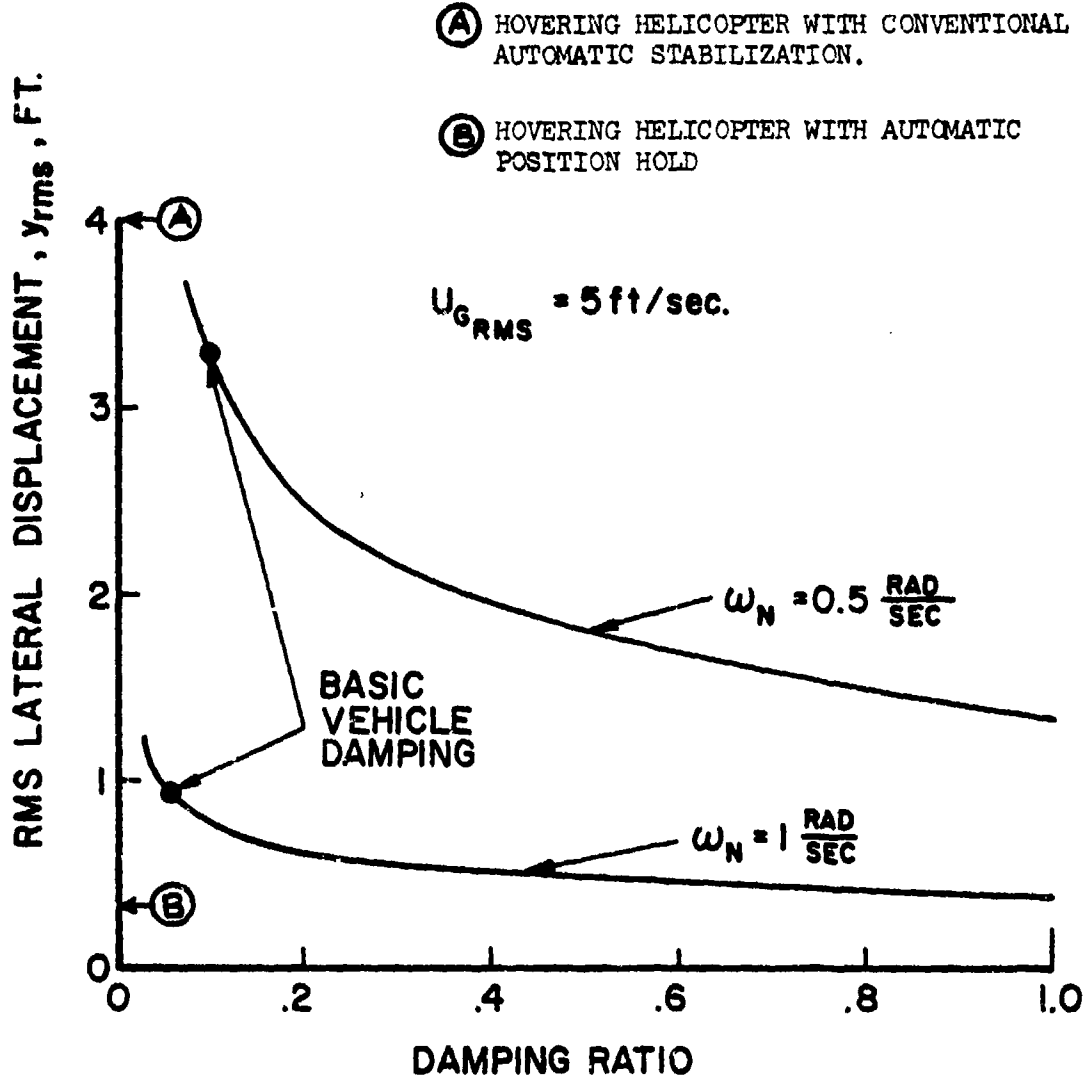


Figure 46. RMS Lateral Displacement as a Function of Closed Loop Vehicle Damping Ratio and Natural Frequency.

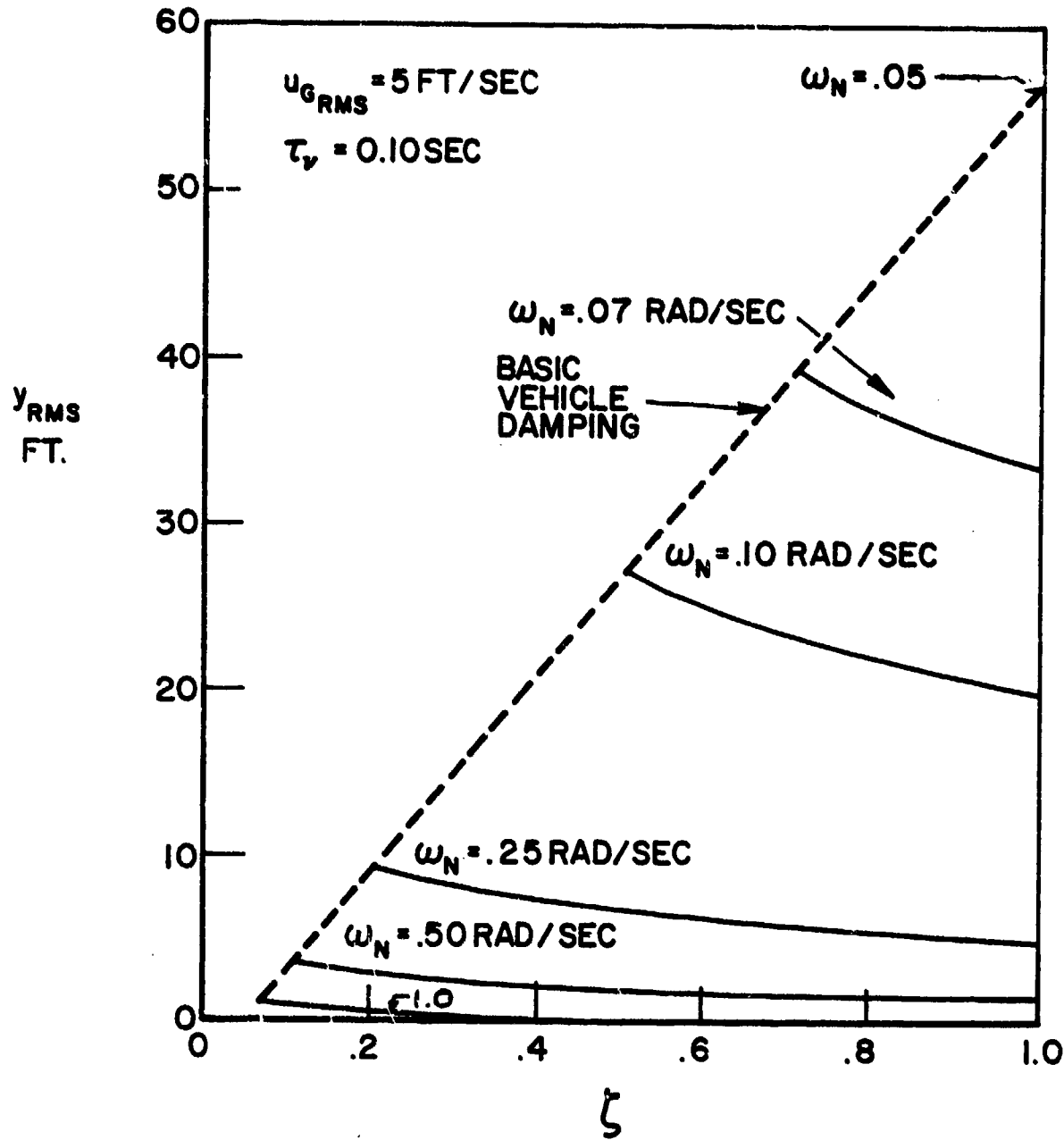


FIGURE 46. RMS Lateral Displacement as a Function of Closed Loop Vehicle Damping Ratio and Natural Frequency  
(continued)

RATIO OF ROLL DISTURBANCE  
WITH TRANSLATIONAL CONTROL  
ROLL DISTURBANCE OF BASIC  
VEHICLE

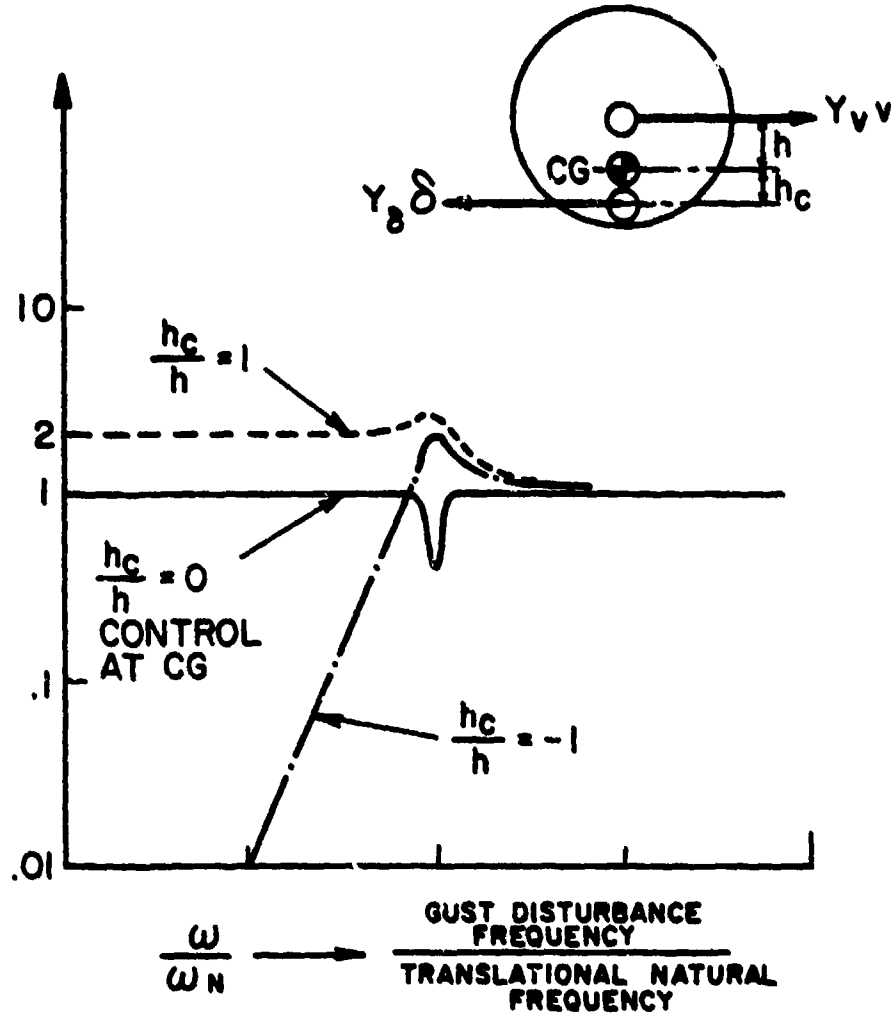


FIGURE 47. Level of Roll Disturbance Caused by Gusts and Translational Control System

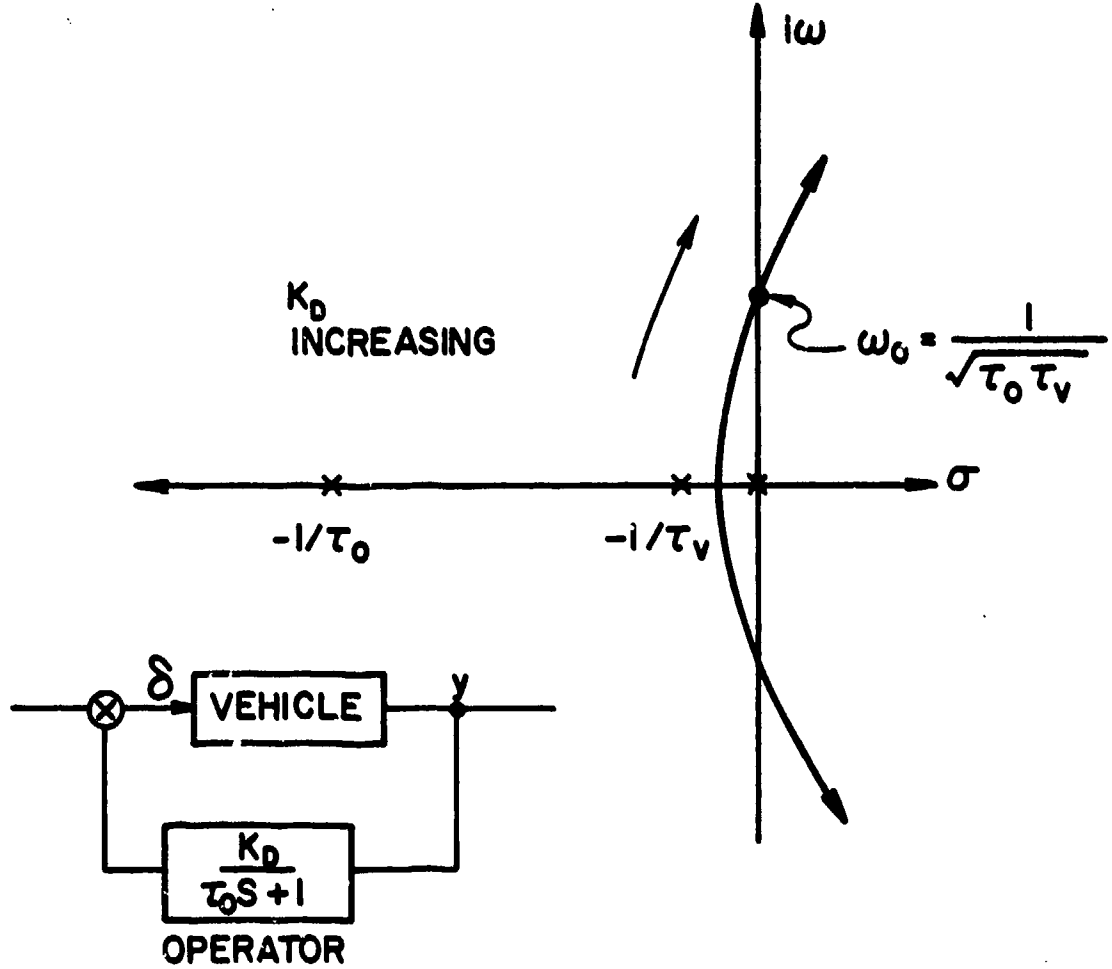


FIGURE 48. Closed Loop Dynamics, Translational Control by Human Operator; Position Feedback with Lag  $\tau_0$

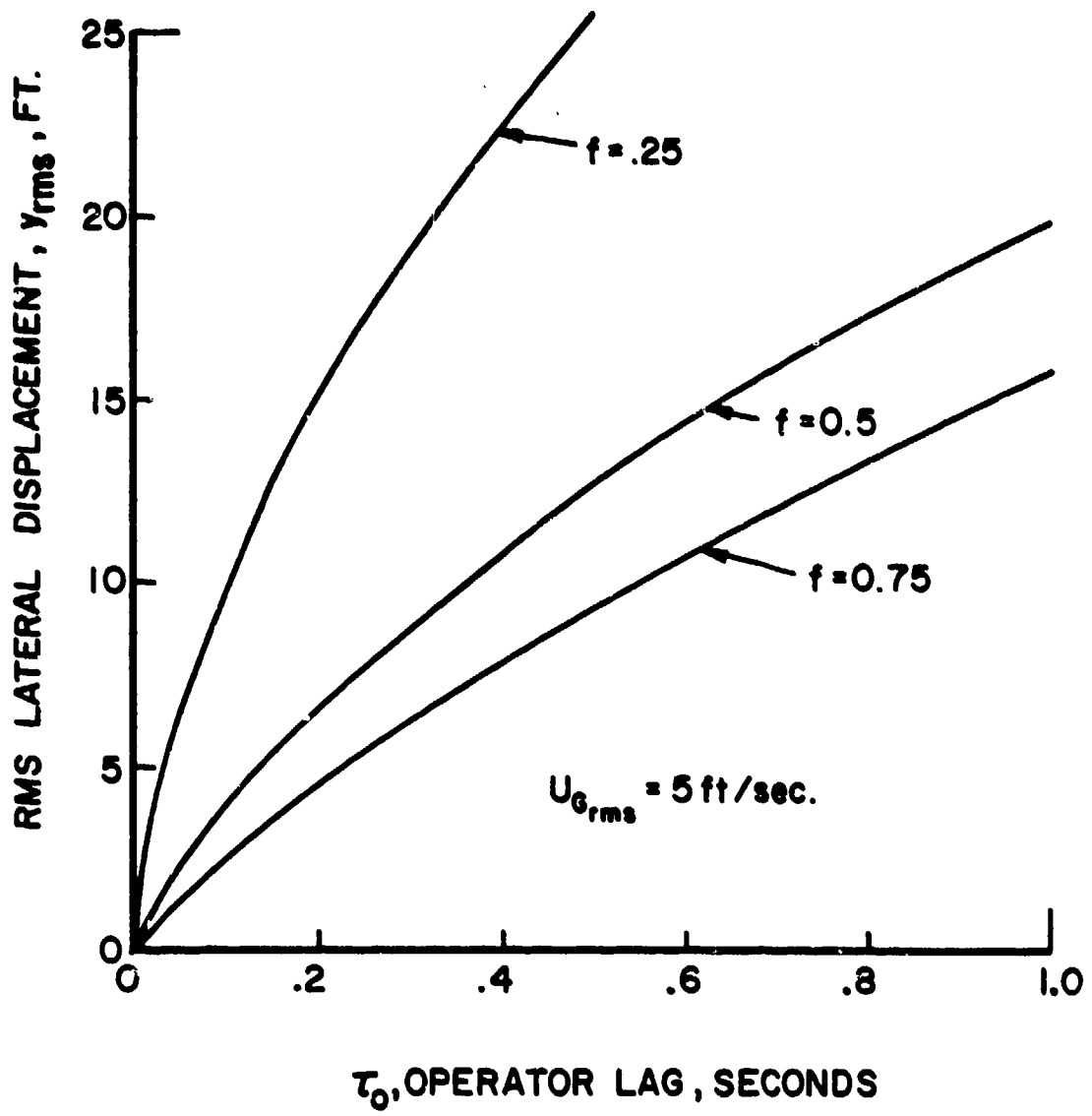


Figure 49. RMS Displacement in Gusts with Human Operator Control; Displacement Feedback with Lag.

### BIBLIOGRAPHY

1. Munk, M. M.: "The Aerodynamic Forces on Airship Hulls", NACA Report 184, 1924.
2. Milne-Thompson: THEORETICAL HYDRODYNAMICS, MacMillan, 1955.
3. Kochin, N. E., Kibel, I. A. and Rose, N. W.: "Theoretical Hydro-mechanics", Interscience 1964.
4. Lamb, H.: HYDRODYNAMICS, Dover Publications, New York, 1945.
5. Nielsen, J. N.: MISSILE AERODYNAMICS, McGraw-Hill Book Company, Inc., New York, 1960.
6. Prandtl, L.: FLUID DYNAMICS, Hafner Publishing Co., 1952.
7. Bisplinghoff, R. L., Ashley, H. and Halfman, R.: AEROELASTICITY, Addison-Wesley, 1955.
8. Liu, D. D. and Platzer, M. F.: "On the Calculation of Static and Dynamic Stability Derivatives for Bodies of Revolution at Subsonic and Transonic Speeds", AIAA Paper No. 70-190, January 1970.
9. Revell, J. D.: "Second-Order Theory for Steady or Unsteady Subsonic Flow Past Slender Lifting Bodies of Finite Thickness", AIAA Journal, Vol. 7, No. 6, pp. 1070-1079, 1968.
10. von Karman, Th.: "Some Aerodynamic Problems of Airships", Guggenheim Institute Proceedings.
11. Thwaites, B.: INCOMPRESSIBLE AERODYNAMICS, Oxford University Press, Oxford, England, 1960.
12. Upson, R. H., Klikoff, W. A.: "Application of Practical Hydrodynamics of Airship Design", NACA Report 405.
13. Jones, R.: "The Distribution of Pressure on a Prolate Spheroid", ARC R&M 1961, 1925.
14. Jones, R.: HIGH SPEED WING THEORY, Princeton University Press, Princeton N. J., 1960.
15. Peake, D. J., Rainbird, W. J. and Atraghi, E. G.: "Three-Dimensional Flow Separations on Aircraft and Missiles", AIAA Journal, Vol. 10, No. 5, pp. 567-580, May 1972.
16. Wang, K. C.: "Separation Patterns on Inclined Bodies of Revolution", AIAA Journal, Vol. 10, No. 8, pp. 1044-1050, August 1972.

17. Allen, H. J.: "Estimation of the Forces and Moments Acting on Inclined Bodies of Revolution of High Fineness Ratio", NACA RM A9126, 1949.
18. Allen, H. J. and Perkins, E. W.: "A Study of Effects of Viscosity on Flow Over Slender Inclined Bodies of Revolution", NACA Report 1048, 1951.
19. Hopkins, E. J.: "A Semi-Empirical Method for Calculating the Pitching Moment of Bodies of Revolution at Low Mach Number", NACA RM A51C14, 1951.
20. Jorgensen, L. H.: "Prediction of Static Aerodynamic Characteristics for Space-Shuttle-Like and Other Bodies at Angles-of-Attack From 0° to 180°", NASA TN D-6996, 1973.
21. Marshall, F. J. and Deffenbaugh, F. D.: "Separated Flow Over a Body of Revolution", Journal of Aircraft, Vol. 12, No. 2, pp. 78-85, February 1975.
22. Multhopp, H.: "Aerodynamics of the Fuselage", NACA TM No. 1036, 1942.
23. Hoerner, S. F.: FLUID-DYNAMIC DRAG, Published by Author, New Jersey, 1965.
24. Young, A. D.: "The Calculation of the Total and Skin Friction Drags of Bodies of Revolution at Zero Incidence", ARC R&M No. 1874, 1939.
25. Heaslet, M. A. and Nitzberg, G. E.: "The Calculation of Drag For Airfoil Sections and Bodies of Revolution at Subcritical Speeds", NACA RM A7B06, 1947.
26. Granville, P. S.: "The Calculation of the Viscous Drag of Bodies of Revolution", David Taylor Model Basin Report 849, 1953.
27. Cebeci, T., Musinskis, G. J. and Smith, A. M. O.: "Calculation of Viscous Drag of Two-Dimensional and Axisymmetric Bodies in Incompressible Flows", AIAA Paper No. 72-1, 1972.
28. Nakayama, A. and Patel, V. C.: "Calculation of the Viscous Resistance of Bodies of Revolution", Journal of Hydraulics, Vol. 8, No. 4, pp. 154-162, October 1974.
29. Myring, D. F.: "A Theoretical Study of Body Drag in Subcritical Axisymmetric Flow", The Aeronautical Quarterly, Vol. XXVII, Part 3, pp. 186-194, August 1976.
30. Kaplan, C.: "Potential Flow About Elongated Bodies of Revolution", NACA Report No. 516, 1935.

31. Hess, J. L. and Smith, A. M. O.: "Calculation of the Non-Lifting Potential Flow About Arbitrary Three-Dimensional Bodies", Douglas Aircraft Division Report No. E.S. 40622, March 1962.
32. Hess, J. L. and Smith, A. M. O.: "Calculation of Potential Flow About Arbitrary Body Shapes", Douglas Paper-1700, September 1963.
33. Cebeci, T., Mosinskis, G. J. and Smith, A. M. O.: "Calculation of Separation Points in Incompressible Turbulent Flow", Journal of Aircraft, Vol. 9, No. 9, pp. 618-624, September 1972.
34. Geissler, W.: "Three-Dimensional Laminar Boundary Layer Over a Body of Revolution at Incidence and With Separation", AIAA Journal, Vol. 12, No. 12, pp. 1743-1745, December 1974.
35. Miles, J. W.: THE POTENTIAL THEORY OF UNSTEADY SUPERSONIC FLOW, Cambridge University Press,
36. Robinson, M. L.: "The Estimation of Pitch Damping Derivative of Missile Configurations at Subsonic Speeds", AIAA Paper 70-537
37. Jones, R. and Bell, A. H.: "Experimental on a Model of the Airship R 101", ARC R&M 1168, September 1926.
38. Johnes, R.: "The Distribution of Normal Pressures on a Prolate Spheroid", ARC R&M 1061, December 1925.
39. Gourjienko, G. A.: "Method of Curved Models and Its Application to the Study of Curvilinear Flight of Airships", NACA TM's 829, 830
40. Smith, R. H.: "Curvilinear Dynamics of Airships Based on Bowed Model Tests", Proceedings of the Fifth International Congress for Applied Mechanics, MIT, September 12-16, 1938.
41. Pannell, J. R. and Jones, R.: "Experiments on a Model of an Airship of the 23 Class", ARC R&M 456, July 1918.
42. Pannell, J. R. and Jones, R.: "Stability and Resistance Experiments on a Model of Vickers Rigid Airship R.80", ARC R&M No. 541, August 1918.
43. Zam, A. F., Smith, R. H. and Louden, F. A.: "Air Forces, Moments and Damping on Model of Fleet Airship Shenandoah", NACA TR 215, 1925.
44. Flax, A. H., and Lawrence, H. R.: "The Aerodynamics of Low Aspect Ratio Wings and Wing-Body Combinations", Cornell Aeronautical Laboratory Report No. CAL-37, 1951.

45. Ribner, H. S.: "The Stability Derivatives of Low-Aspect-Ratio Triangular Wings of Subsonic and Supersonic Speeds", NACA Technical Report Note No. 1423, 1947.
46. Weissenger, J.: "The Lift Distribution of Sweptback Wings", NACA TM 1120, 1947.
47. Lawrence, H. F.: "The Lift Distribution on Low Aspect Ratio Wings at Subsonic Speeds", IAS Preprint No. 313, January 1951.
48. Crosthwait, E. L. and Seath, D. D.: "Subsonic Characteristics of Low Aspect Ratios", Air Force Flight Dynamics Laboratory Technical Document Report No. FDL TDR 64-103, July 1964 (Scholar).
49. Lange/Wacke: "Test Report on Three-and Six-Component Measurements on a Series of Tapered Wings of Small Aspect Ratio", NACA TM 1176, 1948.
50. USAF Stability and Control DATCOM, Revised, January 1974, USAF Flight Dynamics Laboratory.
51. Hoerner, S. F. and Borst, H. V.: FLUID DYNAMIC LIFT, Mrs. L. A. Hoerner, Bricktown, N. J. 1975.
52. Curtiss, Jr. H. C., Hazen, D. C. and Putman, W. F.: "LTA Aerodynamic Data Revisited", Journal of Aircraft, Vol. 12, No. 11, Survey Paper, pp. 835-844, November, 1976.
53. Schlichting, H.: BOUNDARY LAYER THEORY, McGraw-Hill, N. Y., 1960.
54. Frost, R. C. and Rutherford, R. G.: "Subsonic Wing Span Efficiency", AIAA Journal, Vol. 1, pp. 931-933, April 1963.
55. Sim, A. G.: "Flight-Determined Stability and Control Characteristics of the M2-F3 Lifting Body Vehicle", NASA TN D-7511, December 1973.
56. Kilgore R. A. and Davenport E. E.: "Aerodynamic Damping and Oscillatory Stability of a Model of a Proposed HL-10 Vehicle in Pitch at Mach Numbers From 0.20 to 2.86 and in Yaw at Mach Numbers From 0.20 to 1.20", NASA TM X-72619, Langley Research Center, October 15, 1974.
57. Young, A. D. and Owen, P. R.: "A Simplified Theory for Streamline Bodies of Revolution, and Its Application to the Development of High-Speed Low-Drag Shapes", R&M No. 2071, Aeronautical Research Council, London, July 1943.

58. Hamill, P. A.: "Low Drag Bodies in an Incompressible Fluid", Report No. DME/NAE 1960 (3), Quarterly Bulletin of the Division of Mechanical Engineering and the National Aeronautical Establishment, Ottawa, September, 1960.
59. Hertel, H.: "Full Integration of VTOL Power Plants in the Aircraft Fuselage", AGARD CP No. 9, Part 1, Gas Turbines, pp. 69-96, 1966.
60. Galvao, F. L.: "A Note on Low Drag Bodies", XI OSTIV Congress, 1968.
61. Carmichael, B. H.: "Underwater Vehicle Drag Reduction Through Choice of Shape", AIAA Paper No. 66-657, 1966.
62. Parsons, J. S., Goodson, R. E. and Goldschmied, F. R.: "Shaping of Axisymmetric Bodies for Minimum Drag in Incompressible Flow", Journal of Hydraulics, Vol. 8, No. 3, pp. 100-107, July 1974.
63. Lachmann, G. V.: BOUNDARY-LAYER AND FLOW CONTROL, Vols. I and II, Pergamon Press, 1961.
64. Goldschmied, F. A.: "Integrated Hull Design Boundary-Layer Control and Propulsion of Submerged Bodies", AIAA Paper No. 66-658, 1966.
65. Goldstein, S.: "Low Drag and Suction Airfoils", Journal of the Aeronautical Sciences, Vol. 15, No. 4, pp. 189-214, April 1948.
66. Goodyear Aircraft Corp.: "A Theoretical Aerodynamic Analysis of a Boundary-Layer-Controlled Airship Hull", GER-6251, September 1954.
67. Cerreta, P. A.: "Wing Tunnel Investigation of the Drag of a Proposed Boundary-Layer-Controlled Airship", David Taylor Model Basin Aero Report 914, AD 127331, March 1957.
68. Horshe, M. P., Pake, F. A. and Wasson, H. R.: "An Investigation of a Boundary-Layer-Controlled Airship", Goodyear Aircraft Corp., GER 8399, October 1957.
69. Pake, F. A. and Pipitone, S. J.: "Boundary Layer Control for Airships", Proceedings of the Interagency Workshop on LTA Vehicles, MIT Flight Transportation Laboratory, FTL Report R75-2, pp. 147-155, January 1975.
70. Cornish, J. J. and Boatwright, D. W.: "Application of Full Scale Boundary-Layer Measurements to Drag Reduction of Airships", Aerophysics Department, Mississippi State University, Research Report No. 28, January 1960.

71. Wislicenus, G. F.: "Hydrodynamics and Propulsion of Submerged Bodies", ARS Journal, pp. 1140-1148, December 1960.
72. McLemore, H. C.: "Wind-Tunnel Tests of a 1/20-Scale Airship Model With Stern Propellers", NASA TN D-1026, January 1962.
73. Davis, J. M., et. al.: "Development of Heavy Lift Helicopter Handling Qualities for Precision Cargo Operations", American Helicopter Society Preprint 940.
74. Seckel, E., Traybar, J. J. and Miller, G. E.: "Longitudinal Handling Qualities for Hovering", Princeton University Department of Aeronautical Engineering Report 594, December 1961.
75. Haurwitz, B.: DYNAMIC METEROLOGY, McGraw-Hill, New York, 1941.
76. James, H. M., Nichols, N. B. and Phillips, R. S.: THEORY OF SERVO-MECHANISMS, McGraw-Hill, New York, 1947.